Responses to Reviewer #1

We appreciate the reviewer's encouragement and valuable comments for our manuscript. Our point-to-point responses are given below.

General Summary and Comments

With a set of comprehensive experimental design, this work studied the effects of air-sea coupling and ocean mean state in the boreal summer intraseasonal oscillation simulation. An interesting finding is that a cold ocean mean-state bias improved the simulated BSISO amplitude and spatial distribution by reducing overestimated subtropical summer mean rainfall, which results from the model systematic error. Although air-sea coupling captured correct SST-rainfall phase relationship, the current work shows that it has little effect in the BSISO northward propagating. This also makes incremental progress towards understanding such a debatable topic. The manuscript is well organized and the results are robust and clearly presented. I recommend the publication of this paper after my minor concerns below are addressed.

1. It is recommended to draw the grids of the axes in figures 4 and 5, so that the latitudes of the maximum centers can be easily recognized.

Response:

Good suggestion. The grids of both axes in Figures 4 and 5 have been added accordingly.

2. L207. I do not agree that rainfall and SST anomalies are out-of-phase over off-equatorial regions. since the zero contour lines of SST still locate near the maximum centers of rainfall (Figure 7f, g, h, k, l, m). Please consider adding the SST contours to figures 4 and 5, so that the associated propagations of SST and its phase relationship with rainfall can be clearly revealed.

Responses:

Yes, we agree with the reviewer that the intraseasonal rainfall and SST anomalies do not show a completely out-of-phase relationship over the off-equatorial western Pacific. However, the coupled models do capture the shift of the warm SST anomaly toward the suppressed convective region over the off-equatorial western Pacific (Figs. A1b and d), similar to the observations (Fig. A1a).

We have modified this sentence as follows: "Over the western Pacific, SPK reproduces the observed phase relationship between the convection and SST anomalies: a near-quadrature relationship over the equatorial regions (Figs. 7a–c), but a shift of warm SST anomalies toward the suppressed convective regions in the off-equatorial regions (Figs. 7f–h and k–m)." (Lines 220–222)

Following your suggestion, the SST anomalies were added to Figures 4 and 5 (as shown in Figs. A1 and A2 below) in the revised manuscript.

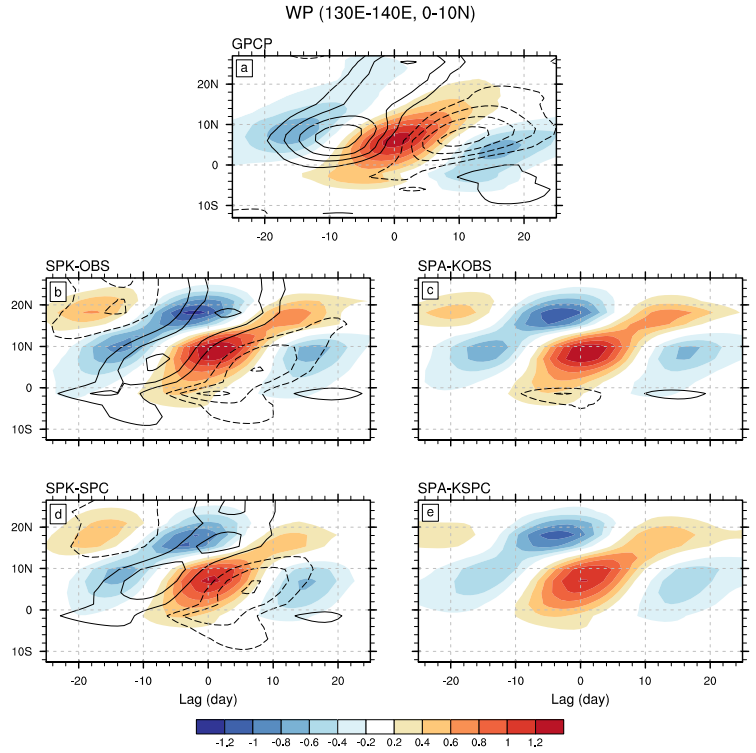

Figure A1. Lagged regression coefficients of 130°–140°E averaged intraseasonal precipitation (shading; [mm day^{-1}]/[mm day^{-1}]) and SST (contour; [ºC]/[mm day^{-1}]) onto (130°–140°E, 0°–10°N) averaged intraseasonal precipitation for (a) GPCP precipitation and ERAI SST, (b) SPK-OBS, (c) SPA-KOBS, (d) SPK-SPC, and (e) SPA-KSPC. The contour interval is 0.001 [ºC]/[mm day^{-1}]; the zero contour is omitted.

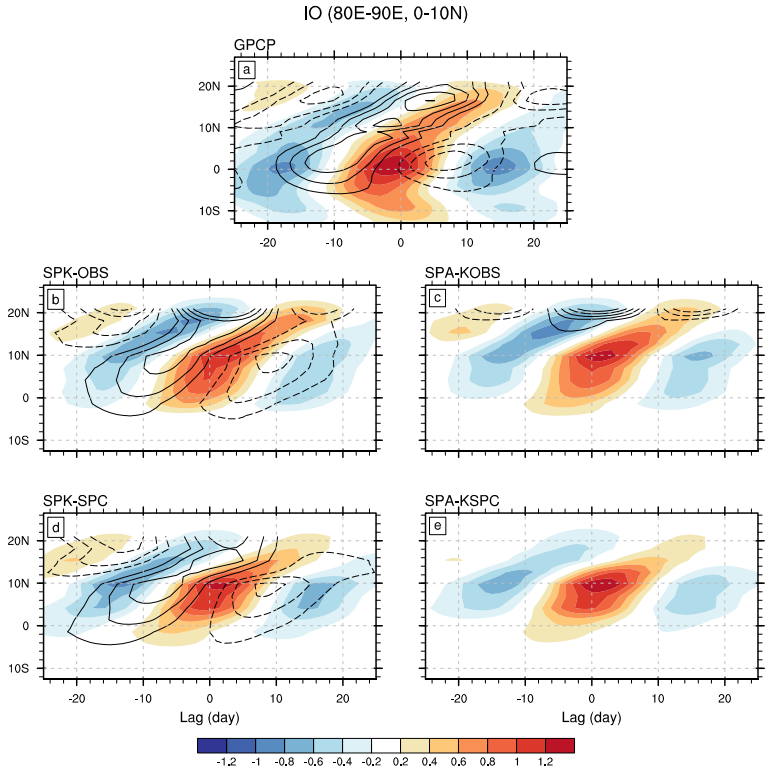

Figure A2. Same as Fig. A1, except for 80°–90°E averaged intraseasonal precipitation and SST regressed onto (80°–90°E, 0°–10°N) averaged intraseasonal precipitation.

3. L285. I don't think "large" is a nice adjective for "relationship".

Response:
Done.

4. L287-288. Please explain why "it is easy to surmise the effect of air-sea coupling on the amplitude of convection, while its effect on the propagation is not obvious". Is it because of the correct phase relationship, or is it from the shorter delay?

Response:
Thank you for pointing out this unclear description. To clarify it, we revised the sentences as follows: "As a consequence of the shorter delay, it is easy to surmise the negative effect of air-sea coupling on the amplitude of convection, while its effect on the propagation is not obvious." (Lines 300–301)

Responses to Reviewer #2

We appreciate the valuable and insightful comments provided by the reviewer. We have revised the manuscript carefully according to these comments and suggestions. Our point-to-point responses are given below.

General Summary and Comments

This study explores the role of mean SST biases in simulating the observed characteristics of BSISO. The study is carried out using a suite of numerical experiments in which an atmospheric model (SPCAM3) is configured with observed boundary forcing (uncoupled) and coupled to a mixed-layer ocean model (coupled). Each of these configurations is branched out into further configurations. The mixed-layer ocean model (MC-KPP) is first constrained to an observed climatology and then to the climatology of a coupled GCM (SPCCSM3). The boundary forcing is constructed from the SST of the two coupled simulations. Based on these experiments, the authors suggest that ocean mean state determines the skill of BSISO simulation in a coupled model. The manuscript is well written, and it is worthy of publications subject to addressing the specific comments below.

1. One objective of the study is to "examine the role of […] and mean state bias in the simulated BSISO using a configuration of SPCAM3 coupled to a mixed-layer ocean model". To overcome the limitations of the 1D model, MC–KPP is constrained to an ocean mean state. Please explain what the advantage is of running the new simulations and not just analyze SPCAM3 and SPCCSM3. SST biases in SPCCSM3 and SPK-SPC are very similar.

Responses:

There are two differences between the atmosphere-only SPCAM3 and atmosphere-ocean coupled SPCCSM3 models: air-sea coupling and ocean mean-state bias. Thus, it is hard to tell which factor (air-sea coupling or ocean mean-state bias) mainly causes the differences in the simulated BSISO between SPCAM3 and SPCCSM3. To isolate the air-sea coupling effect and the ocean mean-state effect, we carried out four experiments by using SPCAM3 coupled to the MC-KPP ocean model (SPCAM-KPP; see Table 1 in the manuscript or see Table B1 below). For example, to study the effect of the ocean mean-state bias on the simulated BSISO, SPCAM3-KPP is constrained to either observed ocean state ("SPK-OBS") or by the cold climatological SPCCSM3 ocean state ("SPK-SPC"). Both experiments have air-sea coupling, but the ocean mean state differs. To isolate the effect of air-sea interaction on the simulated BSISO under the observed (SPCCSM3) ocean mean state, SPCAM3 is forced by the 31-day smoothed SST from SPK-OBS (SPK-SPC) in experiment "SPA-KOBS" ("SPA-KSPC"). We compare SPA-KOBS to SPK-OBS; we compare SPA-KSPC to SPK-SPC. In both comparisons, the two experiments have the same ocean mean state, but one has air-sea coupling while the other does not.

Table B1: List of simulations analysed, including the experiment name, model, ocean climatology condition used by the model to constrain (coupled model) or as forcing (atmospheric-only model), and design purpose.

Exp	Model	Ocean surface	Purpose
SPK-OBS	SPCAM3-KPP	SST climatology from observation	Understanding ocean mean-state effect (SPK-OBS vs. SPK-SPC)
SPK-SPC	SPCAM3-KPP	SST climatology from SPCCSM3	
SPA-KOBS	SPCAM3	31-day smoothed SST from SPK-OBS	Understanding air-sea coupling effect under observed mean state (vs. SPK-OBS)
SPA-KSPC	SPCAM3	31-day smoothed SST from SPK-SPC	Understanding air-sea coupling effect under SPCCSM3 mean state (vs. SPK-SPC)

2. L65-66: There are other studies (e.g., Waliser et al. 1999; Bernie et al. 2005, 2007; Danabasoglu et al. 2006; Misra et al. 2008; Stan 2018) showing that air-sea coupling improves the representation of diurnal cycle, which is relevant for intraseasonal variability. This other side of the argument should also be mentioned here.

Responses:

Thank you for pointing out these interesting studies. We have modified the related sentence as follows: "By comparing the results of coupled GCMs (CGCMs) with the results of the AGCMs prescribed with observed SSTs, many studies found that the inclusion of air-sea coupling could produce a more realistic intraseasonal variability via improving the representation of the diurnal cycle at the air-sea interface (Waliser et al., 1999; Bernie et al., 2005; Danabasoglu et al., 2006; Misra et al., 2008; Stan, 2018). Besides the air-sea coupling process, the differences between simulated results may also come from ocean mean-state differences between AGCM and CGCM, as incorporating air-sea interaction in CGCMs inevitably introduces atmospheric and ocean mean-state biases." (Lines 55–60).

References:

Bernie, D. J., S. J. Woolnough, J. M. Slingo, and E. Guilyardi, 2005: Modeling diurnal and intraseasonal variability of the ocean mixed layer. J. Climate, 18, 1190–1202.

Danabasoglu, G., W. G. Large, J. J. Tribbia, P. R. Gent, B. P. Briegleb, and J. C. McWilliams, 2006: Diurnal coupling in the tropical oceans of CCSM3. J. Climate, 19, 2347–2365.

Misra, V., L. Marx, M. Brunke, and X. Zeng, 2008: The equatorial Pacific cold tongue bias in a coupled climate model. J. Climate, 21, 5852–5869.

Stan, C., 2018: The role of SST variability in the simulation of the MJO. Clim. Dyn., 51, 2943–2964.

Waliser, D. E., K. M. Lau, and J.-H. Kim, 1999: The influence of coupled sea surface temperatures on the Madden–Julian Oscillation: A model perturbation experiment. J. Atmos. Sci., 56, 333–358.

3. L97: Since MC-KPP must be constrained to a reference ocean climatology, some tuning is involved in this process to ensure a realistic behavior in the ocean currents. Please clarify if MC-KPP is retuned when is constrained to SPC.

Responses:

Yes, we retune the ocean temperature and salinity corrections when MC-KPP is constrained to SPC, i.e., the reference ocean climatology. For both the SPK-OBS and SPK-SPC simulations, we first perform a 10-year simulation with relaxation, to compute the required climatological temperature and salinity corrections. In these 10-year simulations, the MC-KPP ocean is relaxed toward the ocean climatology (either from observations or from SPC) with a timescale of 15 days. The temperature and salinity relaxation tendencies from this simulation are stored, and then a daily climatology of corrections is calculated. This daily climatology is then smoothed with a 31-day running mean, to remove the high-frequency variability. Physically, this mean the seasonal cycles of the temperature and salinity relaxation corrections account for the effects of ocean advection and of bias in the surface fluxes. These mean seasonal cycles of the corrections are then imposed on the SPK-OBS or SPK-SPC simulation with no relaxation, which displays only small SST biases against the SPC ocean climatology (Fig. 1 in the manuscript).

We have clarified that: “For each SPCAM3-KPP simulation analysed here, a 10-year “relaxation” simulation is first performed, with a 15-day relaxation timescale toward the reference seasonal cycles of ocean temperature and salinity.” (Lines 100–101). We explain detailed tuning processes in Lines 98–104.

4. L98-99: MC-KPP has some limitations for the study of air-sea coupling because atmospheric variables can be modified by horizontal advection whereas ocean surface variables cannot. Physical mechanisms involved may not be representative of what happens in observations. Please discuss this limitation.

Responses:

We agree with the reviewer that MC-KPP, which is a simple one-dimensional ocean model, only has vertical mixing but lacks ocean dynamics, such as horizontal or vertical advection or wind-driven upwelling. Besides, the air-sea coupled modes of variability (such as the ENSO) and potential feedbacks from these modes to intraseasonal variability are also absent. These limitations of MC-KPP are emphasized in Lines 90–

92 in the revised manuscript.

5. Section 2.2 Please explain what the expected outcome for each experiment is. It's a lot of mix and match without a clear path why they are conducted.

Responses:

Sorry for the confusion. We have clarified the designs and purposes of these experiments in the revised Section 2.2 (Lines 110–121, Table 1). For convenience, see the text below and Table B1 (in our response to the first comment).

"To study the effect of mean-state biases on simulated BSISO, SPK is constrained to two ocean mean states: 1) the 1980–2009 climatology from the Met Office ocean analysis (Smith and Murphy, 2007); and 2) the climatology from the 20-year SPCCSM3 ("SPC" for short) simulation, which was analysed in Stan et al. (2010) and DeMott et al. (2014). The former is considered as the observed ocean state (Fig. 1c), against which SPC shows large cold SST biases throughout the Indo-Pacific in the boreal summer (Fig. 1f). These two coupled simulations are referred to as "SPK-OBS" and "SPK-SPC", respectively. Differences between the results of SPK-OBS and those of SPK-SPC can reveal the effect of SPC mean-state SST biases on the simulated BSISO. To investigate the effect of air-sea interaction on simulated BSISO under the observed ocean mean state, the time-varying SSTs from SPK-OBS are prescribed in an SPA simulation ("SPA-KOBS"). The 31-day smoothed SST is used to remove the high-frequency variability of SST and avoid erroneous positive feedbacks between SSTs, surface fluxes and precipitation (see DeMott et al., 2015 and references therein). Similarly, we prescribe the 31-day smoothed SST from SPK-SPC to SPA to understand the air-sea coupling effect under the SPC mean state ("SPA-KSPC") through the comparison with SPK-SPC."

Reference:

DeMott, C. A., N. P. Klingaman, and S. J. Woolnough, 2015: Atmosphere-ocean coupled processes in the Madden-Julian oscillation. Rev. Geophys., 53(4), 1099–1154.

6. L113: What is the resolution of the ocean model in SPCCSM3? Please add some details about the ocean model in SPCCSM3.

Responses:

The Parallel Ocean Program (POP; Danabasoglu et al. 2006), the ocean component of SPCCSM3, is a three-dimensional ocean model, which includes ocean dynamics. SPCCSM3 utilizes the low horizontal resolution version (~3º) of POP. POP has 40 vertical layers with the thickness of the top layers being 10 m, and exchanges SST and surface fluxes with SPCAM3 at 1-day coupling frequency.

Detailed description about POP was added in the revised manuscript (Lines 84–88).

Reference:

Danabasoglu, G., W. G. Large, J. J. Tribbia, P. R. Gent, B. P. Briegleb, and J. C. McWilliams, 2006: Diurnal coupling in the tropical oceans of CCSM3. J. Climate, 19, 2347–2365.

7. L117: Please explain the reasoning behind the 31-day smoothing. Why not using monthly data?

Responses:

Actually, prescribing either monthly or 31-day smoothed SST to the AGCM is efficient for removing the high-frequency variability in the boundary conditions. Considering the temporal resolution of the boundary forcing used in SPCAM3 is daily, we simply used 31-day smoothed data. This explanation about data resolution was added in Lines 117–119 of the revised manuscript. For further details about the need for using temporally smoothed SSTs in AGCM simulations to study tropical intraseasonal variability, please see Section 6 of DeMott et al. (2015).

Reference:

DeMott, C. A., N. P. Klingaman, and S. J. Woolnough, 2015: Atmosphere-ocean coupled processes in the Madden-Julian oscillation. Rev. Geophys., 53(4), 1099–1154.

8. L120-121: ERAI is not the common data set used for validation of precipitation and OLR. Why this choice? Fig. 2a shows a double ITCZ feature, which is not seen in other datasets used for validation of precipitation (CMAP, GPCP).

Responses:

Thanks for this useful comment. We have replaced the precipitation and OLR from the ERAI reanalysis dataset by the GPCP precipitation (Huffman et al. 2001) and NOAA OLR (Liebmann and Smith 1996) in the revised manuscript.

The summer (May–October) mean precipitation patterns from ERAI, GPCP and CMAP are shown in Fig. B1. Overall, the precipitation pattern from ERAI (Fig. B1a) resembles those from GPCP (Fig. B1b) and CMAP (Fig. B1c). With a focus on the tropical Pacific, the precipitation associated with the ITCZ and SPCZ in ERAI is indeed larger than GPCP and CMAP observations, as noted by the reviewer. Thus, we used the precipitation from GPCP 1DD instead of ERAI in the revised manuscript (and we revised Figs. 2–7).

We also compared the dominant modes of BSISO represented by convection from different datasets (ERAI vs. NOAA) and circulations (Fig. B2). The spatial distributions of the first four EOF patterns seem to be highly consistent, although the amplitude is slightly different. To enhance the reliability of the data analyzed, we used NOAA OLR rather than the OLR from the reanalysis in the revised manuscript (and

we revised Figs. 9–12).

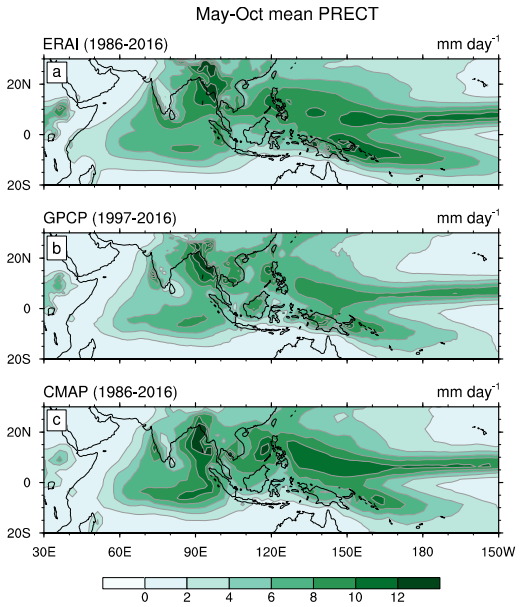

Figure B1. Summer (May–October) mean precipitation from (a) ERAI, (b) GPCP and (c) CMAP. The ERAI and CMAP data cover the period of 1986–2016 while the GPCP data is from 1997 to 2016.

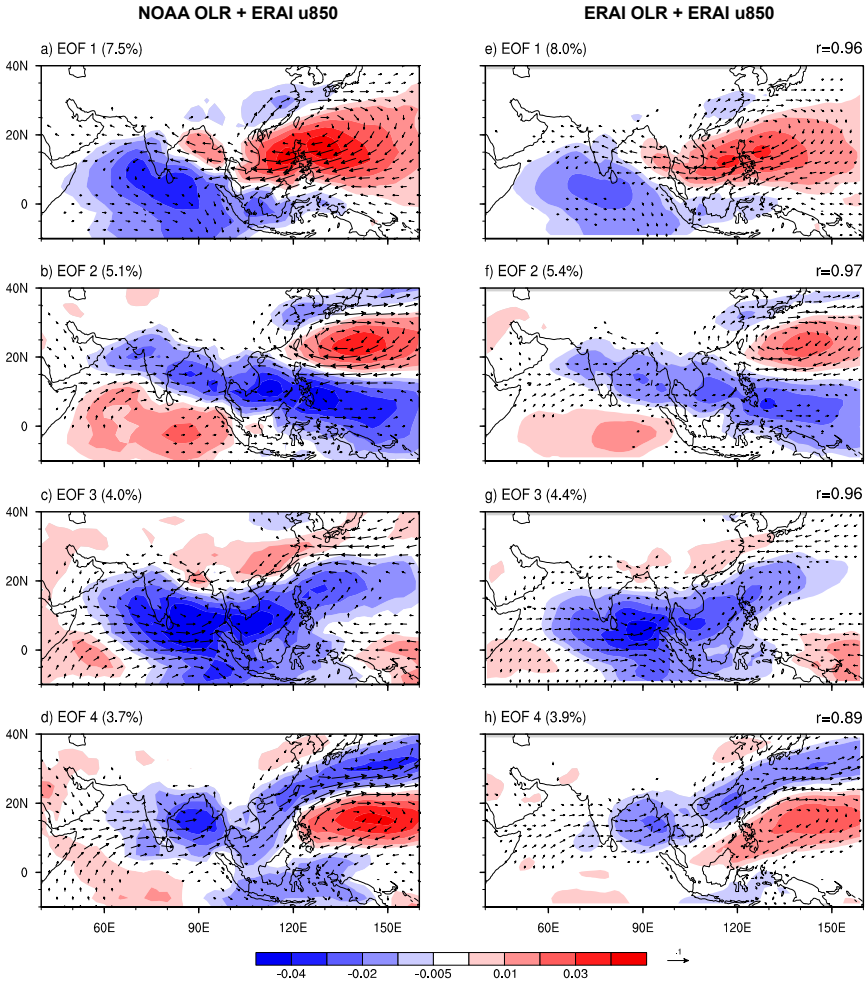

Figure B2. The first four leading MV-EOF modes of OLR (shading) and 850-hPa zonal wind (U850), derived from (a–d) NOAA OLR and ERAI U850, and from (e–h) ERAI OLR and ERAI U850. The meridional wind at 850 hPa was computed by regression onto the respective principal components. Numbers in parentheses indicate the percentage of variance explained. The pattern correlation of anomalous OLR in each MV-EOF mode derived from the two datasets is shown in the titles of (e–h).

References:

Huffman, G. J., Adler, R. F., Morrissey, M. M., Bolvin, D. T., Curtis, S., Joyce, R., McGavock, B., and Susskind, J., 2001: Global Precipitation at One-Degree Daily Resolution from Multisatellite Observations. J. Hydrometeorol., 2, 36–50.

Liebmann, B., Smith, C. A., 1996: Description of a complete (interpolated) outgoing long wave radiation dataset. Bull Am. Meteorol. Soc., 77, 1275–1277.

9. L127: OLR is generally viewed as a proxy of convective precipitation. This should be precipitation or OLR.

Response:

Revised accordingly.

10. L153-154: SPK-OBS displays the "bull's eye" feature specific to most SPCAM simulations. This feature disappeared in the SPCCSM simulations and hence was explained by the lack of coupling which would compensate for some unrealistic features caused by the periodic domain of CRM. Can the authors comment on the nature of these features in SPK-OBS, which is used as a coupled model?

Responses:

Besides air-sea coupling, SST mean states between SPCAM3 and SPCCSM3 are also different, as a large cold SST bias can be identified over the Indo-Pacific regions in SPCCSM3. Consistent with the SPCAM3 simulation (DeMott et al. 2011; as shown in Figure B3), SPK-OBS simulates a zonally oriented band of excessively intense precipitation extending from 65ºE to 150ºE. In contrast, this enhanced precipitation band is largely suppressed in SPK-SPC. This suggests that the mean-state SST bias (rather than the air-sea coupling process) in SPCCSM3 may be the primary factor that causes the precipitation bias. Related discussion has been added in the revised manuscript (Lines 167–170).

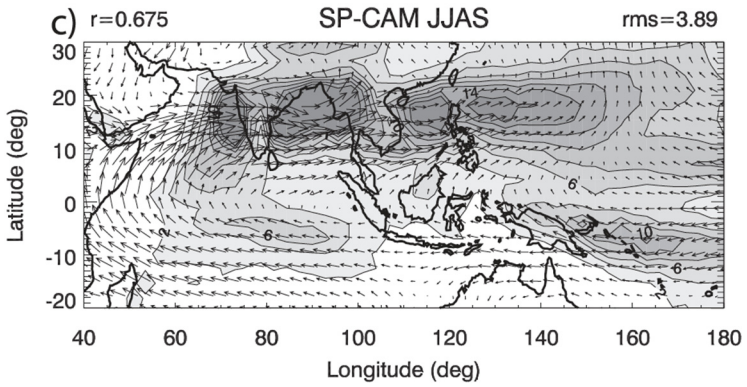

Figure B3. June–September mean precipitation and 850-hPa winds for SPCAM3. Precipitation contour interval is 2 mm day^{-1} starting at 2. (After Fig. 2c of DeMott et al. 2011)

Reference:

DeMott, C. A., Stan, C., Randall, D. A., Kinter, J. L. and Khairoutdinov, M., 2011: The Asian monsoon in the superparameterized CCSM and its relationship to tropical wave activity. J. Climate, 24(19), 5134–5156.

11. L162: The SST variability in SPC is lower than in OBS because the horizontal resolution of SPC is probably much coarser than in OBS.

Responses:

Thanks for this useful comment. As shown in Fig. B4, the deficient SST variability in SPK-SPC is largely associated with the deficient SST variability in SPCCSM3. POP in SPCCSM3 has a coarse horizontal resolution (~3º), which likely degrade the SST variability. We have added this in the revised manuscript (Lines 173–175).

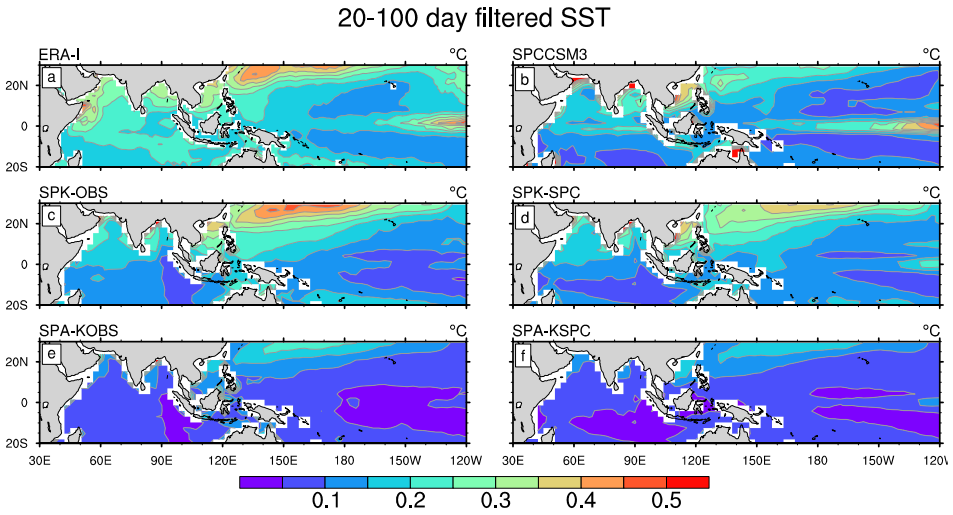

Figure B4. Standard deviations of 20–100-day-filtered SST during May–October derived from (a) ERAI, (b) SPCCSM3, (c) SPK-OBS, (d) SPK-SPC, (e) SPA-KOBS,

and (f) SPA-KSPC.

12. L169-171: Without comparing the mean state of SPK-OBS (SPK-SPC) and SPA-KOBS (SPA-KSPC) we cannot say that coupling and mean biases have a negative feedback of BSISO. This would be true only if the mean precipitation remains the same.

Responses:

Excellent suggestion. The atmospheric mean state is often similar in atmosphere-only and atmosphere-ocean coupled models with the same oceanic mean state. As shown in Fig. B5, mean SST and precipitation in SPA-KOBS (SPA-KSPC) are almost the same as those in SPK-OBS (SPK-SPC). We added in the revised manuscript: "Mean precipitation fields in SPA-KOBS and SPK-OBS (SPA-KSPC and SPK-SPC) are nearly the same." Thank you.

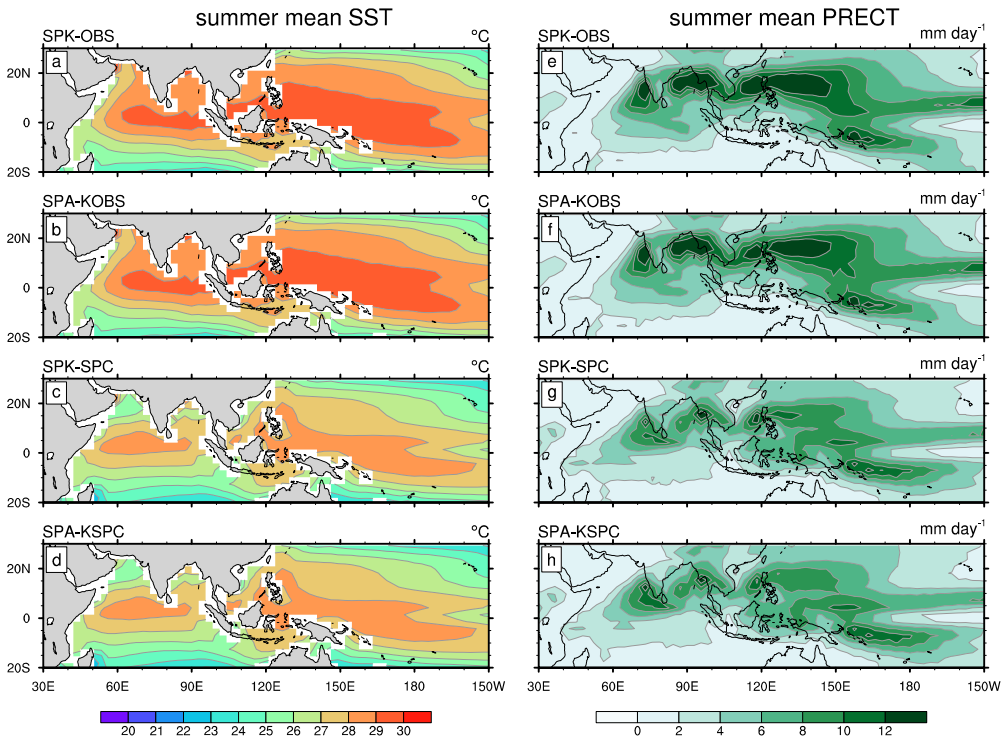

Figure B5. Summer (May–October) mean SST (left column) and precipitation (right column) from (a, e) SPK-OBS, (b, f) SPA-KOBS, (c, g) SPK-SPC, and (d, h) SPA-KSPC.

13. L175-181: Except for the southward propagation there is arguable any difference between observations and all simulations. Please revise these statements.

Responses:

Yes, all model simulations fail to capture the southward propagation of the BSISO. Other significant biases can be seen in the location of maximum BSISO convection.

The simulated convection center shifts northward (10ºN) relative to the observation (5ºN). We have modified these sentences. Please see Lines 191–193 in the revised manuscript.

14. L198-200: Please explain what features show the delay between the suppressed convection and warm SST.

Responses:

To reveal clearly the phase relationship between the convection and SST anomalies, we added the SST contours in Figures 4 and 5 in the revised manuscript. In the Indian Ocean (Fig. B6), SPK simulates well the observed near-quadrature phase relationship between the equatorial convection and SST anomalies. However, in the off-equatorial regions, the warm SST in the coupled models tends to shift toward the suppressed convective region. Over the western Pacific, the phase relationship between precipitation and SST seems to be properly represented in SPK simulations (Fig. B7).

We have carefully checked and modified the related sentences in the revised manuscript after the precipitation data were changed from ERAI to GPCP.

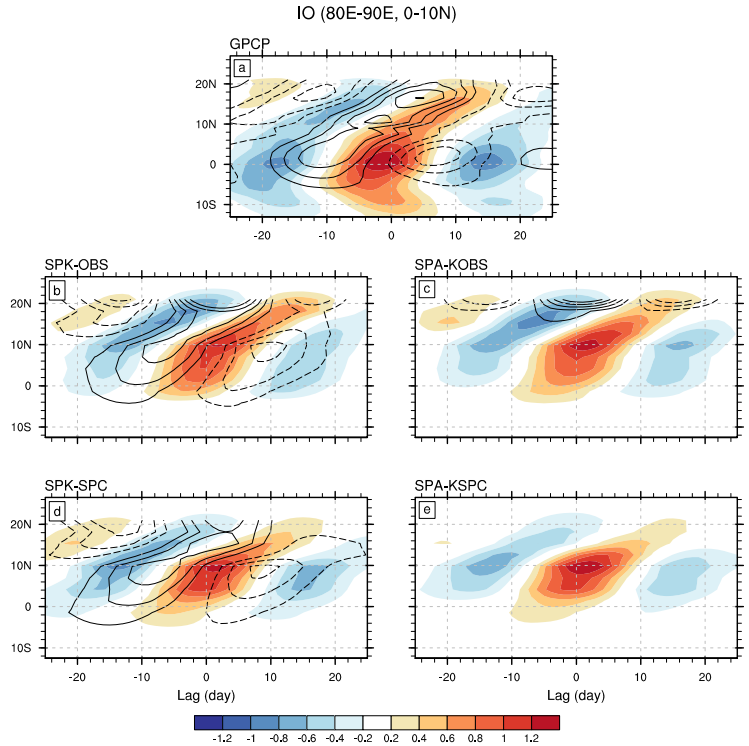

Figure B6. Lagged regression coefficients of 80º–90ºE averaged intraseasonal precipitation (shading; [mm day^{-1}]/[mm day^{-1}]) and SST (contour; [ºC]/[mm day^{-1}]) onto (80º–90ºE, 0º–10ºN) averaged intraseasonal precipitation for (a) GPCP precipitation and ERAI SST, (b) SPK-OBS, (c) SPA-KOBS, (d) SPK-SPC, and (e) SPA-KSPC. The contour interval is 0.001 [ºC]/[mm day^{-1}], and zero contour is omitted.

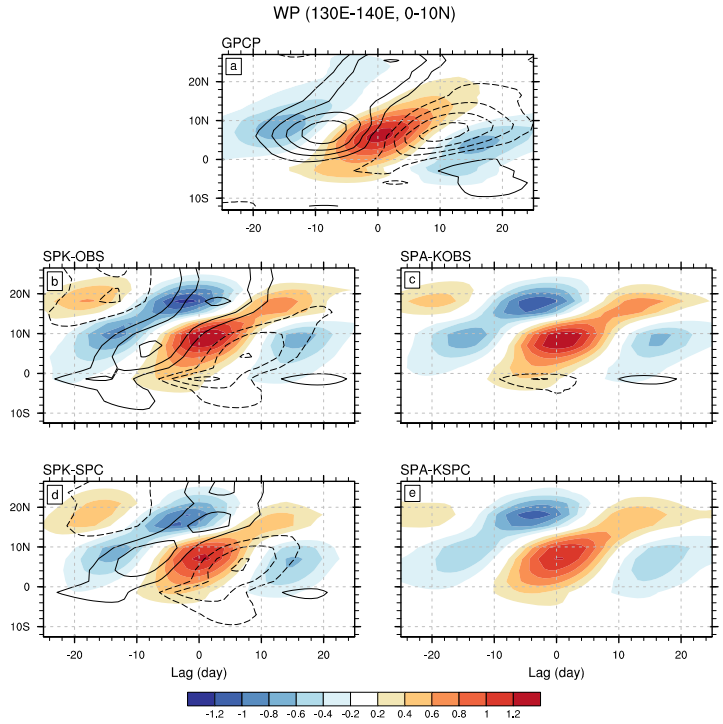

Figure B7. Same as Fig. B6, except for 130º–140ºE averaged intraseasonal precipitation and SST regressed onto (130º–140ºE, 0º–10ºN) averaged intraseasonal precipitation.

15. L202-204: The size of convective region is arguably different between observations and all model simulations. Please revise or show difference plots in support of a large difference.

Responses:

Yes, compared to GPCP precipitation, the size of the simulated convective region in all model simulations is smaller. We have revised the related sentences as follows: "The size of the convective regions in all model simulations is smaller than that in observations, which may imply a deficient BSISO propagation. Compared to SPK-OBS, the convective region reduces when either the SPC mean state is used (SPK-SPC) or air-sea coupling is removed (SPA-KOBS and SPA-KSPC)." (Lines 217–219)

16. L224: Please explain how one can use Fig. 8 (right column) to determine propagation of convection.

Responses:

As shown in Fig. B8, the temporal and spatial evolution of column-integrated moist static energy (MSE; $\langle m \rangle$) is highly consistent with that of anomalous precipitation (Figs. B8a and c). Positive values of the time change of $\langle m \rangle$ (i.e., $\partial \langle m \rangle / \partial t$) leads 90º ahead of the convection over both the Indian Ocean and western Pacific (Figs. B8b and d). Thus, the physical processes that modulate $\langle m \rangle$ (left column of Fig. B8) and

$\partial\langle m\rangle/\partial t$ (right column of Fig. B8) can be considered as the mechanisms responsible for the maintenance and propagation of convection, respectively. We have clarified the meaning of MSE diagnosis in the revised manuscript. Please see the text in Lines 138–142.

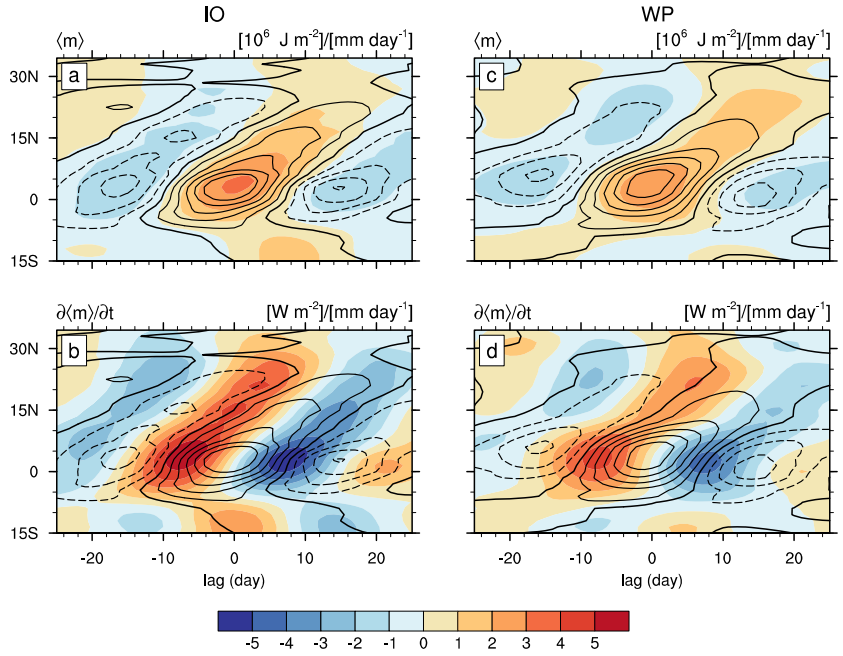

Figure B8. Lagged regression coefficients between longitudinal (75º–85ºE) averaged 20–100-day-filtered (a) $\langle m\rangle$ and (b) ($\partial\langle m\rangle/\partial t$) and area (75º–85ºE, 0º–10ºN) averaged 20–100-day-filtered precipitation over the Indian Ocean as a function of latitude. (c–d) Same as (a)–(b), except for the longitudinal (140º–150ºE) averaged variables regressed onto area (140º–150ºE, 0º–10ºN) averaged precipitation over the western Pacific (WP). Regression coefficients of precipitation are overlaid with an interval of 0.3 [mm day^{-1}]/[mm day^{-1}]; positive (negative) values are represented by solid (dashed) contours.

17. Section 3.4: The comparison between models and observations based on the BSISO indices can be very misleading because models can have their own BSISO with a different lifecycle than observations and this type of analysis will still consider 8 phases. A fair comparison can be done only if the phase compositing is constructed using PC1 and PC2 of observations for models as well. Here this is not possible because SST of the coupled model does not match an observed forcing. The only relevant analysis is to compare the lag-correlation of PC1 and PC2 for MISO 1 (with the 30-60 day period) and PC3 and PC4 for the MISO 2 (14-day period).

Responses:

It is true that models have their own BSISOs with different periods and evolutions, which lead to difficulties in comparing the features of simulated BSISO based on the same reference states. To ensure consistent analysis across all experiments, the

anomalous OLR and 850-hPa zonal wind produced by each model experiment are projected, respectively, onto the observed EOF modes to obtain their respective PC time series. This approach helps assess fairly how well the model experiments simulate the observed BSISO because the projected results (modelled PCs) can be directly compared with the observations. If we used the EOF modes derived from the outputs of individual experiments, differences in the spatial patterns and periods would compromise direct comparison of PC time series. In fact, the approach of projecting anomalous fields onto observed modes has been widely used for model assessment of MJO and BSISO simulations (Sperber et al. 2008, 2013; DeMott et al. 2019).

The advantage of this approach has been added in section 2.3 (Lines 155–157).

References:

DeMott, C. A., Klingaman, N. P., Tseng, W.-L., Burt, M. A., Gao, Y., and Randall, D. A., 2019: The convection connection: How ocean feedbacks affect tropical mean moisture and MJO propagation. J. Geophys. Res. Atmos., 124(22), 11910–11931.

Sperber, K. R. and Annamalai, H., 2008: Coupled model simulations of boreal summer intraseasonal (30–50 day) variability, Part 1: Systematic errors and caution on use of metrics. Clim. Dyn., 31(2–3), 345–372.

Sperber, K. R., Annamalai, H., Kang, I.-S., Kitoh, A., Moise, A., Turner, A., Wang, B. and Zhou, T., 2013: The Asian summer monsoon: an intercomparison of CMIP5 vs. CMIP3 simulations of the late 20th century. Clim. Dyn., 41(9–10), 2711–2744.

18. L300-310: The SST gradients in MC-KPP have very little physical meaning (1D ocean model) and no analysis related to SST gradients is shown in the results. How realistic it is to base the interpretation of results on the SST gradients "simulated" by MC-KPP?

Responses:

Excellent question. It is true that the SST gradients in MC-KPP do not arise from oceanic processes (e.g., currents). However, substantial SST gradients can be forced by gradients in atmospheric surface fluxes, to which MC-KPP responds. Thus, we would argue that the SST gradients have physical meaning, though they may not be as intense or frequent as those in observations or in coupled models with a dynamical ocean.

To address this issue, we compare the differences in summer-mean SST and $\langle m \rangle$ between SPK-OBS and SPK-SPC (Fig. B9). The spatial pattern of $\langle m \rangle$ closely follows that of SST. Thus, we argue that the stronger BSISO variability in SPK-OBS than that in SPK-SPC may be related to the enhanced meridional gradients of SST and moisture (Fig. B9). Although the gradient of SST is underestimated in SPK-SPC, we still discuss the roles of horizontal moisture (or $\langle m \rangle$) advection induced by anomalous flows in ISO propagation because this physical process has been highlighted in several recent studies

(Jiang 2017; Jiang et al. 2018; Gao et al. 2019). Our results here also support the findings about the contribution of horizontal moisture advection to BSISO propagation.

Related sentences have been modified in the revised manscript (Lines 317–323).

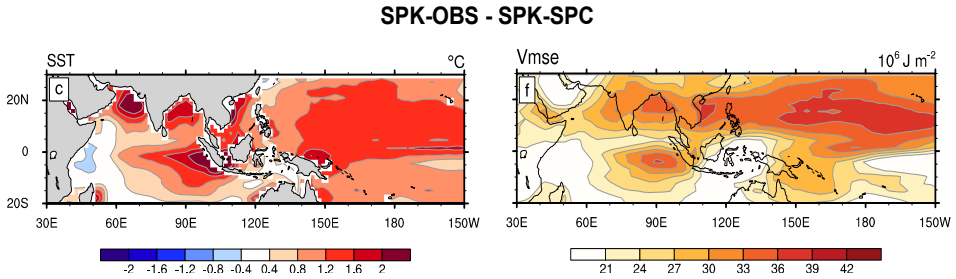

Figure B9. Differences in summer (May–October) mean (a) SST and (b) $\langle m \rangle$ between SPK-OBS and SKP-SPC (SPK-OBS minus SPK-SPC).

References:

DeMott, C. A., Klingaman, N. P., Tseng, W.-L., Burt, M. A., Gao, Y., and Randall, D. A., 2019: The convection connection: How ocean feedbacks affect tropical mean moisture and MJO propagation. J. Geophys. Res. Atmos., 124(22), 11910–11931.

Gao, Y., Klingaman, N. P., DeMott, C. A. and Hsu, P.: Diagnosing ocean feedbacks to the BSISO, 2019: SST-modulated surface fluxes and the moist static energy budget. J. Geophys. Res. Atmos., 124, 146–170.

Jiang, X., 2017: Key processes for the eastward propagation of the Madden-Julian Oscillation based on multimodel simulations. J. Geophys. Res. Atmos., 122, 755–770.

Jiang, X., Adames, A. F., Zhao, M., Waliser, D., and Maloney, E., 2018: A unified moisture moist framework for seasonality of MJO propagation. J. Climate, 31, 4215–4224.

19. Figure 1: The SST field is not an ERAI product.

Responses:

Yes, the ERAI is an atmospheric reanalysis dataset in which SST and sea ice concentration (SIC) were prescribed as boundary conditions for the atmospheric model. The SST and SIC used in the ERAI varied over different periods, which can be found in Table 1 of Dee et al. (2011).

We added: “Note that ERAI SST was the boundary condition prescribed for the ERAI.” (Line 128).

Reference:

Dee, D. P., and Coauthors, 2011: The ERA-Interim reanalysis: Configuration and performance of the data assimilation system. Q. J. Roy. Meteorol. Soc. 137(656), 553–597, 2011.

20. Figure 8: Please add the statistical significance of regression coefficients.

Response:

The statistical significance of regression coefficients has been added in the revised Fig. 8 (or see Fig. B10 below).

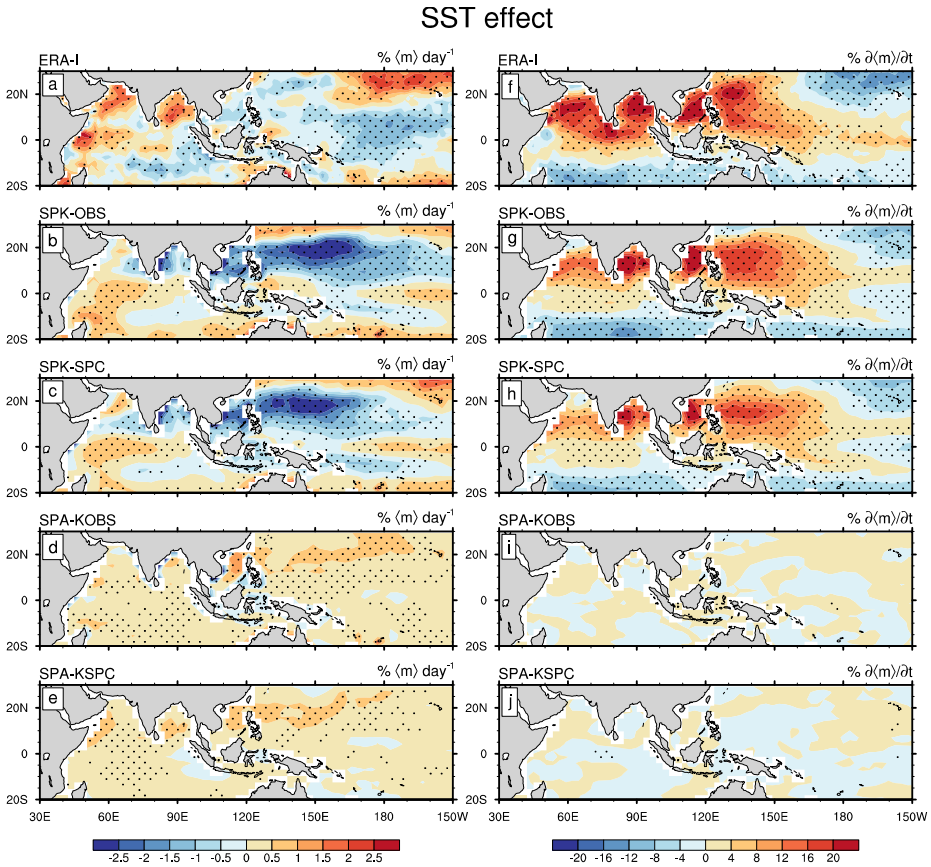

Figure B10. SST effect on (left column) $\langle m \rangle$ and (right column) $\partial \langle m \rangle / \partial t$ through the modification of surface turbulent fluxes for (a, f) ERAI, (b, g) SPK-OBS, (c, h) SPK-SPC, (d, i) SPA-KOBS, and (e, j) SPA-KSPC. Stippling marks regression coefficient being significant at the 95% confidence level.

Boreal summer intraseasonal oscillation in a superparameterized GCM: effects of air-sea coupling and ocean mean state

Yingxia Gao[1,2], Nicholas P. Klingaman[2], Charlotte A. DeMott[3], Pang-Chi Hsu[1]

[1]Key Laboratory of Meteorological Disaster of Ministry of Education/Collaborative Innovation Center on Forecast and Evaluation of Meteorological Disasters/NUIST-UoR International Research Institute, Nanjing University of Information Science & Technology, Nanjing, China
[2]National Centre for Atmospheric Science-Climate and Department of Meteorology, University of Reading, Reading, United Kingdom
[3]Department of Atmospheric Science, Colorado State University, Fort Collins, Colorado, USA

Correspondence to: Pang-Chi Hsu (pangchi@nuist.edu.cn)

Abstract. The effect of air-sea coupling on simulated boreal summer intraseasonal oscillation (BSISO) is examined using atmosphere–ocean-mixed-layer coupled (SPCAM3-KPP) and uncoupled configurations of the superparameterized (SP) Community Atmospheric Model, version 3 (SPCAM3). The coupled configuration is constrained to either observed ocean mean state or the mean state from the SP coupled configuration with a dynamic ocean (SPCCSM3), to understand the effect of mean-state biases on the BSISO. All configurations overestimate summer mean subtropical rainfall and its intraseasonal variance. All configurations simulate realistic BSISO northward propagation over the Indian Ocean and western Pacific, in common with other SP configurations.

Prescribing the 31-day smoothed sea surface temperature (SST) from the SPCAM3-KPP simulation in SPCAM3 worsens the overestimated BSISO variance. In both coupled models, the phase relationship between intraseasonal rainfall and SST is well captured. This suggests that air-sea coupling improves the amplitude of simulated BSISO and contributes to the propagation of convection. Constraining SPCAM3-KPP to the SPCCSM3 mean state also reduces the overestimated BSISO variability, but weakens BSISO propagation. Using the SPCCSM3 mean state also introduces a one-month delay to the BSISO seasonal cycle compared to SPCAM3-KPP with the observed ocean mean state, which matches well with observation. Based on a Taylor diagram, both air-sea coupling and SPCCSM3 mean-state SST biases generally lead to higher simulated BSISO fidelity, largely due to their abilities to suppress the overestimated subtropical BSISO variance.

1 Introduction

The intraseasonal oscillation (ISO) is the most vigorous sub-seasonal signal in the tropics (Zhang, 2005). It interacts with other tropical climate and weather systems, such as the El Niño–Southern Oscillation (ENSO) and tropical cyclones (Kessler et al., 1995; Zhang and Gottschalck, 2002; McPhaden, 2004; Wu et al., 2007), and even the mid-latitude systems (Ding and Wang, 2007; Moon et al., 2013). Compared to the boreal winter ISO (i.e., the Madden and Julian Oscillation, or MJO; Madden and Julian, 1971, 1972), the boreal summer ISO (BSISO) shifts away from the equator to the Asian summer monsoon (ASM)

region (Wang et al., 2006; Lau and Waliser, 2012). Thus, the BSISO is connected strongly to the onset, active and break phases of the ASM (Yasunari, 1979; Annamalai and Slingo, 2001; Lau and Waliser, 2012). The frequency of extreme events over the ASM region is also highly related to BSISO activity (Ren et al., 2013; Li et al., 2015; Hsu et al., 2016, 2017, 2020; Liu and Hsu, 2019).

Realistic representation of the BSISO in climate models remains a challenge, although some improvements have been achieved in recent decades. The state-of-the-art general circulation models (GCMs) still have difficulty in simulating properly the BSISO spatial pattern (Sperber and Annamalai, 2008; Sperber et al., 2013; Hu et al., 2017) and its northwest-southeast tilted rain band structure (Lin et al., 2006; Sabeerali et al., 2013). In contrast, its northward propagation, which is the most significant feature of the BSISO, is captured by most models. Fidelity for northward propagation improved in the models that contributed to the Coupled Model Intercomparison Project (CMIP) phase 5, relative to the CMIP phase 3 (Sabeerali et al., 2013; Sperber et al., 2013). Most models with reasonable northward propagation of the BSISO also simulate a good eastward propagation along the equatorial Indian Ocean.

The representation of convection is largely responsible for the ability of GCMs to simulate BSISO characteristics (Maloney and Hartmann, 2001; Randall et al., 2007; Jiang et al., 2016). Using the Hadley Centre atmospheric GCM (AGCM), Klingaman and Woolnough (2014) found that increasing the convective entrainment and detrainment rates considerably improved deficient MJO-like variability in the Indian and Pacific oceans. In recent years, studies have shown that "superparameterized" (SP) GCMs have high fidelity in simulating ISO variability (Benedict and Randall, 2009; Jiang et al., 2015; Neena et al., 2017). In SP GCMs, the traditional cumulus parameterization is replaced by a two-dimensional (2-D) cloud-resolving model in each grid column to calculate the cloud and radiation physics tendencies (Khairoutdinov and Randall, 2003; Khairoutdinov et al., 2005). By comparing different versions of the National Center for Atmospheric Research (NCAR) Community Atmospheric Model (CAM), DeMott et al. (2014) showed that the SP CAM (SPCAM3) gave better BSISO characteristics than the CAM with the standard convective parameterization.

Besides the convective parameterization scheme, the effect of air-sea interaction on simulated ISO variability has also received growing attention. By comparing the results of coupled GCMs (CGCMs) with the results of the AGCMs prescribed with observed SSTs, many studies found that the inclusion of air-sea coupling could produce a more realistic intraseasonal variability via improving the representation of the diurnal cycle at the air-sea interface (Waliser et al., 1999; Bernie et al., 2005; Danabasoglu et al., 2006; Misra et al., 2008; Stan, 2018). Besides the air-sea coupling process, the differences between simulated results may also come from ocean mean-state differences between AGCM and CGCM, as incorporating air-sea interaction in CGCMs inevitably introduces atmospheric and ocean mean-state biases. Due to the strong control on low-level moisture and convergence anomalies, such ocean mean-state biases may degrade simulated intraseasonal variability (Hendon, 2000; Inness et al., 2003; Sperber et al., 2005; Bollasina and Ming, 2013). Using the National Centers for Environmental Prediction (NCEP) coupled Climate Forecast System (CFS) model, Seo et al. (2007) showed that BSISO development and propagation were largely improved when the CGCM cold SST bias was removed via flux correction. They suggested that the role of air-sea interaction would be more accurate under an ocean mean state with smaller SST biases. To reduce the mean-

state differences between CGCMs and AGCMs, time-varying SSTs from CGCMs should be used to drive AGCMs (Fu and Wang, 2004; Seo et al., 2007; Levine and Turner, 2012; DeMott et al., 2015). However, this quantifies the role of air-sea coupling only under the biased CGCM mean state.

Through flux correction, CGCMs can be constrained to a given climatological ocean state. Such constraint is more effective in CGCMs with simple ocean models, which lack ocean dynamics, as ocean dynamics may interfere with the prescribed flux correction. Simple ocean models also lack coupled modes of variability, such as the ENSO, feedbacks from which can influence the perceived effect of coupling on sub-seasonal variability (Klingaman and DeMott, 2020). The CGCMs with simplified model oceans are a useful tool to investigate the roles of air-sea coupling and mean-state biases in the simulation of BSISO. In this study, we examine the roles of air-sea interaction and mean-state biases in simulated BSISO using a configuration of SPCAM3 coupled to a mixed-layer ocean model, constrained to observed ocean mean state and simulated mean ocean state from the SP Community Climate System Model (CCSM), version 3 (SPCCSM3; Stan et al., 2010). The model experiments, validation data, and analysis methods are described in section 2. In section 3, we analyse the influence of air-sea coupling and mean-state biases on the spatial pattern and propagation of simulated BSISO. Results are discussed and summarized in sections 4 and 5, respectively.

2 Model, experiments and methods

2.1 Models

SPCAM3 (Khairoutdinov et al., 2005) is employed in this study, due to its high fidelity for simulated ISO (Jiang et al., 2015; Neena et al., 2017). It has a horizontal resolution of T42 and a vertical resolution of 30 levels. The embedded 2-D cloud-resolving model has 32 columns with a fine resolution (4 km; Khairoutdinov and Randall, 2003). SPCCSM3 is the coupled configuration, in which SPCAM3 is coupled to the 3-D ocean model of Parallel Ocean Program (POP; Danabasoglu et al., 2006), with active ocean dynamics. SPCCSM3 utilizes the low-resolution version (~3º) of the POP, which has 40 vertical layers with the thickness of top layers being 10 m and exchanges SST and surface fluxes with SPCAM3 at 1-day coupling frequency. To understand the roles of air-sea interaction and SST mean-state biases in BSISO simulation, we couple SPCAM3 with the Multi-Column K Profile Parameterization (MC-KPP) mixed-layer ocean model, referred to as “SPCAM3-KPP” from now. In the MC-KPP, there is only vertical mixing (Large et al., 1994), while ocean dynamics, such as horizonal or vertical advection or wind-driven upwelling, are absent. Besides, the air-sea coupled modes of variability (such as the ENSO) and potential feedbacks from these modes to intraseasonal variability are also absent. The MC-KPP consists of many independent 1-D columns, with one column under each AGCM grid for coupling. Therefore, the horizontal resolution of MC-KPP is the same as that of SPCAM3. The MC-KPP has a fine vertical resolution, with 100 points in a 1000 m water column, 70 of which are in the top 300 m, and ~1-m resolution in the top 20 m. More details on SPCAM3-KPP can be found in Klingaman and DeMott (2020).

Since MC-KPP lacks ocean dynamics, SPCAM3-KPP must be constrained to a reference ocean climatology, which can be taken from an observation-based dataset, an ocean model simulation, or a CGCM simulation. To represent mean-ocean dynamics and correct for biases in surface fluxes, prescribed vertical profiles of heat and salt corrections are applied at each gridpoint at each timestep. For each SPCAM3-KPP simulation analysed here, a 10-year "relaxation" simulation is first performed, with a 15-day relaxation timescale toward the reference seasonal cycles of ocean temperature and salinity. The mean seasonal cycles of the temperature and salinity relaxation tendencies are then computed, smoothed with a 31-day running mean, and imposed as corrections in a "free-running" coupled integration with no relaxation, which displays only small SST biases against the reference climatology (Fig. 1). These free-running simulations are analysed here. More details on the correction method can be found in Hirons et al. (2015) and Klingaman and DeMott (2020).

2.2 Experiments and validation data

Two pairs of 50-year-long atmosphere-only (SPCAM3) and coupled (SPCAM3-KPP) models are analysed (Table 1). These simulations were also analysed for studying the MJO in Klingaman and DeMott (2020). For brevity, we write SPCAM3 and SPCAM3-KPP as "SPA" and "SPK", respectively. Next, we explain the setup of each experiment in detail.

To study the effect of mean-state biases on simulated BSISO, SPK is constrained to two ocean mean states: 1) the 1980–2009 climatology from the Met Office ocean analysis (Smith and Murphy, 2007); and 2) the climatology from the 20-year SPCCSM3 ("SPC" for short) simulation, which was analysed in Stan et al. (2010) and DeMott et al. (2014). The former is considered as the observed ocean state (Fig. 1c), against which SPC shows large cold SST biases throughout the Indo-Pacific in the boreal summer (Fig. 1f). These two coupled simulations are referred to as "SPK-OBS" and "SPK-SPC", respectively. Differences between the results of SPK-OBS and those of SPK-SPC can reveal the effect of SPC mean-state SST biases on the simulated BSISO. To investigate the effect of air-sea interaction on simulated BSISO under the observed ocean mean state, the time-varying SSTs from SPK-OBS are prescribed in an SPA simulation ("SPA-KOBS"). The 31-day smoothed SST is used to remove the high-frequency variability of SST and avoid erroneous positive feedbacks between SSTs, surface fluxes and precipitation (see DeMott et al., 2015 and references therein). Similarly, we prescribe the 31-day smoothed SST from SPK-SPC to SPA to understand the air-sea coupling effect under the SPC mean state ("SPA-KSPC") through the comparison with SPK-SPC. Table 1 summarises all four experiments.

The validation data used in this study include: 1) daily outgoing longwave radiation (OLR) from the National Oceanic and Atmospheric Administration (NOAA) at a resolution of 2.5º×2.5º for 1986–2016 (Liebmann and Smith, 1996); 2) daily precipitation from the Global Precipitation Climatology Project (GPCP; Huffman et al., 2001) at a resolution of 1º×1º for 1997–2016; and 3) daily variables from the European Centre for Medium-range Weather Forecasts (ECMWF) Interim (ERAI) reanalysis dataset at a resolution of 1.5º×1.5º (Dee et al., 2011). The variables from the ERAI include: 850-hPa wind, SST, surface variables related to latent heat and sensible heat (LH and SH) fluxes, and 3-D variables associated with moist static energy (MSE; Maloney, 2009). Note that ERAI SST was the boundary condition prescribed for the ERAI. We analyse the period of 1986–2016 of ERAI data for compatibility with Gao et al. (2019).

2.3 Methods

The BSISO convective intensity is represented by 20–100-day-filtered variability of boreal summer (May–October) precipitation, OLR or MSE, depending on the process-oriented diagnostic applied. To reveal the overall propagation features of BSISO convection, lead-lag regression analysis is performed on area-averaged, filtered precipitation or OLR. Here, we use precipitation. Since the Indian and Pacific basins exhibit different basic states (Lau and Waliser, 2012), we compute propagation over one region in each basin: the eastern Indian Ocean (80°–90°E, 0°–10°N) and western Pacific (130°–140°E, 0°–10°N).

DeMott et al. (2016) and Gao et al. (2019) provided a useful diagnostic method to quantitatively assess the contribution of intraseasonal SST variability to the MSE budget of ISO in the boreal winter and boreal summer, respectively. The temporal and spatial evolution of column-integrated MSE ($\langle m \rangle$) is highly consistent with that of anomalous precipitation; and positive values of the time change of $\langle m \rangle$ ($\partial \langle m \rangle / \partial t$) leads 90° ahead of the convection. Thus, the physical processes that modulate $\langle m \rangle$ and $\partial \langle m \rangle / \partial t$ can be considered as the mechanisms responsible for the maintenance and propagation of convections, respectively. We employ the same approach to understand oceanic feedbacks to the simulated BSISO, and compare these feedbacks to those in reanalysis data. Intraseasonal SST can affect atmospheric convection through modifying LH and SH fluxes and hence MSE, via the near-surface gradients in specific humidity and temperature. Based on decomposition of surface bulk formulae (Weare et al., 1981), SST modulation of surface fluxes is represented as the difference between fluxes calculated using the full and 61-day smoothed SST. These SST-modulated fluxes are then projected onto $\langle \mathrm{m} \rangle$ and $\partial \langle \mathrm{m} \rangle / \partial \mathrm{t}$ to reveal the oceanic feedbacks to the maintenance and propagation of BSISO convection, respectively. More details can be found in DeMott et al. (2016) and Gao et al. (2019).

We employ the BSISO indices of Lee et al. (2013) to investigate the simulated convective features in each BSISO phase. First, daily anomalies are computed as the departure from the climatological annual cycle and a 120-day running mean. Multi-variate Empirical Orthogonal Function (MV-EOF) is then performed on the combination of OLR and 850-hPa zonal wind (u850) anomalies, each normalized by their respective area-mean standard deviation over the ASM region (40°–160°E, 10°S–40°N) during the boreal summer. The first two leading principal components (PC1 and PC2) define the BSISO indices, which separate the BSISO life cycle into eight phases. For model results, normalized OLR and u850 anomalies are projected onto the observed EOF modes to obtain the model PCs. This approach helps assess fairly how well the model experiments simulate the observed BSISO because the projected results (model PCs) can be directly compared to observations (Sperber et al., 2008, 2013; DeMott et al., 2019). Model simulated BSISO phase composites are constructed based on these PCs. Consistent with Lee et al. (2013), only strong BSISO events ($\sqrt{\mathrm{PC1}^2 + \mathrm{PC2}^2} > 1.5$) are selected for phase composites.

3 Results

3.1 Mean state and intraseasonal variability

Previous studies indicated that ISO variability is closely related to the climatological state of convection (Wheeler and Kiladis, 1999; Sperber et al., 2000; Waliser et al., 2003). Thus, we first examine the summer mean precipitation and 850-hPa wind (Fig. 2). In GPCP, substantial rainfall appears over the ASM region (Fig. 2a). In common with SPCAM3 simulation (DeMott et al., 2011), SPK-OBS overestimates subtropical rainfall (10°–20°N), particularly in the western North Pacific (Figs. 2b and e), but underestimates rainfall over the southern Indian Ocean, Maritime Continent and India north to 20°N. These precipitation biases are associated with low-level wind biases. Simulated mean westerlies extend into the western North Pacific, increasing convergence across the band of subtropical enhanced precipitation. In SPK-SPC (Fig. 2c), which is constrained to the cold climatological SPC SST (Fig. 1d), rainfall is reduced compared to that in SPK-OBS: wet biases are reduced while dry biases become more severe over the Indian Ocean and western North Pacific (Figs. 2e and f). The SPC mean-state SST bias tends to suppress the mean precipitation. Mean precipitation fields in SPA-KOBS and that in SPK-OBS (SPA-KSPC and SPK-SPC) are nearly the same (not shown).

Figure 3 illustrates the standard deviations of intraseasonal SST and precipitation variability. SST variability is underestimated over the Indian Ocean and equatorial Pacific in all simulations. In the off-equatorial Pacific, we see more intraseasonal SST variability in SPK-OBS but less SST variability in SPK-SPC (Figs. 3b and c), which may be related to the less SST variability in SPC as a consequence of coarse horizontal resolution of POP. Prescribing the 31-day smoothed SST from SPK-OBS (SPK-SPC) to SPA-KOBS (SPA-KSPC) strongly reduces intraseasonal SST, as expected (Figs. 3d and e). The right-column panels in Fig. 3 show the intraseasonal rainfall from each dataset (Figs. 3f–j). Compared to GPCP (Fig. 3f), all simulations significantly overestimate subtropical intraseasonal precipitation variability (10°–20°N), where mean rainfall is also overestimated (Fig. 2). This reinforces that model BSISO biases are largely associated with incorrect representation of mean rainfall (Sperber and Annamalai, 2008; Sabeerali et al., 2013; Hu et al., 2017). The overestimate of intraseasonal rainfall in SPK-SPC (Fig. 3h) is smaller than that in SPK-OBS (Fig. 3g), consistent with the lower mean rainfall in SPK-SPC. SPA-KOBS (Fig. 3i) and SPA-KSPC (Fig. 3j) show increases in intraseasonal rainfall relative to SPK-OBS and SPK-SPC, respectively. This indicates that both cold SST biases and air-sea coupling exert negative feedbacks on BSISO convection, and improve the simulated BSISO amplitude.

3.2 Northward propagation of BSISO

Lag regression analysis is employed to understand the simulated BSISO propagation in each experiment. Over the Indian Ocean, area (80°–90°E) averaged intraseasonal precipitation and SST are regressed onto area (80°–90°E, 0°–10°N) averaged intraseasonal precipitation time series (Fig. 4). In observation, the convective anomaly originates south of the equator and propagates southward to 10º–15ºS and northward into the Bay of Bengal (Fig. 4a). All simulations capture the northward propagation, confirming the high fidelity of SPCAM3 in simulating BSISO northward propagation (DeMott et al., 2014; Neena

et al., 2017). However, the simulations fail to capture the southward propagation branch. Other significant biases can be seen in the locations of maximum convections of BSISO. The simulated convective center shifts northward (10°N) relative to observation (5°N). A weaker propagating signal is observed under the SPC mean state than under the observed mean state for both SPK and SPA, especially over the subtropical regions from Lag 0 to Lag 20 (Figs. 4b and d; Figs. 4c and e). This is consistent with weaker BSISO variability under the SPC mean state (Figs. 3g–j), suggesting that cold tropical mean SST biases are unfavourable for BSISO variability and northward propagation. In SPA, the amplitude of convective maxima increases relative to that in SPK, but with weaker propagation (Figs. 4b–e). Air-sea coupling plays a similar role in BSISO convection under both observed and cold mean states: it damps BSISO amplitude but supports northward propagation over the eastern Indian Ocean.

The BSISO northward propagation over the western Pacific is shown in Fig. 5. The observed convection also originates south of the equator, but propagates only north, into the western North Pacific (Fig. 5a). These characteristics are properly simulated by all experiments (Figs. 5b–e). As in the Indian Ocean, due to the large overestimate of subtropical BSISO variability, the strongest simulated convection moves north compared to observation. It is notable that considerable suppressed off-equatorial convection leads the strongest convection by ~1 week, which degrades model performance. Over the western Pacific, mean-state biases also reduce the northward propagating signal in SPK-SPC (SPA-KSPC) relative to that in SPK-OBS (SPA-KOBS). Air-sea interaction seems to play little role in the BSISO northward propagation over the western Pacific, as there is no substantial difference between SPK and SPA under either ocean mean state (Figs. 5b–c; Figs. 5d–e).

3.3 Quantitative contribution of SST fluctuation to BSISO

The temporal and spatial evolutions of BSISO and SST variability over the Indian Ocean and western Pacific are shown in Figs. 6 and 7, respectively. Over the Indian Ocean, the warm SSTs in observation always lead enhanced convection, with maxima north/northeast of the convective center (Figs. 6a, f and k). The SST-rainfall phase relationship is properly represented in SPK but misrepresented in SPA. However, SPK shows a shorter delay between off-equatorial suppressed convection and warm SST relative to observation, which can be more clearly revealed in Fig. 4. This suggests the ocean responds more quickly to BSISO convection in SPK than in observation, which might be caused by the lack of ocean dynamics in MC-KPP. Alternatively, the high coupling frequency (15 minutes) and fine ocean vertical resolution (~1 m) in SPK may make the mixed-layer depth too sensitive to atmospheric convection. The SST anomalies in SPA are small due to the 31-day smoothing applied (Figs. 6d, e, i, j, n, and o). The size of the convective regions in all model simulations is smaller than that in observations, which may imply a deficient BSISO propagation. Compared to SPK-OBS, the convective region reduces when either the SPC mean state is used (SPK-SPC) or air-sea coupling is removed (SPA-KOBS and SPA-KSPC). To some degree, it reflects the negative (positive) role of mean-state biases (air-sea interaction) in supporting the propagating BSISO signal, in agreement with Fig. 4.

Over the western Pacific, SPK reproduces the observed phase relationship between the convection and SST anomalies: a near-quadrature relationship over the equatorial regions (Figs. 7a–c), but a shift of warm SST anomalies toward the suppressed

convective regions in the off-equatorial regions (Figs. 7f–h and k–m). This phase relationship can also be clearly revealed in the Hovmöller diagram (Fig. 5). However, SPK produces substantial suppressed convection north of the active convection over the western North Pacific, consistent with Fig. 5. Besides, simulated warm SST appears north of the convective center, while the ERAI SST maximum is always located northwest of the convective center. This implies that the simulated SST may be favourable for the northward but unfavourable for the westward propagation of the simulated BSISO convection over the western Pacific. Imposing the SPC mean state weakens the simulated convection. In SPA, the intraseasonal SST is very small by design.

As revealed by Gao et al. (2019), intraseasonal SST can affect the BSISO by modulating surface LH and SH fluxes. The temporal and spatial distributions of SST-modulated fluxes are highly coherent with those of SST anomalies themselves. Therefore, the evolutions of SST anomalies shown in Figs. 6 and 7 can also roughly reveal the evolutions of SST-modulated surface fluxes. By regressing the SST-modulated flux anomalies onto the BSISO $\langle \mathrm{m} \rangle$ and $\partial\langle \mathrm{m} \rangle / \partial \mathrm{t}$, Fig. 8 illustrates the "SST effect" on the maintenance and propagation of convection. In the ERAI, intraseasonal SST supports $\langle m \rangle$ in the central Indian Ocean and Bay of Bengal but destroys $\langle m \rangle$ in the western North Pacific (Fig. 8a). The inter-basin differences are linked to the differences in SST-convection phase relationship (Gao et al., 2019). However, simulated SST anomalies in SPK largely damp the convection over the Bay of Bengal and western North Pacific (Figs. 8b and c), because of the quicker response of the SPK ocean to BSISO convection, combined with the erroneously strong suppressed convection just before the active phase. The negative SST effect on $\langle m \rangle$ agrees with the stronger subtropical BSISO variability in SPA than in SPK. For the BSISO propagation, the simulated SST anomalies play positive roles in $\partial\langle \mathrm{m} \rangle / \partial \mathrm{t}$ under both ocean mean states (Figs. 8g and h), but with a smaller contribution (8–12%) than that in the ERAI (12–20%). A weak SST effect on the BSISO can still be found in SPA (Figs. 8d, e, i, and j), as these simulations retain some intraseasonal SST variability (Fig. 3). In summary, SST variability enhances the simulated amplitude of BSISO variability by suppressing the excessive subtropical convection and contributes to the propagation of convection over the entire BSISO region.

3.4 BSISO indices

Propagating BSISO characteristics can also be examined using the BSISO indices. Figure 9 shows the annual cycle of variance of each of the first four PCs from observation and model simulations. Since EOF analysis is only applied to May–October data, the PC time series for November–April are obtained by projecting OLR and u850 anomalies onto the same EOF patterns.

In observation, PC1 has the largest variance throughout the boreal summer (Fig. 9a). It increases sharply from late April, maximises in August, and is followed by PC2 with about half a month delay. In contrast to PC1 and PC2, PC3 exhibits most of its variance in early summer (May–June). PC4 also has a broad peak, but its amplitude is much smaller than those of the other PCs. SPK-OBS produces a similar seasonal cycle of PC1 as observation, except for deficient variance in August–September, which largely reduces the amplitude difference between the first two PCs (Fig. 9b). Simulated PC1 in SPK-OBS also increases abruptly from late April, with a half-month delay between PC1 and PC2, which matches observation well. However, PC1 in SPK-SPC begins to increase in late May (Fig. 9c), about one month later than observation and SPK-OBS.

The variance of the first two PCs in SPK-SPC has a much narrower peak and tails off from early July, without a second peak in October. This suggests that cold SST bias leads to a late onset of BSISO activity, and also strongly degrades the annual cycle of BSISO activity. In both SPK simulations, the amplitude of PC3 is smaller than that of PC4, indicating that the order of those simulated PCs is reversed. All model simulations show a similarly poor ability to simulate PC3 and PC4. Therefore, hereafter we only focus on PC1 and PC2. Removing air-sea coupling in SPA increases significantly the strength of PC1 relative to that in SPK (Figs. 9b and d; Figs. 9c and e). This suggests that the role of air-sea coupling in suppressing BSISO variability is mainly expressed through damping variability in PC1.

Based on the PC1 and PC2 time series, the BSISO life cycle is separated into eight phases, which represents the canonical northward propagating BSISO (Annamalai and Sperber, 2005; Wang et al., 2005). Figure 10 shows the phase composites of anomalous precipitation and 850-hPa wind from observation and SPK-OBS. SPK-OBS displays a similar evolution of the structure of convection and circulation as the observation, but they have significant amplitude differences. The simulated precipitation variability is underestimated over the equatorial Indian Ocean, while substantial overestimate appears over the off-equatorial regions. The simulated circulation matches well with the simulated convection: easterlies (westerlies) occur to the north (south) of the ascent; cyclonic (anticyclonic) circulations coincide with the active (suppressed) off-equatorial convection. However, the northwest-southeast titled rainfall band in SPK-OBS is more zonal than that in GPCP (Figs. 10e and m), largely due to the poor representation of BSISO variability over the western Pacific. In observation, most strong BSISO events occur in phases 2, 5, 7, and 8. In contrast, in SPK-OBS, a stronger preference for simulated strong BSISO events appear in off-equatorial regions (phases 3, 4, 7, and 8) rather than in near-equatorial regions (phases 1, 2, 5, and 6). It implies that the BSISO variability is largely determined by the propagating BSISO signal (Sperber et al., 2013; Neena et al., 2017).

We further compute the frequency of strong BSISO events in each phase from each dataset (Fig. 11). Overall, there are fewer strong BSISO events in the simulations (22.5–27.5%) than in observation (~33%), although the amplitude of simulated precipitation associated with these events is much larger. The frequency of stronger BSISO events becomes further fewer under the SPC ocean mean state than that under the observed ocean mean state. Consistent with Fig. 10, phases 2, 5, 7, and 8 show the highest frequencies in observation, while in SPK-OBS and SPK-SPC, most strong simulated BSISO events occur in phases 3, 4, 7, and 8. Removing air-sea coupling in SPA further increases the frequency of strong BSISO events in the off-equatorial regions, associated with the greater intraseasonal convective variability in SPA relative to that in SPK.

To quantitatively evaluate the performance of each simulation, we construct Taylor diagrams over the Indian Ocean (50°–100°E, 10°S–20°N) and western Pacific (110°–160°E, 0°–30°N), respectively (Fig. 12). These diagrams provide pattern correlation coefficients and root-mean-square-errors of simulated intraseasonal precipitation against GPCP intraseasonal precipitation in each BSISO phase. Over the Indian Ocean, the fidelity of each simulation varies from phase to phase (Fig. 12a). Generally, higher pattern correlations appear in equatorial phases (phases 1, 2, 5 and 6) than in off-equatorial phases (phases 3, 4, 7 and 8). Under the observed ocean mean state, air-sea coupling improves the simulation fidelity in most phases, while the SPC ocean mean state and coupling under the SPC ocean mean state have little consistent effect on the simulated BSISO fidelity.

In almost all simulations, higher pattern correlations are found over the western Pacific (0.6–0.9) than over the Indian Ocean (0.5–0.8), but with much larger overestimates of amplitude (Fig. 12b). The overall simulation performance over the western Pacific is ranked as follows: SPK-SPC, SPA-KSPC, SPK-OBS, and SPA-KOBS. Simulations with the SPC ocean mean state perform better than those with the observed ocean mean state, in terms of both amplitude and distribution. Since the excessive subtropical rainfall variability is the biggest error in SPCAM3, the underlying cold SSTs largely weaken the convection, which helps reduce the amplitude biases and improve the pattern correlation with observation. Air-sea coupling improves model performance under both ocean mean states, particularly in terms of suppressing the overestimated BSISO variability over the western North Pacific.

4 Discussion

Despite the correct SST-rainfall phase relationship in SPK simulations, a shorter delay between suppressed convection and warm SST occurs compared to the reanalysis. This may be associated with the configuration of the MC-KPP ocean (lack of full ocean dynamics, high coupling frequency and fine vertical resolution). As a consequence of the shorter delay, it is easy to surmise the negative effect of air-sea coupling on the amplitude of convection, while its effect on the propagation is not obvious. Overall, intraseasonal SST anomalies in SPK largely damp intraseasonal subtropical convection variability and make a smaller contribution (8–12%) to $\partial\langle \mathrm{m} \rangle / \partial \mathrm{t}$ than those in the ERAI (12–20%). Comparing Figs. 4 and 5, we can see propagation is slightly enhanced in SPK relative to SPA over the Indian Ocean; however, coupling makes nearly no difference to the propagating signal over the western Pacific. This may be related to the larger underestimate of the contribution of intraseasonal SST to $\partial\langle \mathrm{m} \rangle / \partial \mathrm{t}$ over the western Pacific than over the Bay of Bengal (Fig. 8). More importantly, it implies that atmospheric internal processes are essential to the propagation of convection, since SPCAM3 simulates BSISO propagation well even without coupling or sub-seasonal SST variability.

Stan et al. (2010) and Neena et al. (2017) reported that SPC showed better ISO simulation skill than SPA with prescribed observed SST. In our experiments, the BSISO variability is similar in SPK-OBS and SPA-KOBS and in SPK-SPC and SPA-KSPC, which suggests a limited role for air-sea coupling in the simulated BSISO. Comparing SPK-OBS and SPK-SPC strongly suggests that the ocean mean-state biases in SPC improve BSISO amplitude and spatial distribution. This implies that mean-state biases in SPC, not sub-seasonal air-sea coupled feedbacks, be the primary reason for the improved BSISO in SPC relative to SPA. While the SPC mean state improves the amplitude and spatial pattern of simulated BSISO convection, it also weakens northward propagation. Besides the SST mean-state biases, it is also important to control the SST gradient bias. Several studies highlighted the importance of horizonal advection of mean moisture (or $\langle m \rangle$) by anomalous wind in the propagation of the ISO (Hsu and Li, 2012; Jiang, 2017; Jiang et al., 2018; DeMott et al., 2019; Gao et al., 2019). Our additional diagnosis revealed that the pattern of $\langle m \rangle$ biases closely follows that of SST biases (not shown). By examining Figs. 1g–h, we would argue that the stronger BSISO variability in SPK-OBS than in SPK-SPC may be related to the enhanced meridional

gradients of SST and moisture. Weaker propagating BSISO signal in SPC seems to be associated with the reduced horizontal $\langle m \rangle$ advection of mean $\langle m \rangle$ induced by anomalous wind.

In CGCMs with dynamic oceans, it is also important to consider the effect of interannual SST variability (such as the ENSO), due to its strong control on sub-seasonal variability, particularly on the boreal winter MJO (Weaver et al., 2011; Kapur and Zhang, 2012; Klingaman and DeMott, 2020). We note that none of the simulations considered here represent the ENSO or other coupled modes of interannual variability, as the MC-KPP ocean model lacks the requisite ocean dynamics. Using the same simulations, Klingaman and DeMott (2020) found that the intensity and propagation of the boreal winter MJO was strongly suppressed in SPCAM3-KPP under the SPC ocean mean state, while here the SPC ocean mean state enhances BSISO amplitude and only slightly weakens its propagation. Klingaman and DeMott (2020) found that the inclusion of the SPC ENSO variability on top of the SPC mean state substantially strengthened the MJO, suggesting that the strong MJO in SPC arose from an excessively intense response to the ENSO. The effect of ENSO is not considered here, which could be a subject for further study.

5 Summary

We investigate the roles of ocean mean-state biases and air-sea coupling in simulating the BSISO by coupling the SPCAM3 to the MC-KPP mixed-layer ocean. To diagnose the sensitivity to the ocean mean state, SPCAM3-KPP is constrained to either observed ocean mean state or the ocean mean state from the coupled configuration of SPCAM3 with a dynamic ocean (SPC). The SPC mean state introduces substantial cold SST biases across the Indo-Pacific. To diagnose the sensitivity to air-sea coupling under different mean states, SPCAM3 is driven by the 31-day running mean SST from each SPCAM3-KPP simulation.

Systematic errors in SPCAM3 result in overestimated subtropical summer mean rainfall and intraseasonal variability. These overestimated variables are greatly improved with coupling, or with the SPC ocean mean state. Lag regression composites show that the simulated convection exhibits realistic northward propagation over both the Indian Ocean and western Pacific. However, the strongest convective center shifts north relative to the observation. Using the SPC ocean mean state degrades the propagating BSISO signal in both coupled and uncoupled simulations, relative to the simulations that use the observed ocean mean state. Air-sea coupling slightly enhances the strength of the propagating signal under both ocean mean states. The coupled simulations capture the SST-rainfall phase relationship reasonably well, but with warm SSTs shifting toward the suppressed convection over the Bay of Bengal relative to the observation. Intraseasonal SST variability plays a similar role in the BSISO MSE budget in the coupled simulations, regardless of the ocean mean state: it damps subtropical convection and favours BSISO northward propagation, but with a smaller contribution (8–12%) than the reanalysis (12–20%).

We also examine the simulation skill of propagating BSISO characteristics by using BSISO indices. Experiments with the observed ocean mean state produce a realistic annual cycle of BSISO variance, while the simulations with the SPC mean state result in a one-month delay of the onset of BSISO activity. Air-sea coupling weakens convective variability mainly through

suppressing the first EOF mode. Different from the observation, all model simulations favour strong BSISO activity in off-equatorial regions, which is associated with intense subtropical variability. Overall, the simulations using the SPC ocean mean state produce an improved BSISO than those using the observed ocean mean state, in terms of both amplitude and pattern correlation of anomalous precipitation. Air-sea coupling improves the BSISO fidelity in most phases. The enhancement of simulated BSISO by the ocean mean state and air-sea coupling largely arises from suppressing erroneously strong subtropical convection.

In our study, air-sea coupling has a similar effect on the simulated BSISO under different ocean background states, suggesting that the role of coupling may largely depend on the phase relationship between the convection and SST anomalies. Compared to daily coupling frequency between the atmosphere and ocean components of CGCMs, improved fidelity for the BSISO simulation is shown in CGCMs with sub-daily coupling frequency (Woolnough et al., 2007; Klingaman et al., 2011; Hu et al., 2015). In our study, the model ocean tends to respond quickly to the atmospheric convection, which may be associated with the sensitive mixed layer depth due to the absent ocean dynamics in KPP. Therefore, to better understand the role of coupling in the simulated ISO, efforts should be aimed at simulating a realistic phase relationship between the ISO convection and SST anomalies.

Code and data availability. All model outputs are available on the U.K. JASMIN collaborative research analysis facility (http://www.jasmin.ac.uk). Access to data can be obtained by contacting Nicholas Klingaman (nicholas.klingaman@ncas.ac.uk). Data used to reproduce the figures and associated code can be found at https://doi.org/10.6084/m9.figshare.c.4874406.v2

Competing interests: The authors have no competing interests to declare.

Author contributions. YG and PCH developed the codes, conducted analyses, and wrote the manuscript. NPK and CAD designed and performed SPCAM3-KPP simulations presented in the paper. All authors gave comments and contributed to the development of the manuscript.

Competing interests. The authors declare that they have no conflict of interest.

Acknowledgements. YG and PCH are supported by the National Key R&D Program of China (2018YFC1505804) and NUIST-UoR Open Project. NPK is supported by an Independent Research Fellowship from the UK Natural Environment Research Council (NE/L010976/1) and a grant from the NOAA Modeling, Analysis, Predictions and Projections program (NA16OAR4310071). CAD is supported by the National Science Foundation (NSF 1445191) and the NOAA Modeling, Analysis, Predictions and Projections program (NA16OAR4310094). ERAI reanalysis data are obtained from http://apps.ecmwf.int/datasets.

References

Annamalai, H. and Slingo, J. M.: Active / break cycles: Diagnosis of the intraseasonal variability of the Asian summer monsoon, Clim. Dyn., 18(1–2), 85–102, https://doi.org/10.1007/s003820100161, 2001.

Annamalai, H. and Sperber, K. R.: Regional heat sources and the active and break phases of boreal summer intraseasonal (30–50 day) variability, J. Atmos. Sci., 62(8), 2726–2748, https://doi.org/10.1175/JAS3504.1, 2005.

Benedict, J. J. and Randall, D. A.: Structure of the Madden–Julian oscillation in the superparameterized CAM, J. Atmos. Sci., 66(11), 3277–3296, https://doi.org/10.1175/2009JAS3030.1, 2009.

Bernie, D. J., Woolnough, S. J., Slingo, J. M. and Guilyardi, E.: Modeling diurnal and intraseasonal variability of the ocean mixed layer, J. Climate, 18(8), 1190–1202, https://doi.org/10.1175/JCLI3319.1, 2005.

Bollasina, M. A. and Ming, Y.: The general circulation model precipitation bias over the southwestern equatorial Indian Ocean and its implications for simulating the South Asian monsoon, Clim. Dyn., 40(3–4), 823–838, https://doi.org/10.1007/s00382-012-1347-7, 2013.

Danabasoglu, G., Large, W. G., Tribbia, J. J., Gent, P. R., Briegleb, B. P., and McWilliams, J. C.: Diurnal coupling in the tropical oceans of CCSM3, J. Climate, 19(11), 2347–2365, 2006.

Dee, D. P., Uppala, S. M., Simmons, A. J., Berrisford, P., Poli, P., Kobayashi, S., Andrae, U., Balmaseda, M. A., Balsamo, G., Bauer, P., Bechtold, P., Beljaars, A. C. M., van de Berg, L., Bidlot, J., Bormann, N., Delsol, C., Dragani, R., Fuentes, M., Geer, A. J., Haimberger, L., Healy, S. B., Hersbach, H., Hólm, E. V., Isaksen, L., Kållberg, P., Köhler, M., Matricardi, M., McNally, A. P., Monge-Sanz, B. M., Morcrette, J.-J., Park, B.-K., Peubey, C., de Rosnay, P., Tavolato, C., Thépaut, J.-N. and Vitart, F.: The ERA-Interim reanalysis: Configuration and performance of the data assimilation system, Q. J. Roy. Meteorol. Soc. 137(656), 553–597, https://doi.org/10.1002/qj.828, 2011.

DeMott, C. A., Stan, C., Randall, D. A., Kinter, J. L. and Khairoutdinov, M.: The Asian monsoon in the superparameterized CCSM and Its relationship to tropical wave activity, J. Climate, 24(19), 5134–5156, https://doi.org/10.1175/2011JCLI4202.1, 2011.

DeMott, C. A., Stan, C., Randall, D. A. and Branson, M. D.: Intraseasonal variability in coupled GCMs: The roles of ocean feedbacks and model physics, J. Climate, 27(13), 4970–4995, https://doi.org/10.1175/JCLI-D-13-00760.1, 2014.

DeMott, C. A., Klingaman, N. P., Tseng, W.-L., Burt, M. A., Gao, Y., and Randall, D. A.: The convection connection: How ocean feedbacks affect tropical mean moisture and MJO propagation, J. Geophys. Res. Atmos., 124(22), 11910–11931, https://doi.org/10.1029/2019JD31015, 2019.

DeMott, C. A., Klingaman, N. P. and Woolnough, S. J.: Atmosphere-ocean coupled processes in the Madden-Julian oscillation, Rev. Geophys., 53(4), 1099–1154, https://doi.org/10.1002/2014RG000478, 2015.

DeMott, C. A., Benedict, J. J., Klingaman, N. P., Woolnough, S. J. and Randall, D. A.: Diagnosing ocean feedbacks to the MJO: SST-modulated surface fluxes and the moist static energy budget, J. Geophys. Res. Atmos., 121(14), 8350–8373, https://doi.org/10.1002/2016JD025098, 2016.

Ding, Q. and Wang, B.: Intraseasonal teleconnection between the summer Eurasian wave train and the Indian monsoon, J. Climate, 20(15), 3751–3767, https://doi.org/10.1175/JCLI4221.1, 2007.

Fu, X. and Wang, B.: Differences of boreal summer intraseasonal oscillations simulated in an atmosphere–ocean coupled model and an atmosphere-only model, J. Climate, 17, 1263–1271, 2004.

Gao, Y., Klingaman, N. P., DeMott, C. A. and Hsu, P.: Diagnosing ocean feedbacks to the BSISO: SST-modulated surface fluxes and the moist static energy budget, J. Geophys. Res. Atmos., 124, 146–170, https://doi.org/10.1029/2018JD029303, 2019.

Hendon, H. H.: Impact of air–sea coupling on the Madden–Julian oscillation in a general circulation model, J. Atmos. Sci., 57(24), 3939–3952, https://doi.org/10.1175/1520-0469(2001)058<3939:IOASCO>2.0.CO;2, 2000.

Hirons, L. C., Klingaman, N. P. and Woolnough, S. J.: MetUM-GOML1: a near-globally coupled atmosphere–ocean-mixed-layer model, Geosci. Model Dev., 8(2), 363–379, https://doi.org/10.5194/gmd-8-363-2015, 2015.

Hsu, P.-C., and Li, T.: Role of the boundary layer moisture asymmetry in causing the eastward propagation of the Madden-Julian Oscillation. J. Climate, 25, 4914–4931, https://doi.org/10.1175/JCLI-D-11-00310.1, 2012.

Hsu, P.-C., Lee, J.-Y. and Ha, K.-J.: Influence of boreal summer intraseasonal oscillation on rainfall extremes in southern China, Int. J. Climatol., 36(3), 1403–1412, https://doi.org/10.1002/joc.4433, 2016.

Hsu, P.-C., Lee, J.-Y., Ha, K.-J. and Tsou, C.-H.: Influences of boreal summer intraseasonal oscillation on heat waves in monsoon Asia, J. Climate, 30(18), 7191–7211, https://doi.org/10.1175/JCLI-D-16-0505.1, 2017.

Hsu, P.-C., Qian, Y., Liu, Y., Murakami, H. and Gao, Y.: Role of abnormally enhanced MJO over the Western Pacific in the formation and subseasonal predictability of the record-breaking Northeast Asian heatwave in the summer of 2018. J. Climate, 33, 3333–3349, https://doi.org/10.1175/JCLI-D-19-0337.1, 2020.

Hu, W., Duan, A. and Wu, G.: Impact of subdaily air–sea interaction on simulating intraseasonal oscillations over the tropical Asian monsoon region, J. Climate, 28(3), 1057–1073, https://doi.org/10.1175/JCLI-D-14-00407.1, 2015.

Hu, W., Duan, A. and He, B.: Evaluation of intra-seasonal oscillation simulations in IPCC AR5 coupled GCMs associated with the Asian summer monsoon, Int. J. Climatol., 37, 476–496, https://doi.org/10.1002/joc.5016, 2017.

Huffman, G. J., Adler, R. F., Morrissey, M. M., Bolvin, D. T., Curtis, S., Joyce, R., McGavock, B., and Susskind, J.: Global Precipitation at One-Degree Daily Resolution from Multisatellite Observations, J. Hydrometeorol., 2, 36–50, https://doi.org/10.1175/1525-7541(2001)002<0036:GPAODD>2.0.CO;2, 2001.

Inness, P. M., Slingo, J. M., Guilyardi, E. and Cole, J.: Simulation of the Madden–Julian oscillation in a coupled general circulation model. Part II: The role of the basic state, J. Climate, 16(3), 365–382, https://doi.org/10.1175/1520-0442(2003)016<0365:SOTMJO>2.0.CO;2, 2003.

Jiang, X.: Key processes for the eastward propagation of the Madden-Julian Oscillation based on multimodel simulations. J. Geophys. Res. Atmos., 122, 755–770, https://doi.org/10.1002/2016JD025955, 2017.

Jiang, X., Adames, A. F., Zhao, M., Waliser, D., and Maloney, E.: A unified moisture moist framework for seasonality of MJO propagation. J. Climate, 31, 4215–4224, https://doi.org/10.1175/JCLI-D-17-0671.1, 2018.

Jiang, X., Waliser, D. E., Xavier, P. K., Petch, J., Klingaman, N. P., Woolnough, S. J., Guan, B., Bellon, G., Crueger, T., DeMott, C., Hannay, C., Lin, H., Hu, W., Kim, D., Lappen, C.-L., Lu, M.-M., Ma, H.-Y., Miyakawa, T., Ridout, J. A., Schubert, S. D., Scinocca, J., Seo, K.-H., Shindo, E., Song, X., Stan, C., Tseng, W.-L., Wang, W., Wu, T., Wu, X., Wyser, K., Zhang, G. J. and Zhu, H.: Vertical structure and physical processes of the Madden-Julian oscillation: Exploring key model physics in climate simulations, J. Geophys. Res. Atmos., 120(10), 4718–4748, https://doi.org/10.1002/2014JD022375, 2015.

Jiang, X., Zhao, M., Maloney, E. D. and Waliser, D. E.: Convective moisture adjustment time scale as a key factor in regulating model amplitude of the Madden-Julian oscillation, Geophys. Res. Lett., 43(19), 10,412-10,419, https://doi.org/10.1002/2016GL070898, 2016.

Kapur, A. and Zhang, C.: Multiplicative MJO forcing of ENSO, J. Climate, 25(23), 8132–8147, https://doi.org/10.1175/JCLI-D-11-00609.1, 2012.

Kessler, W. S., McPhaden, M. J. and Weickmann, K. M.: Forcing of intraseasonal Kelvin waves in the equatorial Pacific, J. Geophys. Res., 100(C6), 10613–10631, https://doi.org/10.1029/95JC00382, 1995.

Khairoutdinov, M., Randall, D. and DeMott, C.: Simulations of the atmospheric general circulation using a cloud-resolving model as a superparameterization of physical processes, J. Atmos. Sci., 62(7), 2136–2154, https://doi.org/10.1175/JAS3453.1, 2005.

Khairoutdinov, M. F. and Randall, D. A.: Cloud resolving modeling of the ARM summer 1997 IOP: Model formulation, results, uncertainties, and sensitivities, J. Atmos. Sci., 60(4), 607–625, https://doi.org/10.1175/1520-0469(2003)060<0607:CRMOTA>2.0.CO;2, 2003.

Klingaman, N. P. and DeMott, C. A.: Mean state biases and interannual variability affect perceived sensitivities of the Madden-Julian oscillation to air-sea coupling, J. Adv. Model. Earth Syst., 12, e2019MS001799, https://doi.org/10.1029/2019MS001799, 2020.

Klingaman, N. P. and Woolnough, S. J.: The role of air-sea coupling in the simulation of the Madden-Julian oscillation in the Hadley Centre model, Q. J. Roy. Meteorol. Soc., 140(684), 2272–2286, https://doi.org/10.1002/qj.2295, 2014.

Klingaman, N. P., Woolnough, S. J., Weller, H. and Slingo, J. M.: The impact of finer-resolution air–sea coupling on the intraseasonal oscillation of the Indian monsoon, J. Climate, 24(10), 2451–2468, https://doi.org/10.1175/2010JCLI3868.1, 2011.

Large, W., McWilliams, J., and Doney, S.: Oceanic vertical mixing: A review and a model with a nonlocal boundary layer parameterization. Rev. Geophys., 32, 363–403, 1994.

Lau, W. K. M. and Waliser, D. E.: Intraseasonal variability in the atmosphere-ocean climate system, 2. ed., Springer [u.a.], Berlin., 2012.

Lee, J.-Y., Wang, B., Wheeler, M. C., Fu, X., Waliser, D. E. and Kang, I.-S.: Real-time multivariate indices for the boreal summer intraseasonal oscillation over the Asian summer monsoon region, Clim. Dyn., 40(1–2), 493–509, https://doi.org/10.1007/s00382-012-1544-4, 2013.

Levine, R. C. and Turner, A. G.: Dependence of Indian monsoon rainfall on moisture fluxes across the Arabian Sea and the impact of coupled model sea surface temperature biases, Clim. Dyn., 38(11–12), 2167–2190, https://doi.org/10.1007/s00382-011-1096-z, 2012.

Li, J., Mao, J. and Wu, G.: A case study of the impact of boreal summer intraseasonal oscillations on Yangtze rainfall, Clim. Dyn., 44(9–10), 2683–2702, https://doi.org/10.1007/s00382-014-2425-9, 2015.

Liebmann, B, Smith, C. A.: Description of a complete (interpolated) outgoing long wave radiation dataset. Bull. Amer. Meteor. Soc., 77, 1275–1277, 1996.

Lin, J.-L., Kiladis, G. N., Mapes, B. E., Weickmann, K. M., Sperber, K. R., Lin, W., Wheeler, M. C., Schubert, S. D., Del Genio, A., Donner, L. J., Emori, S., Gueremy, J.-F., Hourdin, F., Rasch, P. J., Roeckner, E. and Scinocca, J. F.: Tropical intraseasonal variability in 14 IPCC AR4 climate models. Part I: Convective signals, J. Climate, 19(12), 2665–2690, https://doi.org/10.1175/JCLI3735.1, 2006.

Liu, Y., and Hus, P.-C.: Long-term changes in wintertime persistent heavy rainfall over southern China contributed by the Madden–Julian Oscillation. Atmos. and Oceanic Sci. Lett., 12, 361–368, https://doi.org/10.1080/16742834.2019.1639471, 2019.

Madden, R. A. and Julian, P. R.: Detection of a 40–50 Day Oscillation in the Zonal Wind in the Tropical Pacific, J. Atmos. Sci., 28(5), 702–708, https://doi.org/10.1175/1520-0469(1971)028<0702:DOADOI>2.0.CO;2, 1971.

Madden, R. A. and Julian, P. R.: Description of global-scale circulation cells in the tropics with a 40–50 day period, J. Atmos. Sci., 29(6), 1109–1123, https://doi.org/10.1175/1520-0469(1972)029<1109:DOGSCC>2.0.CO;2, 1972.

Maloney, E. D.: The moist static energy budget of a composite tropical intraseasonal oscillation in a climate model, J. Climate, 22(3), 711–729, https://doi.org/10.1175/2008JCLI2542.1, 2009.

Maloney, E. D. and Hartmann, D. L.: The sensitivity of intraseasonal variability in the NCAR CCM3 to changes in convective parameterization, J. Climate, 14(9), 2015–2034, https://doi.org/10.1175/1520-0442(2001)014<2015:TSOIVI>2.0.CO;2, 2001.

McPhaden, M. J.: Evolution of the 2002/2003 El Nino, Bull. Amer. Meteor. Soc., 85, 677–695, 2004.

Moon, J.-Y., Wang, B., Ha, K.-J. and Lee, J.-Y.: Teleconnections associated with Northern Hemisphere summer monsoon intraseasonal oscillation, Clim. Dyn., 40(11–12), 2761–2774, https://doi.org/10.1007/s00382-012-1394-0, 2013.

Misra, V., Marx, L., Brunke, M. and Zeng, X.: The equatorial Pacific cold tongue bias in a coupled climate model, J. Climate, 21(22), 5852–5869, https://doi.org/10.1175/2008JCLI2205.1, 2008.

Neena, J. M., Waliser, D. and Jiang, X.: Model performance metrics and process diagnostics for boreal summer intraseasonal variability, Clim. Dyn., 48(5–6), 1661–1683, https://doi.org/10.1007/s00382-016-3166-8, 2017.

Randall, D. A., Wood, R. A., Bony, S., Colman, R., Fichefet, T., Fyfe, J., Kattsov, V., Pitman, A., Shukla, J., Srinivasan, J., Stouffer, R. J., Sumi, A., Taylor, K. E., AchutaRao, K., Allan, R., Berger, A., Blatter, H., Bonfils, C., Boone, A., Bretherton, C., Broccoli, A., Brovkin, V., Dirmeyer, P., Doutriaux, C., Drange, H., Frei, A., Ganopolski, A., Gent, P., Gleckler, P., Goosse, H., Graham, R., Gregory, J. M., Gudgel, R., Hall, A., Hallegatte, S., Hasumi, H., Henderson-Sellers, A., Hendon, H., Hodges, K., Holland, M., Holtslag, A. A. M., Hunke, E., Huybrechts, P., Ingram, W., Joos, F., Kirtman, B., Klein, S., Koster, R.,

Kushner, P., Lanzante, J., Latif, M., Pavlova, T., Federationi, R., Petoukhov, V., Phillips, T., Power, S., Rahmstorf, S., Raper, S. C. B., Renssen, H., Rind, D., Roberts, M., Rosati, A., Schär, C., Schmittner, A., Scinocca, J., Seidov, D., Slater, A. G., Slingo, J., Smith, D., Soden, B., Stern, W., Stone, D. A., Sudo, K., Takemura, T., Tselioudis, G., Webb, M., Wild, M., Manzini, E., Matsuno, T. and McAvaney, B.: Climate models and their evaluation, , 74, 2007.

Ren, X., Yang, X.-Q. and Sun, X.: Zonal oscillation of western Pacific subtropical high and subseasonal SST variations during Yangtze persistent heavy rainfall events, J. Climate, 26(22), 8929–8946, https://doi.org/10.1175/JCLI-D-12-00861.1, 2013.

Sabeerali, C. T., Ramu Dandi, A., Dhakate, A., Salunke, K., Mahapatra, S. and Rao, S. A.: Simulation of boreal summer intraseasonal oscillations in the latest CMIP5 coupled GCMs, J. Geophys. Res. Atmos., 118(10), 4401–4420, https://doi.org/10.1002/jgrd.50403, 2013.

Seo, K.-H., Schemm, J.-K. E., Wang, W. and Kumar, A.: The boreal summer intraseasonal oscillation simulated in the NCEP climate forecast system: The effect of sea surface temperature, Mon. Weather Rev., 135(5), 1807–1827, https://doi.org/10.1175/MWR3369.1, 2007.

Smith, D. M. and Murphy, J. M.: An objective ocean temperature and salinity analysis using covariances from a global climate model, J. Geophys. Res., 112(C2), C02022, https://doi.org/10.1029/2005JC003172, 2007.

Sperber, K. R. and Annamalai, H.: Coupled model simulations of boreal summer intraseasonal (30–50 day) variability, Part 1: Systematic errors and caution on use of metrics, Clim. Dyn., 31(2–3), 345–372, https://doi.org/10.1007/s00382-008-0367-9, 2008.

Sperber, K. R., Slingo, J. M. and Annamalai, H.: Predictability and the relationship between subseasonal and interannual variability during the Asian summer monsoon, Q. J. Roy. Meteorol. Soc., 126(568), 2545–2574, https://doi.org/10.1002/qj.49712656810, 2000.

Sperber, K. R., Gualdi, S., Legutke, S. and Gayler, V.: The Madden–Julian oscillation in ECHAM4 coupled and uncoupled general circulation models, Clim. Dyn., 25(2–3), 117–140, https://doi.org/10.1007/s00382-005-0026-3, 2005.

Sperber, K. R., Annamalai, H., Kang, I.-S., Kitoh, A., Moise, A., Turner, A., Wang, B. and Zhou, T.: The Asian summer monsoon: an intercomparison of CMIP5 vs. CMIP3 simulations of the late 20th century, Clim. Dyn., 41(9–10), 2711–2744, https://doi.org/10.1007/s00382-012-1607-6, 2013.

Stan, C.: The role of SST variability in the simulation of the MJO, Clim. Dyn., 51(7–8), 2943–2964, https://dor.org/10.1007/s00382-017-4058-2, 2018.

Stan, C., Khairoutdinov, M., DeMott, C. A., Krishnamurthy, V., Straus, D. M., Randall, D. A., Kinter, J. L. and Shukla, J.: An ocean-atmosphere climate simulation with an embedded cloud resolving model, Geophys. Res. Lett., 37(1), L01702, https://doi.org/10.1029/2009GL040822, 2010.

Waliser, D. E., Jin, K., Kang, I.-S., Stern, W. F., Schubert, S. D., Wu, M. L. C., Lau, K.-M., Lee, M.-I., Krishnamurthy, V., Kitoh, A., Meehl, G. A., Galin, V. Y., Satyan, V., Mandke, S. K., Wu, G., Liu, Y. and Park, C.-K.: AGCM simulations of intraseasonal variability associated with the Asian summer monsoon, Clim. Dyn., 21(5–6), 423–446, https://doi.org/10.1007/s00382-003-0337-1, 2003.

Waliser, D. E., Lau, K. M. and Kim, J.-H.: The influence of coupled sea surface temperatures on the Madden-Julian Oscillation: A model perturbation experiment, J. Atmos. Sci., 56, 333–358, 1999.

Wang, B., Webster, P. J. and Teng, H.: Antecedents and self-induction of active-break south Asian monsoon unraveled by satellites, Geophys. Res. Lett., 32(4), L04704, https://doi.org/10.1029/2004GL020996, 2005.

Wang, B., Webster, P., Kikuchi, K., Yasunari, T. and Qi, Y.: Boreal summer quasi-monthly oscillation in the global tropics, Clim. Dyn., 27(7–8), 661–675, https://doi.org/10.1007/s00382-006-0163-3, 2006.

Weare, B. C., Strub, P. T. and Samuel, M. D.: Annual mean surface heat fluxes in the tropical Pacific ocean, J. Phys. Oceanogr., 11(5), 705–717, https://doi.org/10.1175/1520-0485(1981)011<0705:AMSHFI>2.0.CO;2, 1981.

Weaver, S. J., Wang, W., Chen, M. and Kumar, A.: Representation of MJO variability in the NCEP climate forecast system, J. Climate, 24(17), 4676–4694, https://doi.org/10.1175/2011JCLI4188.1, 2011.

Wheeler, M. and Kiladis, G. N.: Convectively coupled equatorial waves: Analysis of clouds and temperature in the wavenumber–frequency domain, J. Atmos. Sci., 56(3), 374–399, https://doi.org/10.1175/1520-0469(1999)056<0374:CCEWAO>2.0.CO;2, 1999.

Woolnough, S. J., Vitart, F. and Balmaseda, M. A.: The role of the ocean in the Madden–Julian oscillation: Implications for MJO prediction, Q. J. Roy. Meteorol. Soc., 133(622), 117–128, https://doi.org/10.1002/qj.4, 2007.

Wu, X., Deng, L., Song, X., Vettoretti, G., Peltier, W. R. and Zhang, G. J.: Impact of a modified convective scheme on the Madden-Julian Oscillation and El Niño-Southern Oscillation in a coupled climate model, Geophys. Res. Lett., 34(16), L16823, https://doi.org/10.1029/2007GL030637, 2007.

Yasunari, T.: Cloudiness fluctuations associated with the northern summer monsoon, J. Meteorol. Soc. Japan, 57(3), 16, 1979.

Zhang, C.: Madden-Julian oscillation, Rev. Geophys., 43, RG2003, https://doi.org/10.1029/2004RG000158, 2005.

Zhang, C. and Gottschalck, J.: SST anomalies of ENSO and the Madden–Julian oscillation in the equatorial Pacific, J. Climate, 15(17), 2429–2445, https://doi.org/10.1175/1520-0442(2002)015<2429:SAOEAT>2.0.CO;2, 2002.

Table 1: List of simulations analysed in this study, including the experiment name, model, ocean climatology condition used by the model to constrain (coupled model) or as forcing (atmospheric-only model), and design purpose.

Exp	Model	Ocean surface	Purpose
SPK-OBS	SPCAM3-KPP	SST climatology from observation	Understanding ocean mean-state bias effect (SPK-OBS vs. SPK-SPC)
SPK-SPC	SPCAM3-KPP	SST climatology from SPC	
SPA-KOBS	SPCAM3	31-day smoothed SST from SPK-OBS	Understanding air-sea coupling effect under observed mean state (vs. SPK-OBS)
SPA-KSPC	SPCAM3	31-day smoothed SST from SPK-SPC	Understanding air-sea coupling effect under SPC mean state (vs. SPK-SPC)

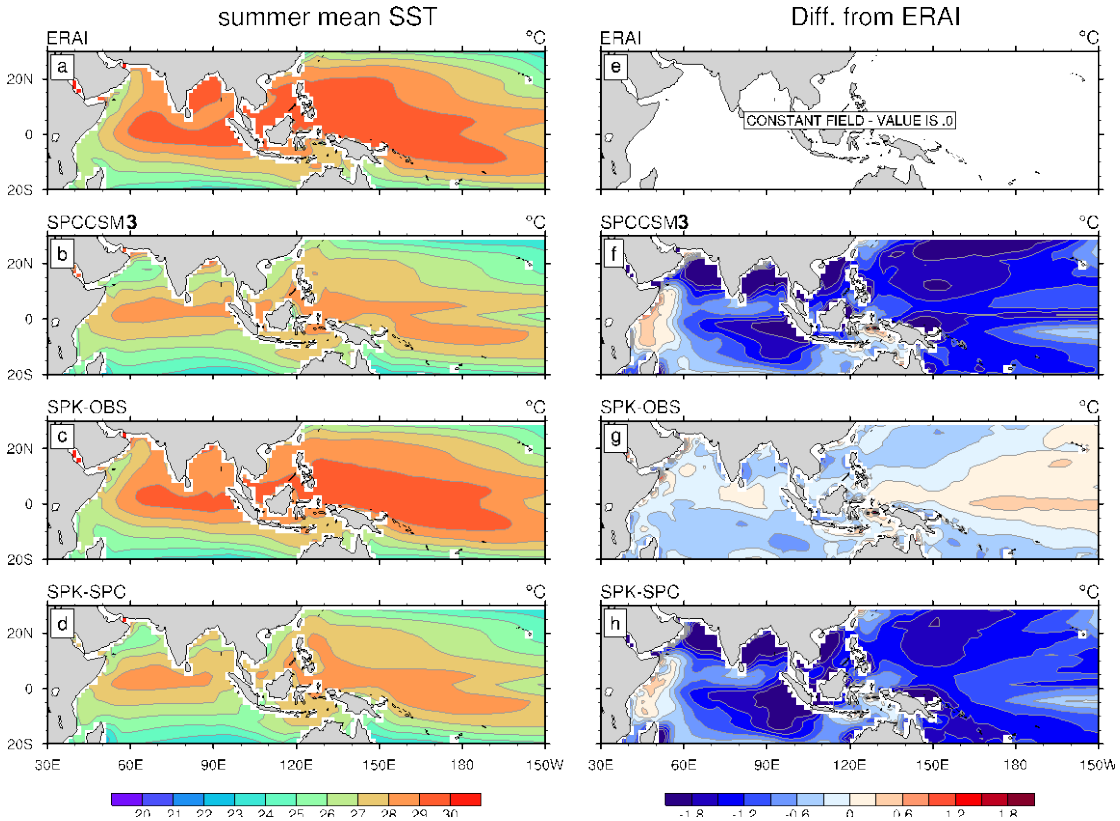

580

Figure 1: May–October mean SST for (a) ERAI, (b) SPCCSM3, (c) SPK-OBS, and (d) SPK-SPC. (f)–(h) are calculated differences between (b)–(d) and (a).

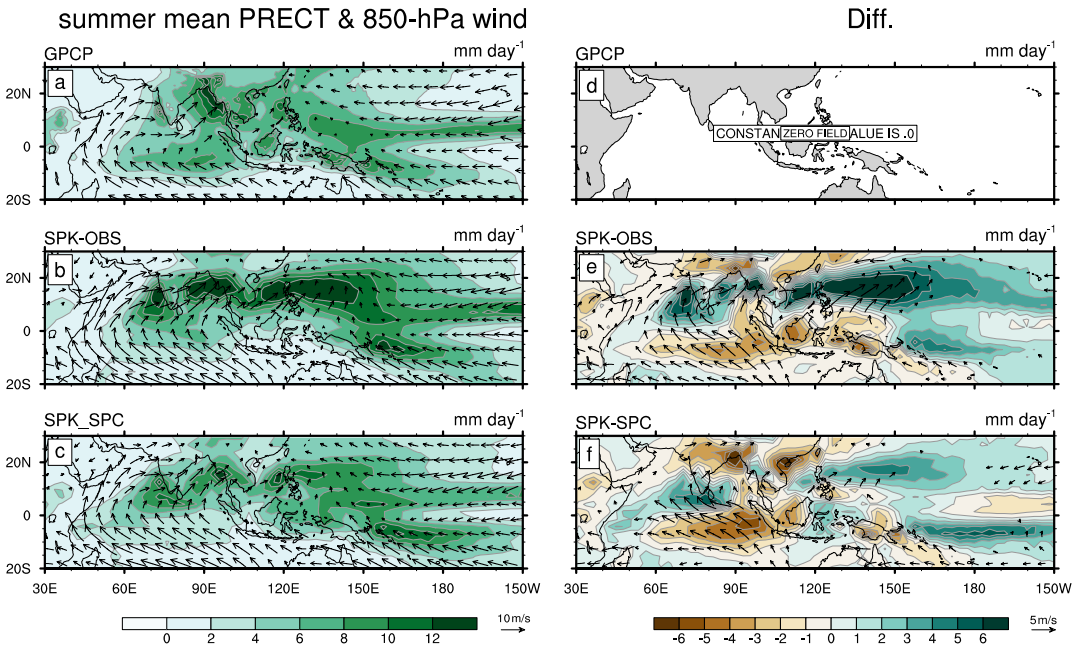

585 **Figure 2:** May–October mean precipitation (shading) and 850-hPa wind (vector; with amplitude > 3.5 m s^{-1}) for (a) GPCP precipitation and ERAI 850-hPa wind, (b) SPK-OBS and (c) SPK-SPC. (e)–(f) are calculated differences between (b)–(c) and (a).

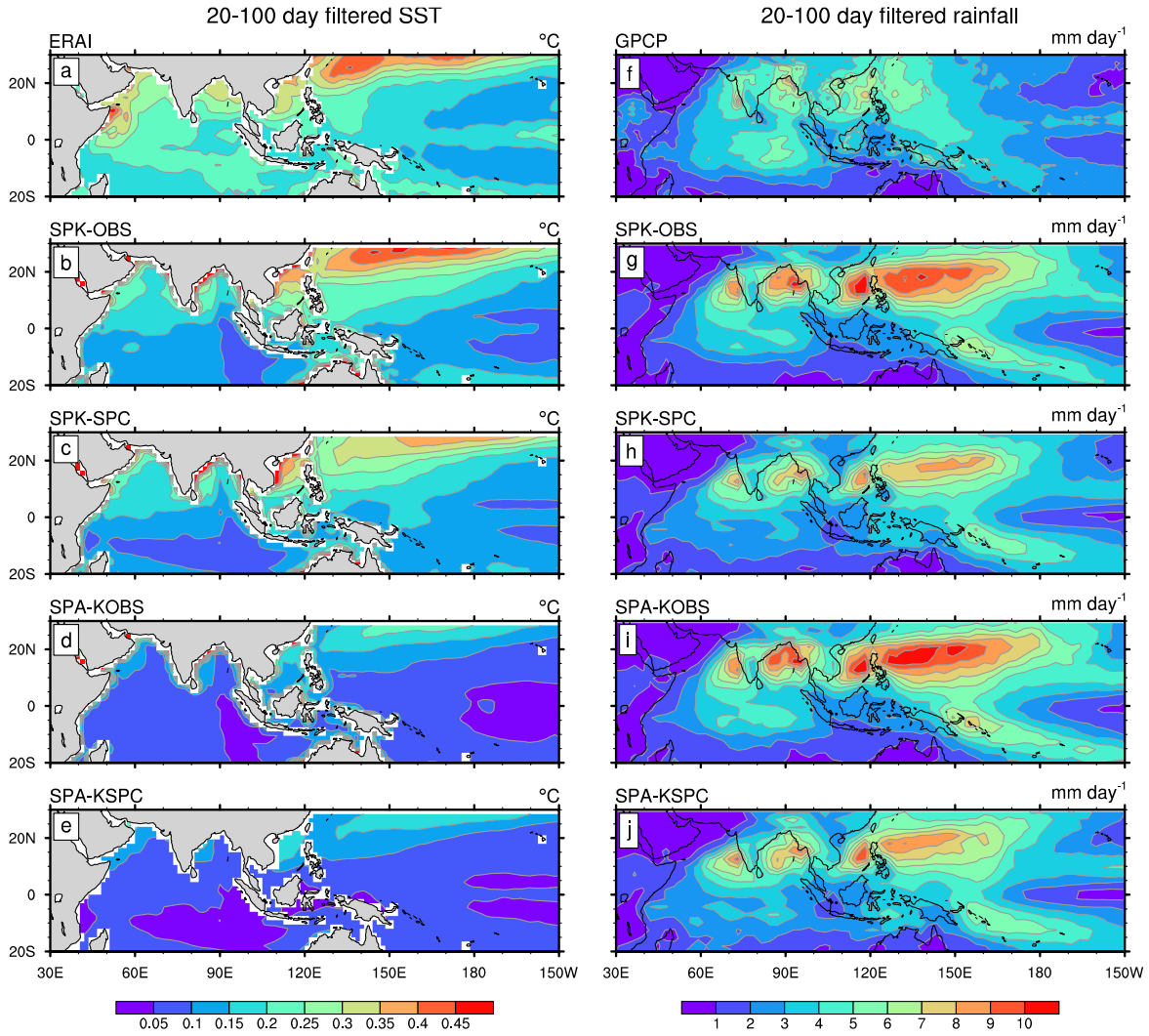

590 **Figure 3:** May–October standard deviations of 20–100-day-filtered (left column) SST and (right column) precipitation for (a, f) ERAI SST and GPCP precipitation, (b, g) SPK-OBS, (c, h) SPK-SPC, (d, i) SPA-KOBS, and (e, j) SPA-KSPC.

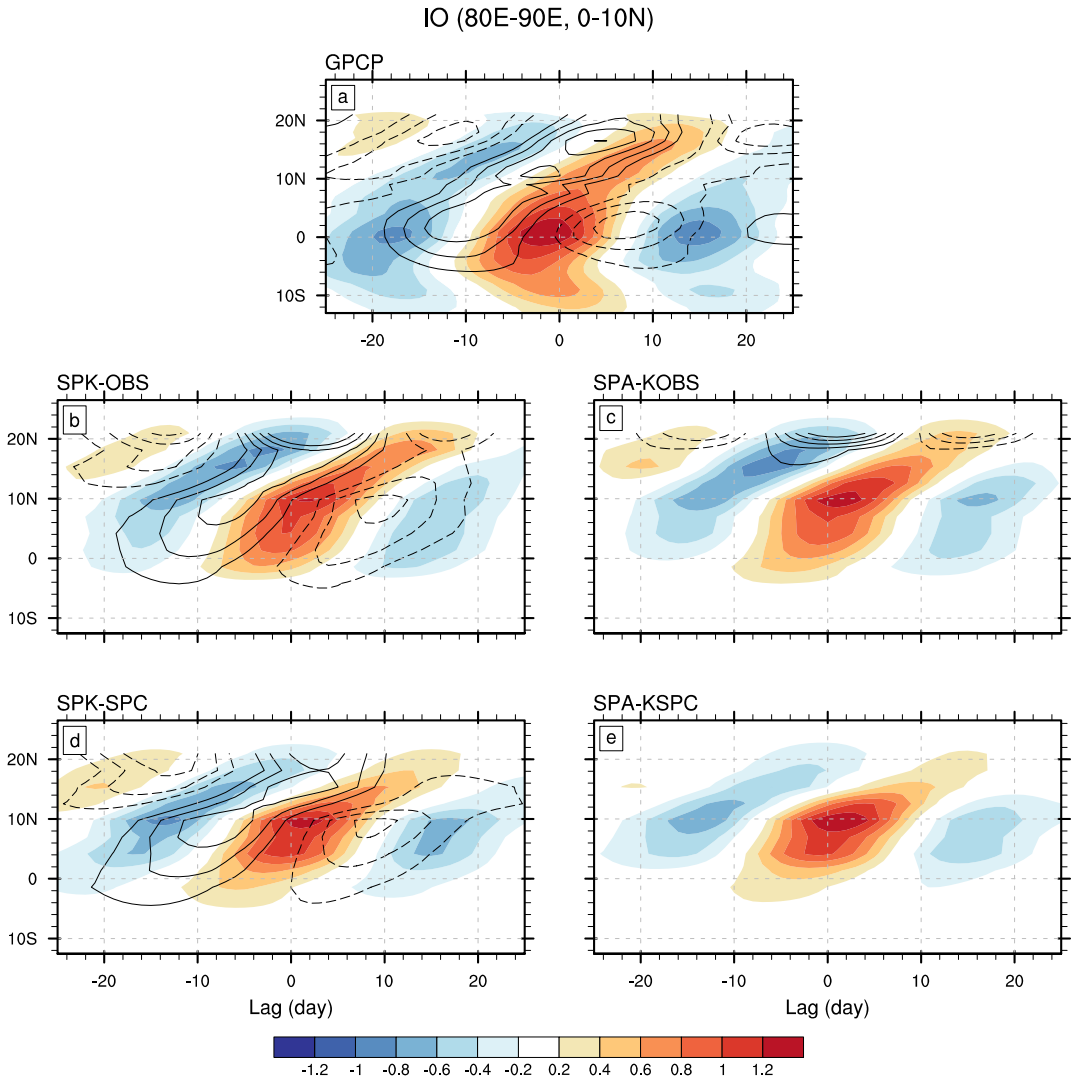

Figure 4: Lagged regression coefficients of 80°–90°E averaged intraseasonal precipitation (shading; [mm day^{-1}]/[mm day^{-1}]) and SST (contour; [ºC]/[mm day^{-1}]) onto (80°–90°E, 0°–10°N) averaged intraseasonal precipitation for (a) GPCP precipitation and ERAI SST, (b) SPK-OBS, (c) SPA-KOBS, (d) SPK-SPC, and (e) SPA-KSPC. Contour interval is 0.001 [ºC]/[mm day^{-1}], and zero contour is omitted.

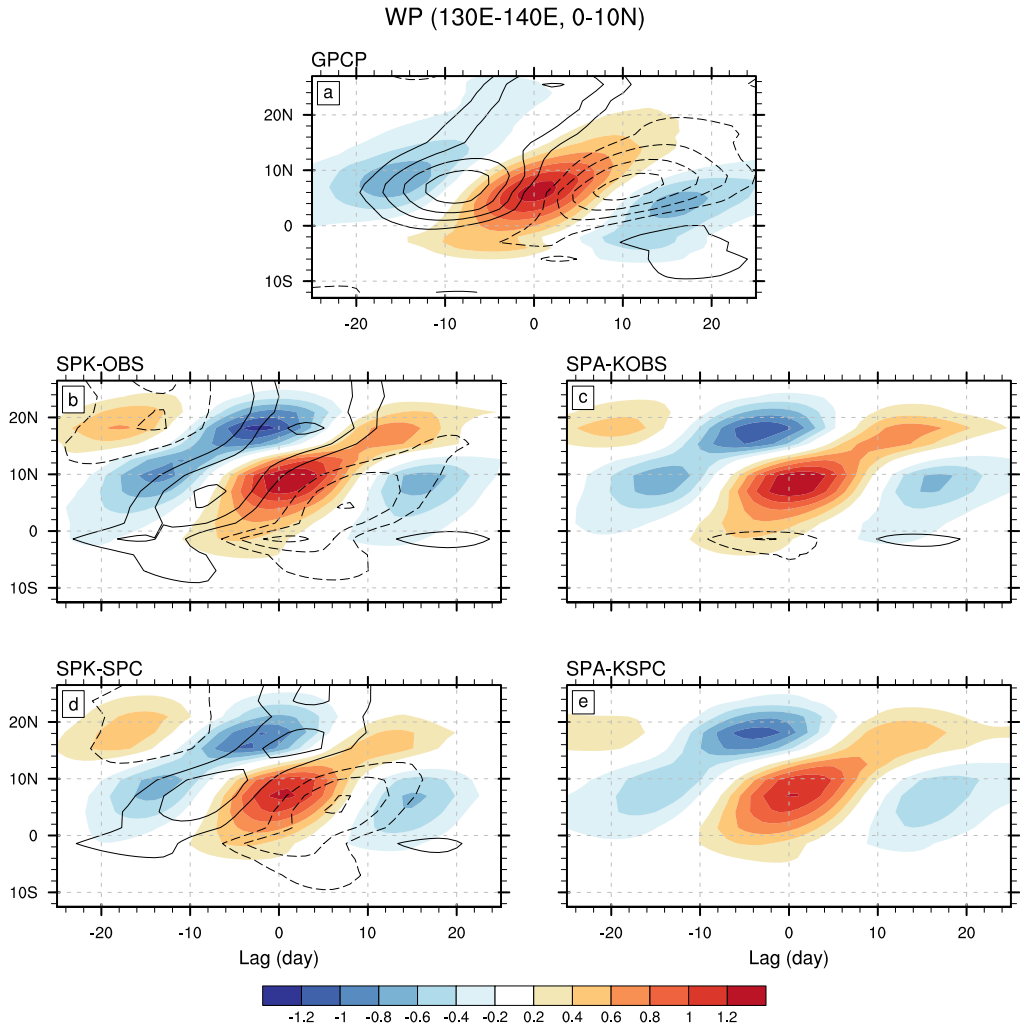

Figure 5: Same as Fig. 4, except for 130°–140°E averaged intraseasonal precipitation and SST regressed onto (130°–140°E, 0°–10°N) averaged intraseasonal precipitation.

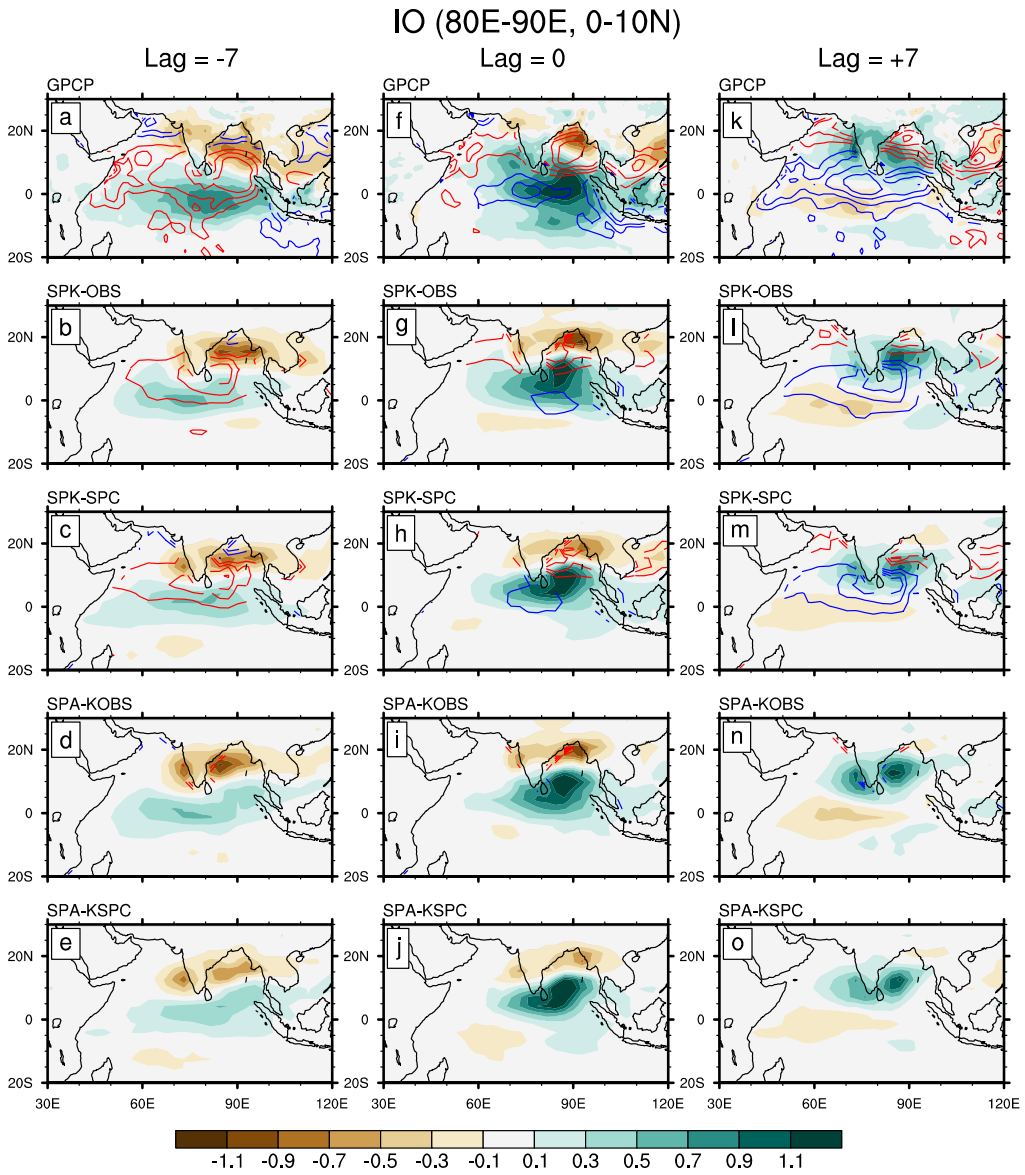

Figure 6: Regression coefficients of intraseasonal precipitation (shading; [mm day^{-1}]/[mm day^{-1}]) and SST (contour; [℃]/[mm day^{-1}]) onto (80°–90°E, 0°–10°N) averaged intraseasonal precipitation over the Indian Ocean at lags of (left column) -7, (middle column) 0 and (right column) +7 days, for (a, f, k) GPCP precipitation and ERAI SST, (b, g, l) SPK-OBS, (c, h, m) SPK-SPC, (d, i, n) SPA-KOBS, and (e, j, o) SPA-KSPC. The contour interval is 0.01 [℃]/[mm day^{-1}]; positive (negative) values are represented by red (blue) lines.

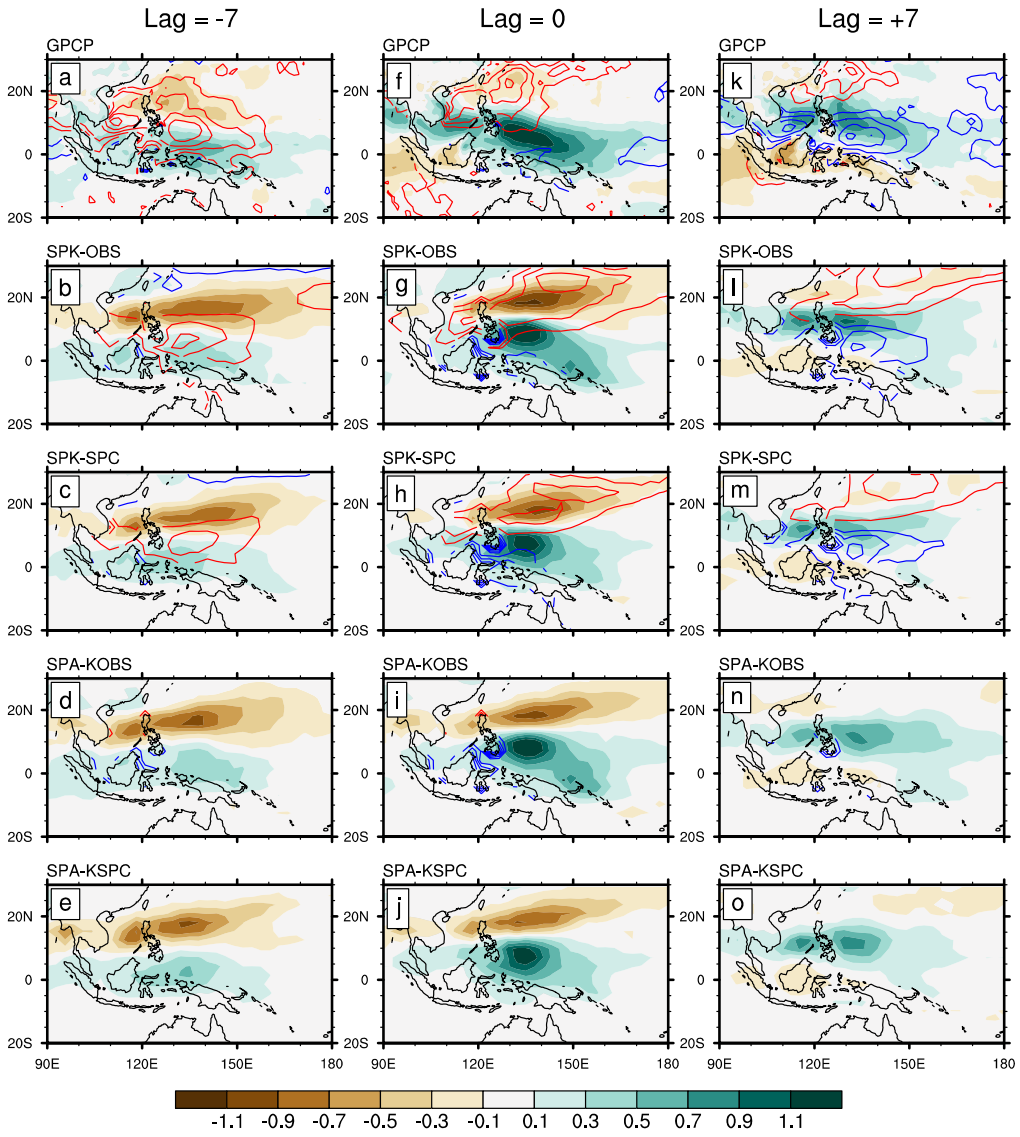

Figure 7: Same as Fig. 6, except for variables regressed onto (130°–140°E, 0°–10°N) averaged intraseasonal precipitation over the western Pacific.

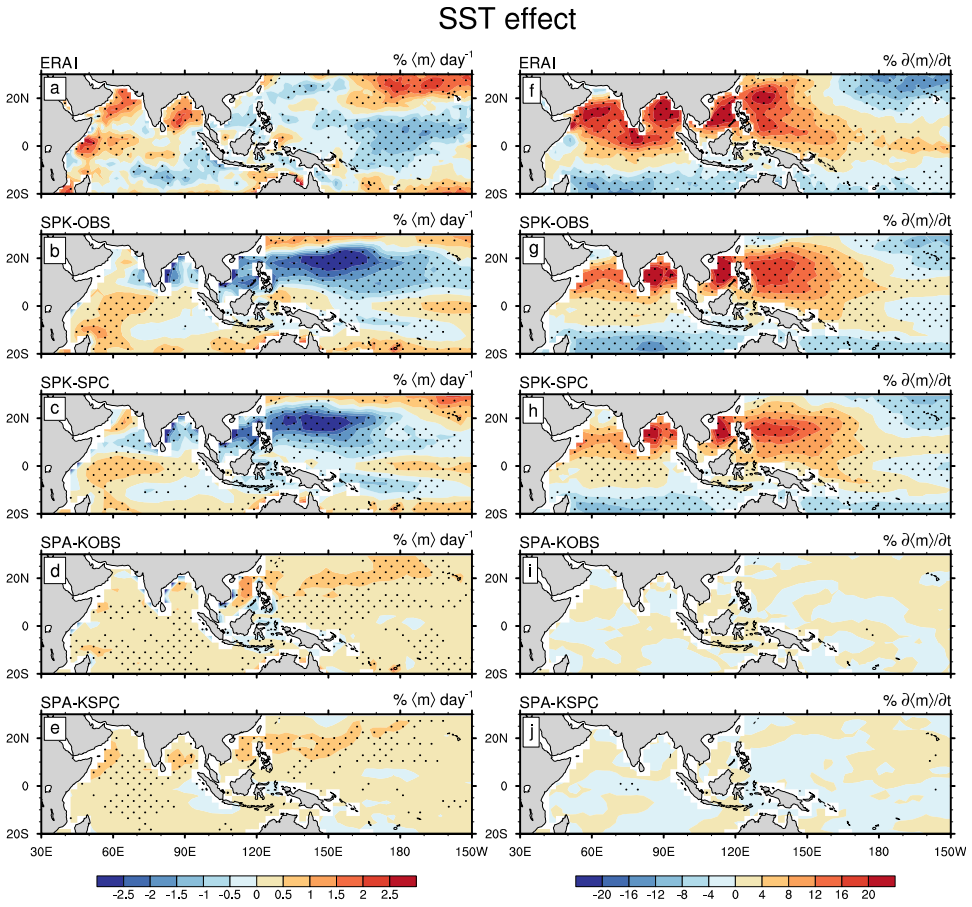

Figure 8: SST effect on (left column) $\langle \boldsymbol{m} \rangle$ and (right column) $\boldsymbol{\partial \langle m \rangle / \partial t}$ through the modification of surface turbulent fluxes for (a, f) ERAI, (b, g) SPK-OBS, (c, h) SPK-SPC, (d, i) SPA-KOBS, and (e, j) SPA-KSPC. Stippling indicates regression coefficient is significant at the 95% confidence level.

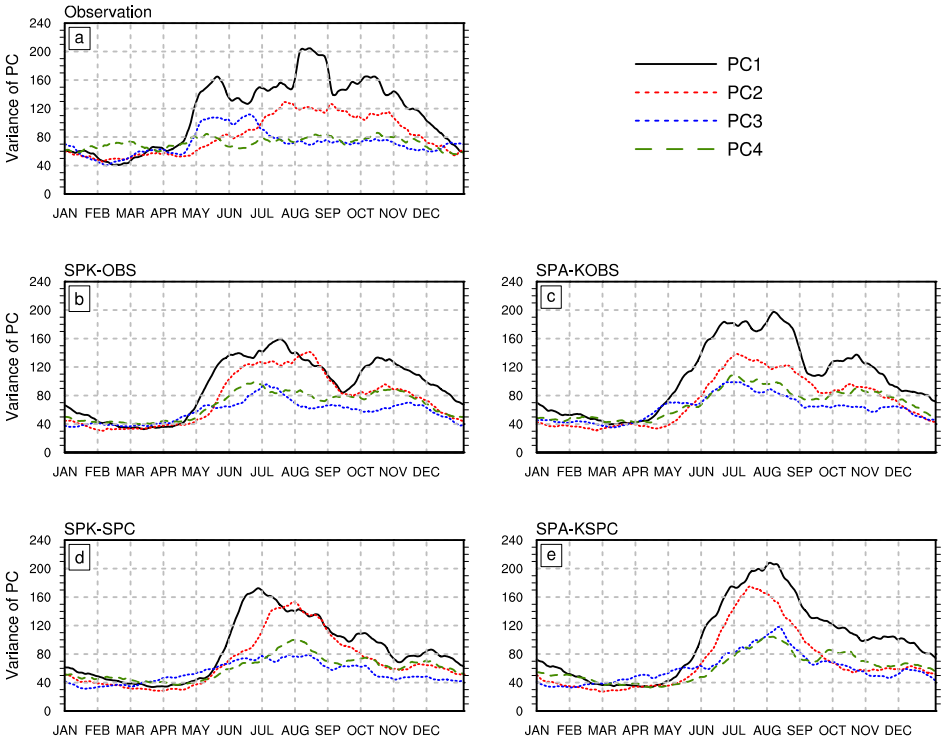

Figure 9: Seasonal cycle of variance of the four leading PCs for (a) NOAA OLR and ERAI u850, (b) SPK-OBS, (c) SPK-SPC, (d) SPA-KOBS, and (e) SPA-KSPC. A 30-day running mean is applied to the seasonal cycle of each variable.

620

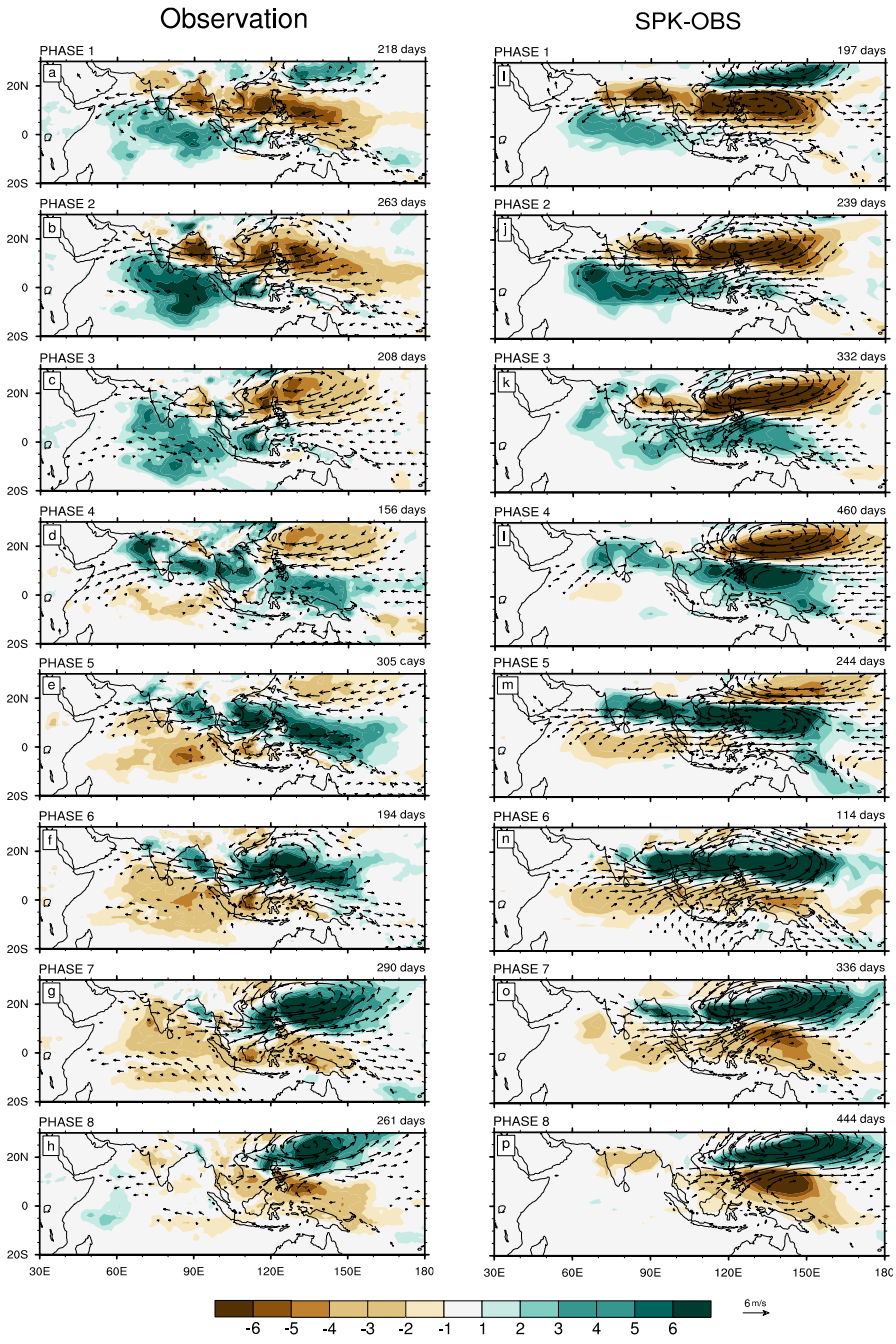

Figure 10: Composites of anomalous precipitation (shading; mm day^{-1}) and 850-hPa wind (vector; with amplitude > 1 m s^{-1}) in the BSISO life cycle from phase 1 to phase 8 for (a–h) GPCP precipitation and ERAI 850-hPa wind and (i–p) SPK-OBS. The number of days for phase composite is shown at the right corner above each panel. Only strong BSISO events (amplitude ≥ 1.5) are selected.

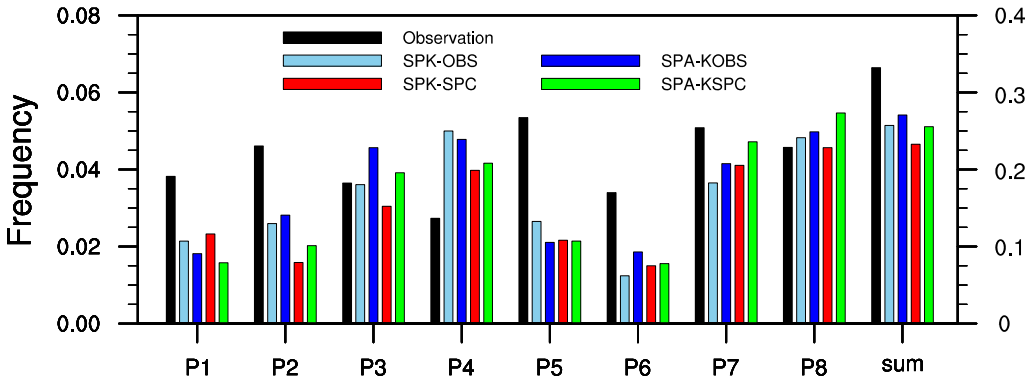

Figure 11: The frequency of strong BSISO activity (amplitude ≥ 1.5) in each phase (P1–P8; the left y-axis) and their sum (the right y-axis) for NOAA OLR and ERAI u850 (black), SPK-OBS (light blue), SPK-SPC (red), SPA-KOBS (dark blue), and SPA-KSPC (green).

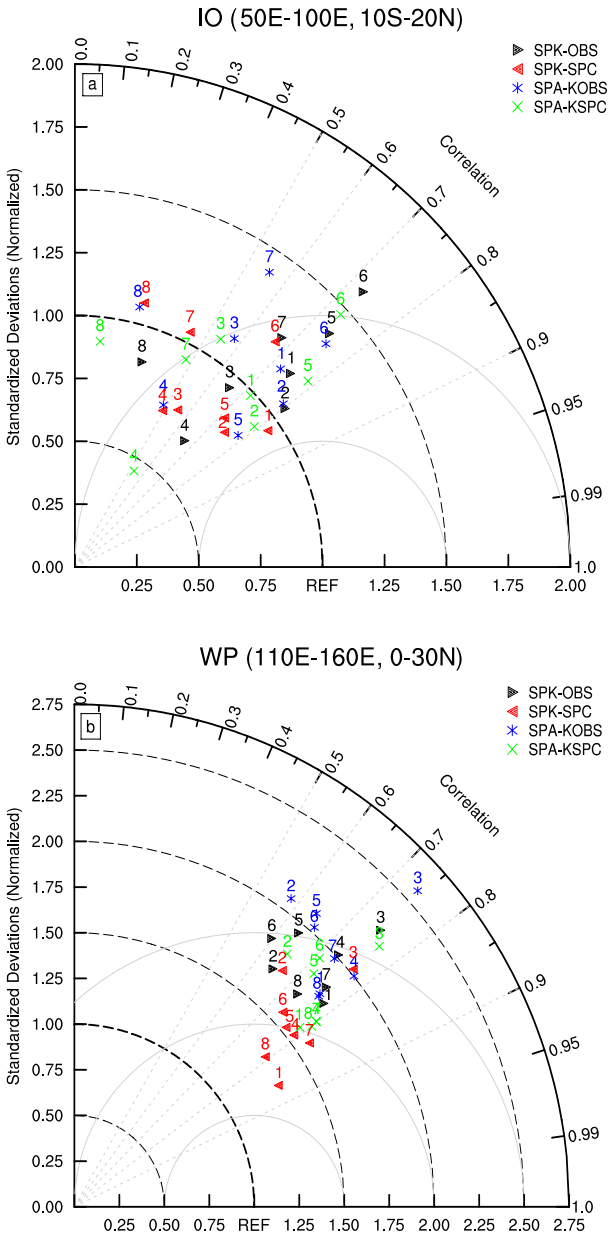

Figure 12: Taylor diagrams for anomalous precipitation in each BSISO phase averaged over (a) the Indian Ocean (IO; 50°–100°E, 10°S–20°N) and (b) western Pacific (WP; 110°–160°E, 0°–30°N). The number above each symbol refers to the BSISO phase.

Boreal summer intraseasonal oscillation in a superparameterized GCM: effects of air-sea coupling and ocean mean state

Yingxia Gao[1,2], Nicholas P. Klingaman[2], Charlotte A. DeMott[3], Pang-Chi Hsu[1]

[1]Key Laboratory of Meteorological Disaster of Ministry of Education/Collaborative Innovation Center on Forecast and Evaluation of Meteorological Disasters/NUIST-UoR International Research Institute, Nanjing University of Information Science & Technology, Nanjing, China
[2]National Centre for Atmospheric Science-Climate and Department of Meteorology, University of Reading, Reading, United Kingdom
[3]Department of Atmospheric Science, Colorado State University, Fort Collins, Colorado, USA

Correspondence to: Pang-Chi Hsu (pangchi@nuist.edu.cn)

Abstract. The effect of air-sea coupling on simulated boreal summer intraseasonal oscillation (BSISO) is examined using atmosphere–ocean-mixed-layer coupled (SPCAM3-KPP) and uncoupled configurations of the superparameterized (SP) Community Atmospheric Model, version 3 (SPCAM3). The coupled configuration is constrained to either observed ocean mean state or the mean state from the SP coupled configuration with a dynamic ocean (SPCCSM3), to understand the effect of mean-state biases on the BSISO. All configurations overestimate summer mean subtropical rainfall and its intraseasonal variance. All configurations simulate realistic BSISO northward propagation over the Indian Ocean and western Pacific, in common with other SP configurations.

Prescribing the 31-day smoothed sea surface temperature (SST) from the SPCAM3-KPP simulation in SPCAM3 worsens the overestimated BSISO variance. In both coupled models, the phase relationship between intraseasonal rainfall and SST is well captured. This suggests that air-sea coupling improves the amplitude of simulated BSISO and contributes to the propagation of convection. Constraining SPCAM3-KPP to the SPCCSM3 mean state also reduces the overestimated BSISO variability, but weakens BSISO propagation. Using the SPCCSM3 mean state also introduces a one-month delay to the BSISO seasonal cycle compared to SPCAM3-KPP with the observed ocean mean state, which matches well with observation. Based on a Taylor diagram, both air-sea coupling and SPCCSM3 mean-state SST biases generally lead to higher simulated BSISO fidelity, largely due to their abilities to suppress the overestimated subtropical BSISO variance.

1 Introduction

The intraseasonal oscillation (ISO) is the most vigorous sub-seasonal signal in the tropics (Zhang, 2005). It interacts with other tropical climate and weather systems, such as the El Niño–Southern Oscillation (ENSO) and tropical cyclones (Kessler et al., 1995; Zhang and Gottschalck, 2002; McPhaden, 2004; Wu et al., 2007), and even the mid-latitude systems (Ding and Wang, 2007; Moon et al., 2013). Compared to the boreal winter ISO (i.e., the Madden and Julian Oscillation, or MJO; Madden and Julian, 1971, 1972), the boreal summer ISO (BSISO) shifts away from the equator to the Asian summer monsoon (ASM)

region (Wang et al., 2006; Lau and Waliser, 2012). Thus, the BSISO is connected strongly to the onset, active and break phases of the ASM (Yasunari, 1979; Annamalai and Slingo, 2001; Lau and Waliser, 2012). The frequency of extreme events over the ASM region is also highly related to BSISO activity (Ren et al., 2013; Li et al., 2015; Hsu et al., 2016, 2017, 2020; Liu and Hsu, 2019).

Realistic representation of the BSISO in climate models remains a challenge, although some improvements have been achieved in recent decades. The state-of-the-art general circulation models (GCMs) still have difficulty in simulating properly the BSISO spatial pattern (Sperber and Annamalai, 2008; Sperber et al., 2013; Hu et al., 2017) and its northwest-southeast tilted rain band structure (Lin et al., 2006; Sabeerali et al., 2013). In contrast, its northward propagation, which is the most significant feature of the BSISO, is captured by most models. Fidelity for northward propagation improved in the models that contributed to the Coupled Model Intercomparison Project (CMIP) phase 5, relative to the CMIP phase 3 (Sabeerali et al., 2013; Sperber et al., 2013). Most models with reasonable northward propagation of the BSISO also simulate a good eastward propagation along the equatorial Indian Ocean.

The representation of convection is largely responsible for the ability of GCMs to simulate BSISO characteristics (Maloney and Hartmann, 2001; Randall et al., 2007; Jiang et al., 2016). Using the Hadley Centre atmospheric GCM (AGCM), Klingaman and Woolnough (2014) found that increasing the convective entrainment and detrainment rates considerably improved deficient MJO-like variability in the Indian and Pacific oceans. In recent years, studies have shown that "superparameterized" (SP) GCMs have high fidelity in simulating ISO variability (Benedict and Randall, 2009; Jiang et al., 2015; Neena et al., 2017). In SP GCMs, the traditional cumulus parameterization is replaced by a two-dimensional (2-D) cloud-resolving model in each grid column to calculate the cloud and radiation physics tendencies (Khairoutdinov and Randall, 2003; Khairoutdinov et al., 2005). By comparing different versions of the National Center for Atmospheric Research (NCAR) Community Atmospheric Model (CAM), DeMott et al. (2014) showed that the SP CAM (SPCAM3) gave better BSISO characteristics than the CAM with the standard convective parameterization.

Besides the convective parameterization scheme, the effect of air~~Incorporating air-sea interaction in CGCMs inevitably introduces atmospheric and oceanic mean-state biases. When studies compare CGCMs to AGCMs prescribed with observed SSTs (Kemball-Cook et al., 2002; Zhang et al., 2006; DeMott et al., 2011; Roxy et al., 2013), the differences between simulations may largely come from mean-state differences, rather than air-sea coupling. Due to the strong control on low-level moisture and convergence anomalies, mean-~-sea interaction on simulated ISO variability has also received growing attention. By comparing the results of coupled GCMs (CGCMs) with the results of the AGCMs prescribed with observed SSTs, many studies found that the inclusion of air-sea coupling could produce a more realistic intraseasonal variability via improving the representation of the diurnal cycle at the air-sea interface (Waliser et al., 1999; Bernie et al., 2005; Danabasoglu et al., 2006; Misra et al., 2008; Stan, 2018). Besides the air-sea coupling process, the differences between simulated results may also come from ocean mean-state differences between AGCM and CGCM, as incorporating air-sea interaction in CGCMs inevitably introduces atmospheric and ocean mean-state biases. Due to the strong control on low-level moisture and convergence anomalies, such ocean mean-state biases may degrade simulated intraseasonal variability (Hendon, 2000; Inness et al., 2003;

Sperber et al., 2005; Bollasina and Ming, 2013). Using the National Centers for Environmental Prediction (NCEP) coupled Climate Forecast System (CFS) model, Seo et al. (2007) showed that BSISO development and propagation were largely improved when the CGCM cold SST bias was removed via flux correction. They suggested that the role of air-sea interaction would be more accurate under an ocean mean state with smaller SST biases. To reduce the mean-state differences between CGCMs and AGCMs, time-varying SSTs from CGCMs should be used to drive AGCMs (Fu and Wang, 2004; Seo et al., 2007; Levine and Turner, 2012; DeMott et al., 2015). However, this quantifies the role of air-sea coupling only under the biased CGCM mean state.

Through flux correction, CGCMs can be constrained to a given climatological ocean state. Such constraint is more effective in CGCMs with simple ocean models, which lack ocean dynamics, as ocean dynamics may interfere with the prescribed flux correction. Simple ocean models also lack coupled modes of variability, such as the ENSO, feedbacks from which can influence the perceived effect of coupling on sub-seasonal variability (Klingaman and DeMott, 2020). The CGCMs with simplified model oceans are a useful tool to investigate the roles of air-sea coupling and mean-state biases in the simulation of BSISO. In this study, we examine the roles of air-sea interaction and mean-state biases in simulated BSISO using a configuration of SPCAM3 coupled to a mixed-layer ocean model, constrained to observed ocean mean state and simulated mean ocean state from the SP Community Climate System Model (CCSM), version 3 (SPCCSM3; Stan et al., 2010). The model experiments, validation data, and analysis methods are described in section 2. In section 3, we analyse the influence of air-sea coupling and mean-state biases on the spatial pattern and propagation of simulated BSISO. Results are discussed and summarized in sections 4 and 5, respectively.

2 Model, experiments and methods

2.1 Models

SPCAM3 (Khairoutdinov et al., 2005) is employed in this study, due to its high fidelity for simulated ISO (Jiang et al., 2015; Neena et al., 2017). It has a horizontal resolution of T42 and a vertical resolution of 30 levels. The embedded 2-D cloud-resolving model has 32 columns with a fine resolution (4 km; Khairoutdinov and Randall, 2003). SPCCSM3 is the coupled configuration, in which SPCAM3 is coupled to the 3-D ocean model of Parallel Ocean Program (POP; Danabasoglu et al., 2006), with active ocean dynamics. SPCCSM3 utilizes the low-resolution version (~3º) of the POP, which has 40 vertical layers with the thickness of top layers being 10 m and exchanges SST and surface fluxes with SPCAM3 at 1-day coupling frequency. To understand the roles of air-sea interaction and SST mean-state biases in BSISO simulation, we couple SPCAM3 with the Multi-Column K Profile Parameterization (MC-KPP) mixed-layer ocean model, referred to as "SPCAM3-KPP" from now. ~~MC-KPP uses the KPP vertical mixing scheme of Large et al. (1994).~~ In the MC-KPP, there is only vertical mixing (Large et al., 1994), while ocean dynamics, such as horizonal or vertical advection or wind-driven upwelling, are absent. Besides, the air-sea coupled modes of variability (such as the ENSO) and potential feedbacks from these modes to intraseasonal variability are also absent. ~~It~~ The MC-KPP consists of many independent 1-D columns, with one column under each AGCM

grid for coupling. Therefore, the horizontal resolution of MC-KPP is the same as that of SPCAM3. The MC-KPP has a fine vertical resolution, with 100 points in a 1000 m water column, 70 of which are in the top 300 m, and ~1-m resolution in the top 20 m. More details on SPCAM3-KPP can be found in Klingaman and DeMott (2020).

Since MC-KPP lacks ocean dynamics, SPCAM3-KPP must be constrained to a reference ocean climatology, which can be taken from an observation-based dataset, an ocean model simulation, or a CGCM simulation. ~~This makes MC-KPP an attractive option for investigating the role of air-sea coupling under different ocean mean states.~~ To represent mean-ocean dynamics and correct for biases in ~~atmospheric~~ surface fluxes, prescribed vertical profiles of heat and salt corrections are applied at each ~~grid point and~~gridpoint at each timestep. ~~These are computed from~~For each SPCAM3-KPP simulation analysed here, a 10-year ~~SPCAM3-KPP~~ "relaxation" simulation is first performed, with a 15-day relaxation timescale toward the reference seasonal cycles of ocean temperature and salinity. The ~~daily climatology of corrections is~~ mean seasonal cycles of the temperature and salinity relaxation tendencies are then computed, smoothed with a 31-day running mean, and imposed ~~on~~as corrections in a "free-running" coupled integration with no relaxation, which displays only small SST biases against the reference climatology (Fig. ~~1). Further~~1). These free-running simulations are analysed here. More details on the correction method can be found in Hirons et al. (2015) and Klingaman and DeMott (2020).

2.2 Experiments and validation data

Two pairs of 50-year-long atmosphere-only (SPCAM3) and coupled (SPCAM3-KPP) models are analysed (Table 1). These simulations were also analysed for studying the MJO in Klingaman and DeMott (2020). For brevity, we write SPCAM3 and SPCAM3-KPP as "SPA" and "SPK", respectively. Next, we explain the setup of each experiment in detail.

To study the effect of mean- -state biases on ~~the~~ simulated BSISO, SPK is constrained to two ocean mean states: 1) the 1980–2009 climatology from the Met Office ocean analysis (Smith and Murphy ~~(~~, 2007) ~~3D ocean analysis; and 2) the climatology from a 20-year simulation of SPCCSM3 ("SPC" for short; Stan et al., 2010; DeMott et al., 2011, 2014). The former is considered as the observed ocean state (Fig. 1c), against which SPC shows large cold SST biases throughout the Indo-Pacific in boreal summer (Fig. 1f). These two coupled simulations are referred to as "SPK-OBS" and "SPK-SPC", respectively. To investigate the effect of air-sea interaction on the simulated BSISO under the observed ocean mean state, SPCAM3 is forced by the 31-day smoothed SST from SPK-OBS (hereafter "SPA-KOBS"). Similarly, we prescribe the 31-day smoothed SST from SPK-SPC to SPCAM3 to understand the air-sea coupling effect under the SPC mean state ("SPA-KSPC"). Table 1 summarises all four experiments.~~

~~All validation data in this study are from the European Centre for Medium-range Weather Forecasts (ECMWF) Interim (ERAI) reanalysis dataset (Dee et al., 2011). The daily variables used include: precipitation, outgoing longwave radiation (OLR), 850 hPa wind, surface variables related to latent heat and sensible heat (LH and SH) fluxes, and 3-D variables associated with moist static energy (MSE; Maloney, 2009). All the variables have the horizontal resolution of 1.5° ×1.5°; we analyse the period of 1986–2016 for compatibility with Gao et al. (2019).~~

; and 2) the climatology from the 20-year SPCCSM3 ("SPC" for short) simulation, which was analysed in Stan et al. (2010) and DeMott et al. (2014). The former is considered as the observed ocean state (Fig. 1c), against which SPC shows large cold SST biases throughout the Indo-Pacific in the boreal summer (Fig. 1f). These two coupled simulations are referred to as "SPK-OBS" and "SPK-SPC", respectively. Differences between the results of SPK-OBS and those of SPK-SPC can reveal the effect of SPC mean-state SST biases on the simulated BSISO. To investigate the effect of air-sea interaction on simulated BSISO under the observed ocean mean state, the time-varying SSTs from SPK-OBS are prescribed in an SPA simulation ("SPA-KOBS"). The 31-day smoothed SST is used to remove the high-frequency variability of SST and avoid erroneous positive feedbacks between SSTs, surface fluxes and precipitation (see DeMott et al., 2015 and references therein). Similarly, we prescribe the 31-day smoothed SST from SPK-SPC to SPA to understand the air-sea coupling effect under the SPC mean state ("SPA-KSPC") through the comparison with SPK-SPC. Table 1 summarises all four experiments.

The validation data used in this study include: 1) daily outgoing longwave radiation (OLR) from the National Oceanic and Atmospheric Administration (NOAA) at a resolution of 2.5º×2.5º for 1986–2016 (Liebmann and Smith, 1996); 2) daily precipitation from the Global Precipitation Climatology Project (GPCP; Huffman et al., 2001) at a resolution of 1º×1º for 1997–2016; and 3) daily variables from the European Centre for Medium-range Weather Forecasts (ECMWF) Interim (ERAI) reanalysis dataset at a resolution of 1.5º×1.5º (Dee et al., 2011). The variables from the ERAI include: 850-hPa wind, SST, surface variables related to latent heat and sensible heat (LH and SH) fluxes, and 3-D variables associated with moist static energy (MSE; Maloney, 2009). Note that ERAI SST was the boundary condition prescribed for the ERAI. We analyse the period of 1986–2016 of ERAI data for compatibility with Gao et al. (2019).

2.3 Methods

The BSISO convective intensity is represented by 20–100-day-filtered variability of boreal summer (May–October) precipitation, OLR or MSE, depending on the process-oriented diagnostic applied. To reveal the overall propagation features of BSISO convection, lead-lag regression analysis is performed on area-averaged, filtered precipitation or OLR. Here, we use precipitation. Since the Indian and Pacific basins exhibit different basic states (Lau and Waliser, 2012), we compute propagation over one region in each basin: the eastern Indian Ocean (80°–90°E, 0°–10°N) and western Pacific (130°–140°E, 0°–10°N).

DeMott et al. (2016) and Gao et al. (2019) provided a useful diagnostic method to quantitatively assess the contribution of intraseasonal SST variability to the MSE budget of ISO in the boreal winter and boreal summer, respectively. The temporal and spatial evolution of column-integrated MSE ($\langle m \rangle$) is highly consistent with that of anomalous precipitation; and positive values of the time change of $\langle m \rangle$ ($\partial \langle m \rangle / \partial t$) leads 90º ahead of the convection. Thus, the physical processes that modulate $\langle m \rangle$ and $\partial \langle m \rangle / \partial t$ can be considered as the mechanisms responsible for the maintenance and propagation of convections, respectively. We employ the same approach to understand oceanic feedbacks to the simulated BSISO, and compare these feedbacks to those in reanalysis data. Intraseasonal SST can affect atmospheric convection through modifying LH and SH fluxes and hence MSE, via the near-surface gradients in specific humidity and temperature. Based on decomposition of surface

bulk formulae (Weare et al., 1981), SST modulation of surface fluxes is represented as the difference between fluxes calculated using the full and 61-day smoothed SST. These SST-modulated fluxes are then projected onto $\langle m \rangle$ and $\partial\langle m \rangle / \partial t$ to reveal the oceanic feedbacks to the maintenance and propagation of BSISO convection, respectively. More details can be found in DeMott et al. (2016) and Gao et al. (2019).

We employ the BSISO indices of Lee et al. (2013) to investigate the simulated convective features in each BSISO phase. First, daily anomalies are computed as the departure from the climatological annual cycle and a 120-day running mean. Multi-variate Empirical Orthogonal Function (MV-EOF) is then performed on the combination of OLR and 850-hPa zonal wind (u850) anomalies, each normalized by their respective area-mean standard deviation over the ASM region (40°–160°E, 10°S–40°N) during the boreal summer. The first two leading principal components (PC1 and PC2) define the BSISO indices, which separate the BSISO life cycle into eight phases. For model results, normalized OLR and u850 anomalies are projected onto the observed EOF modes to obtain the model PCs. This approach helps assess fairly how well the model experiments simulate the observed BSISO because the projected results (model PCs) can be directly compared to observations (Sperber et al., 2008, 2013; DeMott et al., 2019). Model simulated BSISO phase composites are constructed based on these PCs ~~(Sperber et al. 2013).~~ Consistent with Lee et al. (2013), only strong BSISO events ($\sqrt{PC1^2 + PC2^2} > 1.5$) are selected for phase composites.

3 Results

3.1 Mean state and intraseasonal variability

Previous studies indicated that ISO variability is closely related to the climatological state of convection (Wheeler and Kiladis, 1999; Sperber et al., 2000; Waliser et al., 2003). Thus, we first examine the summer mean precipitation and 850-hPa wind (Fig. 2). In ~~ERAI~~GPCP, substantial rainfall appears over the ASM region (Fig. 2a). In common with SPCAM3 simulation (DeMott et al., 2011), SPK-OBS overestimates subtropical rainfall (10°–20°N), particularly in the western North Pacific (Figs. 2b and e), but underestimates rainfall over the southern Indian Ocean, Maritime Continent and India north to 20°N. These precipitation biases are associated with low-level wind biases. Simulated mean westerlies extend into the western North Pacific, increasing convergence across the band of subtropical enhanced precipitation. In SPK-SPC (Fig. 2c), which is constrained to the cold climatological SPC SST (Fig. 1d), rainfall is reduced compared to that in SPK-OBS: wet biases are reduced while dry biases become more severe ~~(Figs.~~ over the Indian Ocean and western North Pacific (Figs. 2e and f). The SPC mean-state SST bias tends to suppress the mean precipitation. Mean precipitation fields in SPA-KOBS and that in SPK-OBS (SPA-KSPC and SPK-SPC) are nearly the same (not shown).

Figure 3 illustrates the standard deviations of intraseasonal SST and precipitation variability. SST variability is underestimated over the Indian Ocean and equatorial Pacific in all simulations. In the off-equatorial Pacific, we see more intraseasonal SST variability in SPK-OBS but less SST variability in SPK-SPC (Figs. 3b and c~~).~~), which may be related to the less SST variability in SPC as a consequence of coarse horizontal resolution of POP. Prescribing the 31-day smoothed SST

from SPK-OBS (SPK-SPC) to SPA-KOBS (SPA-KSPC~~),~~) strongly reduces intraseasonal SST, as expected (Figs. 3d and e). The right-column panels in Fig. 3 show the intraseasonal rainfall from each dataset (Figs. 3f–j). Compared to ~~ERAI~~GPCP (Fig. 3f), all simulations significantly overestimate subtropical intraseasonal precipitation variability (10°–20°N), where mean rainfall is also overestimated (Fig. 2). This reinforces that model BSISO biases are largely associated with incorrect representation of mean rainfall (Sperber and Annamalai, 2008; Sabeerali et al., 2013; Hu et al., 2017). The overestimate of intraseasonal rainfall in SPK-SPC (Fig. 3h) is smaller than that in SPK-OBS (Fig. 3g), consistent with the lower mean rainfall in SPK-SPC. SPA-KOBS (Fig. 3i) and SPA-KSPC (Fig. 3j) show increases in intraseasonal rainfall relative to SPK-OBS and SPK-SPC, respectively. This indicates that both cold SST biases and air-sea coupling exert negative feedbacks on BSISO convection, and improve the simulated BSISO amplitude.

3.2 Northward propagation of BSISO

Lag regression analysis is employed to understand the simulated BSISO propagation in each experiment. Over the Indian Ocean, area (80°–90°E) averaged intraseasonal precipitation ~~is~~and SST are regressed onto area (80°–90°E, 0°–10°N) averaged intraseasonal precipitation time series (Fig. 4). In ~~ERAI~~observation, the convective anomaly originates south of the equator and propagates southward to 10º–15ºS and northward into the Bay of Bengal (Fig. 4a). All simulations capture the northward propagation, confirming the high fidelity of SPCAM3 in simulating BSISO northward propagation (DeMott et al., 2014; Neena et al., 2017). However, the simulations fail to capture the southward propagation branch. ~~And~~Other significant biases can be seen in the locations of maximum convections of BSISO. The simulated ~~strongest convection~~convective center shifts northward (10°N) relative to ~~ERAI~~observation (5°N). A weaker propagating signal is observed under the SPC mean state than under the observed mean state for both SPK and SPA, especially over the subtropical regions from Lag 0 to Lag 20 (~~marked with black box;~~ Figs. 4b and d; Figs. 4c and e). This is consistent with weaker BSISO variability under the SPC mean state (Figs. 3g–j), suggesting that cold tropical mean SST biases are unfavourable for BSISO variability and northward propagation. In SPA, the amplitude of convective maxima increases relative to that in SPK, but with weaker propagation (Figs. 4b–e). Air-sea coupling plays a similar role in BSISO convection under both observed and cold mean states: it damps BSISO amplitude but supports northward propagation over the eastern Indian Ocean.

The BSISO northward propagation over the western Pacific is shown in Fig. 5. ~~In ERAI, the~~The observed convection also originates south of the equator, but propagates only north, into the western North Pacific (Fig. 5a). These characteristics are properly simulated by all experiments (Figs. 5b–e). As in the Indian Ocean, due to the large overestimate of subtropical BSISO variability, the strongest simulated convection moves north compared to ~~ERAI~~observation. It is notable that considerable suppressed off-equatorial convection leads the strongest convection by ~1 week, which degrades model performance. Over the western Pacific, mean-state biases also reduce the northward propagating signal in SPK-SPC (SPA-KSPC) relative to that in SPK-OBS (SPA-KOBS). Air-sea interaction seems to play little role in the BSISO northward propagation over the western Pacific, as there is no substantial difference between SPK and SPA under either ocean mean state (Figs. 5b–c; Figs. 5d–e).

3.3 Quantitative contribution of SST fluctuation to BSISO

The temporal and spatial evolutions of BSISO and SST variability over the Indian Ocean and western Pacific are shown in Figs. 6 and 7, respectively. Over the Indian Ocean, ~~in ERAI,~~the warm SSTs in observation always lead enhanced convection, with maxima north/northeast of the convective center (Figs. 6a, f and k). The SST-rainfall phase relationship is properly represented in SPK ~~and~~but misrepresented in SPA. However, ~~in more detail,~~ SPK shows a shorter delay between off-equatorial suppressed convection and warm SST relative to ~~ERAI.~~observation, which can be more clearly revealed in Fig. 4. This suggests the ocean responds more quickly to BSISO convection in SPK than in ~~ERAI~~observation, which might be caused by the lack of ocean dynamics in MC-KPP. Alternatively, the high coupling frequency (15 minutes) and fine ocean vertical resolution (~1 m) in SPK may make the mixed-layer depth too sensitive to atmospheric convection. The SST anomalies in SPA are small due to the 31-day smoothing applied (Figs. 6d, e, i, j, n, and o). The size of the convective regions in all model simulations is smaller than that in observations, which may imply a deficient BSISO propagation. Compared to SPK-OBS, the convective region ~~becomes smaller under~~reduces when either the SPC mean state is used (SPK-SPC) or ~~without~~ air-sea coupling ~~(SPK-SPC,~~ is removed (SPA-KOBS and SPA-KSPC). To some degree, it reflects the negative (positive) role of mean ~~–~~ state biases (air-sea interaction) in supporting the propagating BSISO signal, in agreement with Fig. 4.

Over the western Pacific, SPK ~~simulates well~~reproduces the ~~ERAI~~observed phase relationship between the convection and SST anomalies: a near-quadrature relationship over the equatorial regions (Figs. 7a–c), but ~~nearly out~~ a shift of ~~phase over~~ warm SST anomalies toward the suppressed convective regions in the off-equatorial regions (Figs. 7f–h and k–m). This phase relationship can also be clearly revealed in the Hovmöller diagram (Fig. 5). However, SPK produces substantial suppressed convection north of the active convection over the western North Pacific, consistent with Fig. 5. Besides, simulated warm SST appears north of the convective center, while the ERAI SST maximum is always located northwest of the convective center. This implies that the simulated SST may be favourable for the northward but unfavourable for the westward propagation of the simulated BSISO convection over the western Pacific. Imposing the SPC mean state weakens the simulated convection. In SPA, the intraseasonal SST is very small by design.

As revealed by Gao et al. (2019), intraseasonal SST can affect the BSISO by modulating surface LH and SH fluxes. The temporal and spatial distributions of SST-modulated fluxes are highly coherent with those of SST anomalies themselves. Therefore, the evolutions of SST anomalies shown in Figs. 6 and 7 can also roughly reveal the evolutions of SST-modulated surface fluxes. By regressing the SST-modulated flux anomalies onto the BSISO $\langle m \rangle$ and $\partial\langle m \rangle / \partial t$, Fig. 8 illustrates the "SST effect" on the maintenance and propagation of convection. In the ERAI, intraseasonal SST supports $\langle m \rangle$ in the central Indian Ocean and Bay of Bengal but destroys $\langle m \rangle$ in the western North Pacific (Fig. 8a). The inter-basin differences are linked to the differences in SST-convection phase relationship (Gao et al., 2019). However, simulated SST anomalies in SPK largely damp the convection over the Bay of Bengal and western North Pacific (Figs. 8b and c), because of the quicker response of the SPK ocean to BSISO convection, combined with the erroneously strong suppressed convection just before the active phase. The negative SST effect on $\langle m \rangle$ agrees with the stronger subtropical BSISO variability in SPA than in SPK. For the BSISO

propagation, the simulated SST anomalies play positive roles in $\partial\langle m\rangle/\partial t$ under both ocean mean states (Figs. 8g and h), but with a smaller contribution (8–12%) than that in the ERAI (12–20%). A weak SST effect on the BSISO can still be found in SPA (Figs. 8d, e, i, and j), as these simulations retain some intraseasonal SST variability (Fig. 3). In summary, SST variability enhances the simulated amplitude of BSISO variability by suppressing the excessive subtropical convection and contributes to the propagation of convection over the entire BSISO region.

3.4 BSISO indices

Propagating BSISO characteristics can also be examined using the BSISO indices. Figure 9 shows the annual cycle of variance of each of the first four PCs from ~~ERAI~~observation and model simulations. Since EOF analysis is only applied to May–October data, the PC time series for November–April are obtained by projecting OLR and u850 anomalies onto the same EOF patterns.

In ~~ERAI, PCs have a similar seasonal cycle as those from Lee et al. (2013).~~observation, PC1 has the largest variance throughout the boreal summer (Fig. 9a). It increases sharply from late April, maximises in August, and is followed by PC2 with about half a month delay. In contrast to PC1 and PC2, PC3 exhibits most of its variance in early summer (May–June). PC4 also has a broad peak, but its amplitude is much smaller than those of the other PCs. SPK-OBS produces a similar seasonal cycle of PC1 as ~~ERAI~~observation, except for deficient variance in August–September, which largely reduces the amplitude difference between the first two PCs (Fig. 9b). Simulated PC1 in SPK-OBS also increases abruptly from late April, with a half-month delay between PC1 and PC2, which matches ~~ERAI~~observation well. However, PC1 in SPK-SPC begins to increase in late May (Fig. 9c), about one month later than ~~ERAI~~observation and SPK-OBS. The variance of the first two PCs in SPK-SPC has a much narrower peak and tails off from early July, without a second peak in October. This suggests that cold SST bias leads to a late onset of BSISO activity, and also strongly degrades the annual cycle of BSISO activity. In both SPK simulations, the amplitude of PC3 is smaller than that of PC4, indicating that the order of those simulated PCs is reversed. All model simulations show a similarly poor ability to simulate PC3 and PC4. Therefore, hereafter we only focus on PC1 and PC2. Removing air-sea coupling in SPA increases significantly the strength of PC1 relative to that in SPK (Figs. 9b and d; Figs. 9c and e). This suggests that the role of air-sea coupling in suppressing BSISO variability is mainly expressed through damping variability in PC1.

Based on the PC1 and PC2 time series, the BSISO life cycle is separated into eight phases, which represents the canonical northward propagating BSISO (Annamalai and Sperber, 2005; Wang et al., 2005). Figure 10 shows the phase composites of anomalous precipitation and 850-hPa wind from ~~ERAI~~observation and SPK-OBS. SPK-OBS displays a similar evolution of the structure of convection and circulation as ~~in ERAI~~the observation, but they have significant amplitude differences. The simulated precipitation variability is underestimated over the equatorial Indian Ocean, while substantial overestimate appears over the off-equatorial regions. The simulated circulation ~~also~~ matches well with the simulated convection: easterlies (westerlies) occur to the north (south) of the ascent; cyclonic (anticyclonic) circulations coincide with the active (suppressed) off-equatorial convection. However, the northwest-southeast titled rainfall band in SPK-OBS is more zonal than that in ~~ERAI (Fig~~GPCP (Figs. 10e and m), largely due to the poor representation of BSISO variability over the western Pacific. In

~~ERAI~~observation, most strong BSISO events occur in phases 2, 5, 7, and ~~7~~8. In contrast, in SPK-OBS, a stronger preference for simulated strong BSISO events appear in off-equatorial regions (phases 3, 4, 7, and 8) rather than in near-equatorial regions (phases 1, 2, 5, and 6). It implies that the BSISO variability is largely determined by the propagating BSISO signal (Sperber et al., 2013; Neena et al., 2017).

We further compute the frequency of strong BSISO events in each phase from each dataset (Fig. 11). Overall, there are fewer strong BSISO events in the simulations (~~25–30~~22.5–27.5%) than in ~~ERAI~~observation (~33%), although the amplitude of simulated precipitation associated with these events is much larger. The frequency of stronger BSISO events becomes further fewer under the SPC ocean mean state than that under the observed ocean mean state. Consistent with Fig. 10, ~~in ERAI,~~ phases 2, 5, 7, and ~~7~~8 show the highest frequencies in observation, while in SPK-OBS and SPK-SPC, most strong simulated BSISO events occur in phases 3, 4, 7, and 8. ~~Comparing SPK-SPC and SPK-OBS shows that the SPC ocean mean state has little consistent effect on the frequency of BSISO events.~~ Removing air-sea coupling in SPA further increases the frequency of strong BSISO events in the off-equatorial regions ~~(phases 3, 4, 7, and 8),~~ associated with the greater intraseasonal convective variability in SPA relative to that in SPK.

To quantitatively evaluate the performance of each simulation, we construct Taylor diagrams over the Indian Ocean (50°–100°E, 10°S–20°N) and western Pacific (110°–160°E, 0°–30°N), respectively (Fig. 12). These diagrams provide pattern correlation coefficients and root-mean-square-errors of simulated intraseasonal precipitation against ~~ERAI~~GPCP intraseasonal precipitation in each BSISO phase. Over the Indian Ocean, the fidelity of each simulation varies from phase to phase (Fig. 12a). Generally, higher pattern correlations appear in equatorial phases (phases 1, 2, 5 and 6) than in off-equatorial phases (phases 3, 4, 7 and 8). ~~The area-averaged rainfall variability is overestimated in almost all phases, with largest amplitude biases in phases 3 and 6 (1.5–2.25 of the standard deviation of ERAI). Overall, SPK-SPC outperforms SPK-OBS, largely due to its smaller amplitude biases compared to ERAI.~~ Under the observed ocean mean state, air-sea coupling improves the simulation fidelity in most phases ~~1, 3, 7,~~, while the SPC ocean mean state and ~~8. Under~~coupling under the SPC ocean mean state~~, coupling greatly improves~~ have little consistent effect on the simulated BSISO ~~life cycle over the Indian Ocean, except for phase 2~~fidelity.

In almost all simulations, higher pattern correlations are found over the western Pacific (0.~~7~~6–0.9) than over the Indian Ocean (0.5–0.~~9~~8), but with much larger overestimates of amplitude (Fig. 12b). The overall simulation performance over the western Pacific is ranked as follows: SPK-SPC, SPA-KSPC, SPK-OBS, and SPA-KOBS. Simulations with the SPC ocean mean state perform better than those with the observed ocean mean state, in terms of both amplitude and distribution. Since the excessive subtropical rainfall variability is the biggest error in SPCAM3, the underlying cold SSTs largely weaken the convection, which helps reduce the amplitude biases and improve the pattern correlation with ~~ERAI~~observation. Air-sea coupling improves model performance under both ocean mean states, particularly in terms of suppressing the overestimated BSISO variability over the western North Pacific.

4 Discussion

Despite the ~~large~~ correct SST-rainfall phase relationship in SPK simulations, a shorter delay between suppressed convection and warm SST occurs compared to the reanalysis. This may be associated with the configuration of the MC-KPP ocean (lack of full ocean dynamics, high coupling frequency and fine vertical resolution). As a consequence of the shorter delay, it is easy to surmise the negative effect of air-sea coupling on the amplitude of convection, while its effect on the propagation is not obvious. Overall, intraseasonal SST anomalies in SPK largely damp intraseasonal subtropical convection variability and make a smaller contribution (8–12%) to $\partial\langle \mathrm{m} \rangle / \partial \mathrm{t}$ than those in the ERAI (12–20%). Comparing Figs. 4 and 5, we can see propagation is slightly enhanced in SPK relative to SPA over the Indian Ocean; however, coupling makes nearly no difference to the propagating signal over the western Pacific. This may be related to the larger underestimate of the contribution of intraseasonal SST to $\partial\langle \mathrm{m} \rangle / \partial \mathrm{t}$ over the western Pacific than over the Bay of Bengal (Fig. 8). More importantly, it implies that atmospheric internal processes are essential to the propagation of convection, since SPCAM3 simulates BSISO propagation well even without coupling or sub-seasonal SST variability.

Stan et al. (2010) and Neena et al. (2017) reported that SPC showed better ISO simulation skill than SPA with prescribed observed SST. In our experiments, the BSISO variability is similar in SPK-OBS and SPA-KOBS and in SPK-SPC and SPA-KSPC, which suggests a limited role for air-sea coupling in the simulated BSISO. Comparing SPK-OBS and SPK-SPC strongly suggests that the ocean mean-state biases in SPC improve BSISO amplitude and spatial distribution. This implies that mean-state biases in SPC, not sub-seasonal air-sea coupled feedbacks, be the primary reason for the improved BSISO in SPC relative to SPA. While the SPC mean state improves the amplitude and spatial pattern of simulated BSISO convection, it also weakens northward propagation. ~~By examining Figs. 1g–h, these amplitude/spatial pattern and propagating differences between SPK-SPC and SPK-OBS may be related to the stronger horizontal SST gradients in SPK-SPC, since the pattern of mean state column water vapor biases closely follows that of mean SST biases (DeMott et al., 2019). Stronger meridional SST gradients in SPC may largely suppress the overestimated subtropical rainfall than in SPK-OBS. SPC also seems to reduce the zonal SST (moisture) gradient that plays an essential role in $\partial\langle \mathrm{m} \rangle / \partial \mathrm{t}$ for both the boreal winter and boreal summer ISO, leading to less propagating BSISO signal (Jiang, 2017; Jiang et al., 2018; Gao et al., 2019). Thus, as suggested by Seo et al. (2007) and Klingaman and Woolnough (2014), it is important to control for the effect of mean state biases as well as its gradients when evaluating the influence of air-sea coupling on the simulated ISO (DeMott et al., 2019).~~Besides the SST mean-state biases, it is also important to control the SST gradient bias. Several studies highlighted the importance of horizonal advection of mean moisture (or $\langle m \rangle$) by anomalous wind in the propagation of the ISO (Hsu and Li, 2012; Jiang, 2017; Jiang et al., 2018; DeMott et al., 2019; Gao et al., 2019). Our additional diagnosis revealed that the pattern of $\langle m \rangle$ biases closely follows that of SST biases (not shown). By examining Figs. 1g–h, we would argue that the stronger BSISO variability in SPK-OBS than in SPK-SPC may be related to the enhanced meridional gradients of SST and moisture. Weaker propagating BSISO signal in SPC seems to be associated with the reduced horizontal $\langle m \rangle$ advection of mean $\langle m \rangle$ induced by anomalous wind.

In CGCMs with dynamic oceans, it is also important to consider the effect of interannual SST variability (such as the ENSO), due to its strong control on sub-seasonal variability, particularly on the boreal winter MJO (Weaver et al., 2011; Kapur and Zhang, 2012; Klingaman and DeMott, 2020). We note that none of the simulations considered here represent the ENSO or other coupled modes of interannual variability, as the MC-KPP ocean model lacks the requisite ocean dynamics. Using the same simulations, Klingaman and DeMott (2020) found that the intensity and propagation of the boreal winter MJO was strongly suppressed in SPCAM3-KPP under the SPC ocean mean state, while here the SPC ocean mean state enhances BSISO amplitude and only slightly weakens its propagation. Klingaman and DeMott (2020) found that the inclusion of the SPC ENSO variability on top of the SPC mean state substantially strengthened the MJO, suggesting that the strong MJO in SPC arose from an excessively intense response to the ENSO. The effect of ENSO is not considered here, which could be a subject for further study.

5 Summary

We investigate the roles of ocean mean-state biases and air-sea coupling in simulating the BSISO by coupling the SPCAM3 to the MC-KPP mixed-layer ocean. To diagnose the sensitivity to the ocean mean state, SPCAM3-KPP is constrained to either observed ocean mean state or the ocean mean state from the coupled configuration of SPCAM3 with a dynamic ocean (SPC). The SPC mean state introduces substantial cold SST biases across the Indo-Pacific. To diagnose the sensitivity to air-sea coupling under different mean states, SPCAM3 is driven by the 31-day running mean SST from each SPCAM3-KPP simulation.

Systematic errors in SPCAM3 result in overestimated subtropical summer mean rainfall and intraseasonal variability. These overestimated variables are greatly improved with coupling, or with the SPC ocean mean state. Lag regression composites show that the simulated convection exhibits realistic northward propagation over both the Indian Ocean and western Pacific. However, the strongest convective center shifts north relative to the observation. Using the SPC ocean mean state degrades the propagating BSISO signal in both coupled and uncoupled simulations, relative to the simulations that use the observed ocean mean state. Air-sea coupling slightly enhances the strength of the propagating signal under both ocean mean states. The coupled simulations capture the SST-rainfall phase relationship reasonably well, but with warm SSTs shifting toward the suppressed convection over the Bay of Bengal relative to the observation. Intraseasonal SST variability plays a similar role in the BSISO MSE budget in the coupled simulations, regardless of the ocean mean state: it damps subtropical convection and favours BSISO northward propagation, but with a smaller contribution (8–12%) than the reanalysis (12–20%).

We also examine the simulation skill of propagating BSISO characteristics by using BSISO indices. Experiments with the observed ocean mean state produce a realistic annual cycle of BSISO variance, while the simulations with the SPC mean state result in a one-month delay of the onset of BSISO activity. Air-sea coupling weakens convective variability mainly through suppressing the first EOF mode. Different from the ~~reanalysis~~observation, all model simulations favour strong BSISO activity in off-equatorial regions, which is associated with intense subtropical variability. Overall, the simulations using the SPC ocean

mean state produce an improved BSISO than those using the observed ocean mean state, in terms of both amplitude and pattern correlation of anomalous precipitation. Air-sea coupling improves the BSISO fidelity in most phases. The enhancement of simulated BSISO by the ocean mean state and air-sea coupling largely arises from suppressing erroneously strong subtropical convection.

In our study, air-sea coupling has a similar effect on the simulated BSISO under different ocean background states, suggesting that the role of coupling may largely depend on the phase relationship between the convection and SST anomalies. Compared to daily coupling frequency between the atmosphere and ocean components of CGCMs, improved fidelity for the BSISO simulation is shown in CGCMs with sub-daily coupling frequency (Woolnough et al., 2007; Klingaman et al., 2011; Hu et al., 2015). In our study, the model ocean tends to respond quickly to the atmospheric convection, which may be associated with the sensitive mixed layer depth due to the absent ocean dynamics in KPP. Therefore, to better understand the role of coupling in the simulated ISO, efforts should be aimed at simulating a realistic phase relationship between the ISO convection and SST anomalies.

Code and data availability. All model outputs are available on the U.K. JASMIN collaborative research analysis facility (http://www.jasmin.ac.uk). Access to data can be obtained by contacting Nicholas Klingaman (nicholas.klingaman@ncas.ac.uk). Data used to reproduce the figures and associated code can be found at https://doi.org/10.6084/m9.figshare.c.4874406.v2

Competing interests: The authors have no competing interests to declare.

Author contributions. YG and PCH developed the codes, conducted analyses, and wrote the manuscript. NPK and CAD designed and performed SPCAM3-KPP simulations presented in the paper. All authors gave comments and contributed to the development of the manuscript.

Competing interests. The authors declare that they have no conflict of interest.

Acknowledgements. YG and PCH are supported by the National Key R&D Program of China (2018YFC1505804) and NUIST-UoR Open Project. NPK is supported by an Independent Research Fellowship from the UK Natural Environment Research Council (NE/L010976/1) and a grant from the NOAA Modeling, Analysis, Predictions and Projections program (NA16OAR4310071). CAD is supported by the National Science Foundation (NSF 1445191) and the NOAA Modeling, Analysis, Predictions and Projections program (NA16OAR4310094). ERAI reanalysis data are obtained from http://apps.ecmwf.int/datasets.

References

Annamalai, H. and Slingo, J. M.: Active / break cycles: Diagnosis of the intraseasonal variability of the Asian summer monsoon, Clim. Dyn., 18(1–2), 85–102, https://doi.org/10.1007/s003820100161, 2001.

Annamalai, H. and Sperber, K. R.: Regional heat sources and the active and break phases of boreal summer intraseasonal (30–50 day) variability, J. Atmos. Sci., 62(8), 2726–2748, https://doi.org/10.1175/JAS3504.1, 2005.

Benedict, J. J. and Randall, D. A.: Structure of the Madden–Julian oscillation in the superparameterized CAM, J. Atmos. Sci., 66(11), 3277–3296, https://doi.org/10.1175/2009JAS3030.1, 2009.

Bernie, D. J., Woolnough, S. J., Slingo, J. M. and Guilyardi, E.: Modeling diurnal and intraseasonal variability of the ocean mixed layer, J. Climate, 18(8), 1190–1202, https://doi.org/10.1175/JCLI3319.1, 2005.

Bollasina, M. A. and Ming, Y.: The general circulation model precipitation bias over the southwestern equatorial Indian Ocean and its implications for simulating the South Asian monsoon, Clim. Dyn., 40(3–4), 823–838, https://doi.org/10.1007/s00382-012-1347-7, 2013.

Danabasoglu, G., Large, W. G., Tribbia, J. J., Gent, P. R., Briegleb, B. P., and McWilliams, J. C.: Diurnal coupling in the tropical oceans of CCSM3, J. Climate, 19(11), 2347–2365, 2006.

Dee, D. P., Uppala, S. M., Simmons, A. J., Berrisford, P., Poli, P., Kobayashi, S., Andrae, U., Balmaseda, M. A., Balsamo, G., Bauer, P., Bechtold, P., Beljaars, A. C. M., van de Berg, L., Bidlot, J., Bormann, N., Delsol, C., Dragani, R., Fuentes, M., Geer, A. J., Haimberger, L., Healy, S. B., Hersbach, H., Hólm, E. V., Isaksen, L., Kållberg, P., Köhler, M., Matricardi, M., McNally, A. P., Monge-Sanz, B. M., Morcrette, J.-J., Park, B.-K., Peubey, C., de Rosnay, P., Tavolato, C., Thépaut, J.-N. and Vitart, F.: The ERA-Interim reanalysis: Configuration and performance of the data assimilation system, Q. J. Roy. Meteorol. Soc. 137(656), 553–597, https://doi.org/10.1002/qj.828, 2011.

DeMott, C. A., Stan, C., Randall, D. A., Kinter, J. L. and Khairoutdinov, M.: The Asian monsoon in the superparameterized CCSM and Its relationship to tropical wave activity, J. Climate, 24(19), 5134–5156, https://doi.org/10.1175/2011JCLI4202.1, 2011.

DeMott, C. A., Stan, C., Randall, D. A. and Branson, M. D.: Intraseasonal variability in coupled GCMs: The roles of ocean feedbacks and model physics, J. Climate, 27(13), 4970–4995, https://doi.org/10.1175/JCLI-D-13-00760.1, 2014.

DeMott, C. A., Klingaman, N. P., Tseng, W.-L., Burt, M. A., Gao, Y., and Randall, D. A.: The convection connection: How ocean feedbacks affect tropical mean moisture and MJO propagation, J. Geophys. Res. Atmos., 124(22), 11910–11931, https://doi.org/10.1029/2019JD31015, 2019.

DeMott, C. A., Klingaman, N. P. and Woolnough, S. J.: Atmosphere-ocean coupled processes in the Madden-Julian oscillation, Rev. Geophys., 53(4), 1099–1154, https://doi.org/10.1002/2014RG000478, 2015.

DeMott, C. A., Benedict, J. J., Klingaman, N. P., Woolnough, S. J. and Randall, D. A.: Diagnosing ocean feedbacks to the MJO: SST-modulated surface fluxes and the moist static energy budget, J. Geophys. Res. Atmos., 121(14), 8350–8373, https://doi.org/10.1002/2016JD025098, 2016.

Ding, Q. and Wang, B.: Intraseasonal teleconnection between the summer Eurasian wave train and the Indian monsoon, J. Climate, 20(15), 3751–3767, https://doi.org/10.1175/JCLI4221.1, 2007.

Fu, X. and Wang, B.: Differences of boreal summer intraseasonal oscillations simulated in an atmosphere–ocean coupled model and an atmosphere-only model, J. Climate, 17, 1263–1271, 2004.

Gao, Y., Klingaman, N. P., DeMott, C. A. and Hsu, P.: Diagnosing ocean feedbacks to the BSISO: SST-modulated surface fluxes and the moist static energy budget, J. Geophys. Res. Atmos., 124, 146–170, https://doi.org/10.1029/2018JD029303, 2019.

Hendon, H. H.: Impact of air–sea coupling on the Madden–Julian oscillation in a general circulation model, J. Atmos. Sci., 57(24), 3939–3952, https://doi.org/10.1175/1520-0469(2001)058<3939:IOASCO>2.0.CO;2, 2000.

Hirons, L. C., Klingaman, N. P. and Woolnough, S. J.: MetUM-GOML1: a near-globally coupled atmosphere–ocean-mixed-layer model, Geosci. Model Dev., 8(2), 363–379, https://doi.org/10.5194/gmd-8-363-2015, 2015.

Hsu, P.-C., and Li, T.: Role of the boundary layer moisture asymmetry in causing the eastward propagation of the Madden-Julian Oscillation. J. Climate, 25, 4914–4931, https://doi.org/10.1175/JCLI-D-11-00310.1, 2012.

Hsu, P.-C., Lee, J.-Y. and Ha, K.-J.: Influence of boreal summer intraseasonal oscillation on rainfall extremes in southern China, Int. J. Climatol., 36(3), 1403–1412, https://doi.org/10.1002/joc.4433, 2016.

Hsu, P.-C., Lee, J.-Y., Ha, K.-J. and Tsou, C.-H.: Influences of boreal summer intraseasonal oscillation on heat waves in monsoon Asia, J. Climate, 30(18), 7191–7211, https://doi.org/10.1175/JCLI-D-16-0505.1, 2017.

Hsu, P.-C., Qian, Y., Liu, Y., Murakami, H. and Gao, Y.: Role of abnormally enhanced MJO over the Western Pacific in the formation and subseasonal predictability of the record-breaking Northeast Asian heatwave in the summer of 2018. J. Climate, 33, 3333–3349, https://doi.org/10.1175/JCLI-D-19-0337.1, 2020.

Hu, W., Duan, A. and Wu, G.: Impact of subdaily air–sea interaction on simulating intraseasonal oscillations over the tropical Asian monsoon region, J. Climate, 28(3), 1057–1073, https://doi.org/10.1175/JCLI-D-14-00407.1, 2015.

Hu, W., Duan, A. and He, B.: Evaluation of intra-seasonal oscillation simulations in IPCC AR5 coupled GCMs associated with the Asian summer monsoon, Int. J. Climatol., 37, 476–496, https://doi.org/10.1002/joc.5016, 2017.

Huffman, G. J., Adler, R. F., Morrissey, M. M., Bolvin, D. T., Curtis, S., Joyce, R., McGavock, B., and Susskind, J.: Global Precipitation at One-Degree Daily Resolution from Multisatellite Observations, J. Hydrometeorol., 2, 36–50, https://doi.org/10.1175/1525-7541(2001)002<0036:GPAODD>2.0.CO;2, 2001.

Inness, P. M., Slingo, J. M., Guilyardi, E. and Cole, J.: Simulation of the Madden–Julian oscillation in a coupled general circulation model. Part II: The role of the basic state, J. Climate, 16(3), 365–382, https://doi.org/10.1175/1520-0442(2003)016<0365:SOTMJO>2.0.CO;2, 2003.

Jiang, X.: Key processes for the eastward propagation of the Madden-Julian Oscillation based on multimodel simulations. J. Geophys. Res. Atmos., 122, 755–770, https://doi.org/10.1002/2016JD025955, 2017.

Jiang, X., Adames, A. F., Zhao, M., Waliser, D., and Maloney, E.: A unified moisture moist framework for seasonality of MJO propagation. J. Climate, 31, 4215–4224, https://doi.org/10.1175/JCLI-D-17-0671.1, 2018.

Jiang, X., Waliser, D. E., Xavier, P. K., Petch, J., Klingaman, N. P., Woolnough, S. J., Guan, B., Bellon, G., Crueger, T., DeMott, C., Hannay, C., Lin, H., Hu, W., Kim, D., Lappen, C.-L., Lu, M.-M., Ma, H.-Y., Miyakawa, T., Ridout, J. A., Schubert, S. D., Scinocca, J., Seo, K.-H., Shindo, E., Song, X., Stan, C., Tseng, W.-L., Wang, W., Wu, T., Wu, X., Wyser, K., Zhang,

G. J. and Zhu, H.: Vertical structure and physical processes of the Madden-Julian oscillation: Exploring key model physics in climate simulations, J. Geophys. Res. Atmos., 120(10), 4718–4748, https://doi.org/10.1002/2014JD022375, 2015.

Jiang, X., Zhao, M., Maloney, E. D. and Waliser, D. E.: Convective moisture adjustment time scale as a key factor in regulating model amplitude of the Madden-Julian oscillation, Geophys. Res. Lett., 43(19), 10,412-10,419, https://doi.org/10.1002/2016GL070898, 2016.

Kapur, A. and Zhang, C.: Multiplicative MJO forcing of ENSO, J. Climate, 25(23), 8132–8147, https://doi.org/10.1175/JCLI-D-11-00609.1, 2012.

Kessler, W. S., McPhaden, M. J. and Weickmann, K. M.: Forcing of intraseasonal Kelvin waves in the equatorial Pacific, J. Geophys. Res., 100(C6), 10613–10631, https://doi.org/10.1029/95JC00382, 1995.

Khairoutdinov, M., Randall, D. and DeMott, C.: Simulations of the atmospheric general circulation using a cloud-resolving model as a superparameterization of physical processes, J. Atmos. Sci., 62(7), 2136–2154, https://doi.org/10.1175/JAS3453.1, 2005.

Khairoutdinov, M. F. and Randall, D. A.: Cloud resolving modeling of the ARM summer 1997 IOP: Model formulation, results, uncertainties, and sensitivities, J. Atmos. Sci., 60(4), 607–625, https://doi.org/10.1175/1520-0469(2003)060<0607:CRMOTA>2.0.CO;2, 2003.

Klingaman, N. P. and DeMott, C. A.: Mean state biases and interannual variability affect perceived sensitivities of the Madden-Julian oscillation to air-sea coupling, J. Adv. Model. Earth Syst., 12, e2019MS001799, https://doi.org/10.1029/2019MS001799, 2020.

Klingaman, N. P. and Woolnough, S. J.: The role of air-sea coupling in the simulation of the Madden-Julian oscillation in the Hadley Centre model, Q. J. Roy. Meteorol. Soc., 140(684), 2272–2286, https://doi.org/10.1002/qj.2295, 2014.

Klingaman, N. P., Woolnough, S. J., Weller, H. and Slingo, J. M.: The impact of finer-resolution air–sea coupling on the intraseasonal oscillation of the Indian monsoon, J. Climate, 24(10), 2451–2468, https://doi.org/10.1175/2010JCLI3868.1, 2011.

Large, W., McWilliams, J., and Doney, S.: Oceanic vertical mixing: A review and a model with a nonlocal boundary layer parameterization. Rev. Geophys., 32, 363–403, 1994.

Lau, W. K. M. and Waliser, D. E.: Intraseasonal variability in the atmosphere-ocean climate system, 2. ed., Springer [u.a.], Berlin., 2012.

Lee, J.-Y., Wang, B., Wheeler, M. C., Fu, X., Waliser, D. E. and Kang, I.-S.: Real-time multivariate indices for the boreal summer intraseasonal oscillation over the Asian summer monsoon region, Clim. Dyn., 40(1–2), 493–509, https://doi.org/10.1007/s00382-012-1544-4, 2013.

Levine, R. C. and Turner, A. G.: Dependence of Indian monsoon rainfall on moisture fluxes across the Arabian Sea and the impact of coupled model sea surface temperature biases, Clim. Dyn., 38(11–12), 2167–2190, https://doi.org/10.1007/s00382-011-1096-z, 2012.

Li, J., Mao, J. and Wu, G.: A case study of the impact of boreal summer intraseasonal oscillations on Yangtze rainfall, Clim. Dyn., 44(9–10), 2683–2702, https://doi.org/10.1007/s00382-014-2425-9, 2015.

Liebmann, B, Smith, C. A.: Description of a complete (interpolated) outgoing long wave radiation dataset. Bull. Amer. Meteor. Soc., 77, 1275–1277, 1996.

Lin, J.-L., Kiladis, G. N., Mapes, B. E., Weickmann, K. M., Sperber, K. R., Lin, W., Wheeler, M. C., Schubert, S. D., Del Genio, A., Donner, L. J., Emori, S., Gueremy, J.-F., Hourdin, F., Rasch, P. J., Roeckner, E. and Scinocca, J. F.: Tropical intraseasonal variability in 14 IPCC AR4 climate models. Part I: Convective signals, J. Climate, 19(12), 2665–2690, https://doi.org/10.1175/JCLI3735.1, 2006.

Liu, Y., and Hsu, P.-C.: Long-term changes in wintertime persistent heavy rainfall over southern China contributed by the Madden–Julian Oscillation. Atmos. and Oceanic Sci. Lett., 12, 361–368, https://doi.org/10.1080/16742834.2019.1639471, 2019.

Madden, R. A. and Julian, P. R.: Detection of a 40–50 Day Oscillation in the Zonal Wind in the Tropical Pacific, J. Atmos. Sci., 28(5), 702–708, https://doi.org/10.1175/1520-0469(1971)028<0702:DOADOI>2.0.CO;2, 1971.

Madden, R. A. and Julian, P. R.: Description of global-scale circulation cells in the tropics with a 40–50 day period, J. Atmos. Sci., 29(6), 1109–1123, https://doi.org/10.1175/1520-0469(1972)029<1109:DOGSCC>2.0.CO;2, 1972.

Maloney, E. D.: The moist static energy budget of a composite tropical intraseasonal oscillation in a climate model, J. Climate, 22(3), 711–729, https://doi.org/10.1175/2008JCLI2542.1, 2009.

Maloney, E. D. and Hartmann, D. L.: The sensitivity of intraseasonal variability in the NCAR CCM3 to changes in convective parameterization, J. Climate, 14(9), 2015–2034, https://doi.org/10.1175/1520-0442(2001)014<2015:TSOIVI>2.0.CO;2, 2001.

McPhaden, M. J.: Evolution of the 2002/2003 El Nino, Bull. Amer. Meteor. Soc., 85, 677–695, 2004.

Moon, J.-Y., Wang, B., Ha, K.-J. and Lee, J.-Y.: Teleconnections associated with Northern Hemisphere summer monsoon intraseasonal oscillation, Clim. Dyn., 40(11–12), 2761–2774, https://doi.org/10.1007/s00382-012-1394-0, 2013.

Misra, V., Marx, L., Brunke, M. and Zeng, X.: The equatorial Pacific cold tongue bias in a coupled climate model, J. Climate, 21(22), 5852–5869, https://doi.org/10.1175/2008JCLI2205.1, 2008.

Neena, J. M., Waliser, D. and Jiang, X.: Model performance metrics and process diagnostics for boreal summer intraseasonal variability, Clim. Dyn., 48(5–6), 1661–1683, https://doi.org/10.1007/s00382-016-3166-8, 2017.

Randall, D. A., Wood, R. A., Bony, S., Colman, R., Fichefet, T., Fyfe, J., Kattsov, V., Pitman, A., Shukla, J., Srinivasan, J., Stouffer, R. J., Sumi, A., Taylor, K. E., AchutaRao, K., Allan, R., Berger, A., Blatter, H., Bonfils, C., Boone, A., Bretherton, C., Broccoli, A., Brovkin, V., Dirmeyer, P., Doutriaux, C., Drange, H., Frei, A., Ganopolski, A., Gent, P., Gleckler, P., Goosse, H., Graham, R., Gregory, J. M., Gudgel, R., Hall, A., Hallegatte, S., Hasumi, H., Henderson-Sellers, A., Hendon, H., Hodges, K., Holland, M., Holtslag, A. A. M., Hunke, E., Huybrechts, P., Ingram, W., Joos, F., Kirtman, B., Klein, S., Koster, R., Kushner, P., Lanzante, J., Latif, M., Pavlova, T., Federationi, R., Petoukhov, V., Phillips, T., Power, S., Rahmstorf, S., Raper, S. C. B., Renssen, H., Rind, D., Roberts, M., Rosati, A., Schär, C., Schmittner, A., Scinocca, J., Seidov, D., Slater, A. G., Slingo, J., Smith, D., Soden, B., Stern, W., Stone, D. A., Sudo, K., Takemura, T., Tselioudis, G., Webb, M., Wild, M., Manzini, E., Matsuno, T. and McAvaney, B.: Climate models and their evaluation, , 74, 2007.

Ren, X., Yang, X.-Q. and Sun, X.: Zonal oscillation of western Pacific subtropical high and subseasonal SST variations during Yangtze persistent heavy rainfall events, J. Climate, 26(22), 8929–8946, https://doi.org/10.1175/JCLI-D-12-00861.1, 2013.

Sabeerali, C. T., Ramu Dandi, A., Dhakate, A., Salunke, K., Mahapatra, S. and Rao, S. A.: Simulation of boreal summer intraseasonal oscillations in the latest CMIP5 coupled GCMs, J. Geophys. Res. Atmos., 118(10), 4401–4420, https://doi.org/10.1002/jgrd.50403, 2013.

Seo, K.-H., Schemm, J.-K. E., Wang, W. and Kumar, A.: The boreal summer intraseasonal oscillation simulated in the NCEP climate forecast system: The effect of sea surface temperature, Mon. Weather Rev., 135(5), 1807–1827, https://doi.org/10.1175/MWR3369.1, 2007.

Smith, D. M. and Murphy, J. M.: An objective ocean temperature and salinity analysis using covariances from a global climate model, J. Geophys. Res., 112(C2), C02022, https://doi.org/10.1029/2005JC003172, 2007.

Sperber, K. R. and Annamalai, H.: Coupled model simulations of boreal summer intraseasonal (30–50 day) variability, Part 1: Systematic errors and caution on use of metrics, Clim. Dyn., 31(2–3), 345–372, https://doi.org/10.1007/s00382-008-0367-9, 2008.

Sperber, K. R., Slingo, J. M. and Annamalai, H.: Predictability and the relationship between subseasonal and interannual variability during the Asian summer monsoon, Q. J. Roy. Meteorol. Soc., 126(568), 2545–2574, https://doi.org/10.1002/qj.49712656810, 2000.

Sperber, K. R., Gualdi, S., Legutke, S. and Gayler, V.: The Madden–Julian oscillation in ECHAM4 coupled and uncoupled general circulation models, Clim. Dyn., 25(2–3), 117–140, https://doi.org/10.1007/s00382-005-0026-3, 2005.

Sperber, K. R., Annamalai, H., Kang, I.-S., Kitoh, A., Moise, A., Turner, A., Wang, B. and Zhou, T.: The Asian summer monsoon: an intercomparison of CMIP5 vs. CMIP3 simulations of the late 20th century, Clim. Dyn., 41(9–10), 2711–2744, https://doi.org/10.1007/s00382-012-1607-6, 2013.

Stan, C.: The role of SST variability in the simulation of the MJO, Clim. Dyn., 51(7–8), 2943–2964, https://dor.org/10.1007/s00382-017-4058-2, 2018.

Stan, C., Khairoutdinov, M., DeMott, C. A., Krishnamurthy, V., Straus, D. M., Randall, D. A., Kinter, J. L. and Shukla, J.: An ocean-atmosphere climate simulation with an embedded cloud resolving model, Geophys. Res. Lett., 37(1), L01702, https://doi.org/10.1029/2009GL040822, 2010.

Waliser, D. E., Jin, K., Kang, I.-S., Stern, W. F., Schubert, S. D., Wu, M. L. C., Lau, K.-M., Lee, M.-I., Krishnamurthy, V., Kitoh, A., Meehl, G. A., Galin, V. Y., Satyan, V., Mandke, S. K., Wu, G., Liu, Y. and Park, C.-K.: AGCM simulations of intraseasonal variability associated with the Asian summer monsoon, Clim. Dyn., 21(5–6), 423–446, https://doi.org/10.1007/s00382-003-0337-1, 2003.

Waliser, D. E., Lau, K. M. and Kim, J.-H.: The influence of coupled sea surface temperatures on the Madden-Julian Oscillation: A model perturbation experiment, J. Atmos. Sci., 56, 333–358, 1999.

Wang, B., Webster, P. J. and Teng, H.: Antecedents and self-induction of active-break south Asian monsoon unraveled by satellites, Geophys. Res. Lett., 32(4), L04704, https://doi.org/10.1029/2004GL020996, 2005.

Wang, B., Webster, P., Kikuchi, K., Yasunari, T. and Qi, Y.: Boreal summer quasi-monthly oscillation in the global tropics, Clim. Dyn., 27(7–8), 661–675, https://doi.org/10.1007/s00382-006-0163-3, 2006.

Weare, B. C., Strub, P. T. and Samuel, M. D.: Annual mean surface heat fluxes in the tropical Pacific ocean, J. Phys. Oceanogr., 11(5), 705–717, https://doi.org/10.1175/1520-0485(1981)011<0705:AMSHFI>2.0.CO;2, 1981.

Weaver, S. J., Wang, W., Chen, M. and Kumar, A.: Representation of MJO variability in the NCEP climate forecast system, J. Climate, 24(17), 4676–4694, https://doi.org/10.1175/2011JCLI4188.1, 2011.

Wheeler, M. and Kiladis, G. N.: Convectively coupled equatorial waves: Analysis of clouds and temperature in the wavenumber–frequency domain, J. Atmos. Sci., 56(3), 374–399, https://doi.org/10.1175/1520-0469(1999)056<0374:CCEWAO>2.0.CO;2, 1999.

Woolnough, S. J., Vitart, F. and Balmaseda, M. A.: The role of the ocean in the Madden–Julian oscillation: Implications for MJO prediction, Q. J. Roy. Meteorol. Soc., 133(622), 117–128, https://doi.org/10.1002/qj.4, 2007.

Wu, X., Deng, L., Song, X., Vettoretti, G., Peltier, W. R. and Zhang, G. J.: Impact of a modified convective scheme on the Madden-Julian Oscillation and El Niño-Southern Oscillation in a coupled climate model, Geophys. Res. Lett., 34(16), L16823, https://doi.org/10.1029/2007GL030637, 2007.

Yasunari, T.: Cloudiness fluctuations associated with the northern summer monsoon, J. Meteorol. Soc. Japan, 57(3), 16, 1979.

Zhang, C.: Madden-Julian oscillation, Rev. Geophys., 43, RG2003, https://doi.org/10.1029/2004RG000158, 2005.

Zhang, C. and Gottschalck, J.: SST anomalies of ENSO and the Madden–Julian oscillation in the equatorial Pacific, J. Climate, 15(17), 2429–2445, https://doi.org/10.1175/1520-0442(2002)015<2429:SAOEAT>2.0.CO;2, 2002.

Table 1: List of simulations analysed in this study, including the experiment name, model, ~~type, and~~ ocean climatology condition ~~to which~~used by the model ~~is constrained~~to constrain (coupled model) or ~~prescribed~~as forcing (atmospheric-only model~~).~~), and design purpose.

~~Name~~Exp	Model	~~Type~~Ocean surface	~~Ocean surface~~Purpose
SPK-OBS	SPCAM3-KPP	~~CGCM~~SST climatology from observation	~~Climatology from observation~~Understanding ocean mean-state bias effect (SPK-OBS vs. SPK-SPC)
SPK-SPC	SPCAM3-KPP	~~CGCM~~SST climatology from SPC	~~Climatology from SPCCSM3~~
SPA-KOBS	SPCAM3	~~AGCM~~31-day smoothed SST from SPK-OBS	~~31-day smoothed SST from SPK-OBS~~Understanding air-sea coupling effect under observed mean state (vs. SPK-OBS)
SPA-KSPC	SPCAM3	~~AGCM~~31-day smoothed SST from SPK-SPC	~~31-day smoothed SST from SPK-SPC~~Understanding air-sea coupling effect under SPC mean state (vs. SPK-SPC)

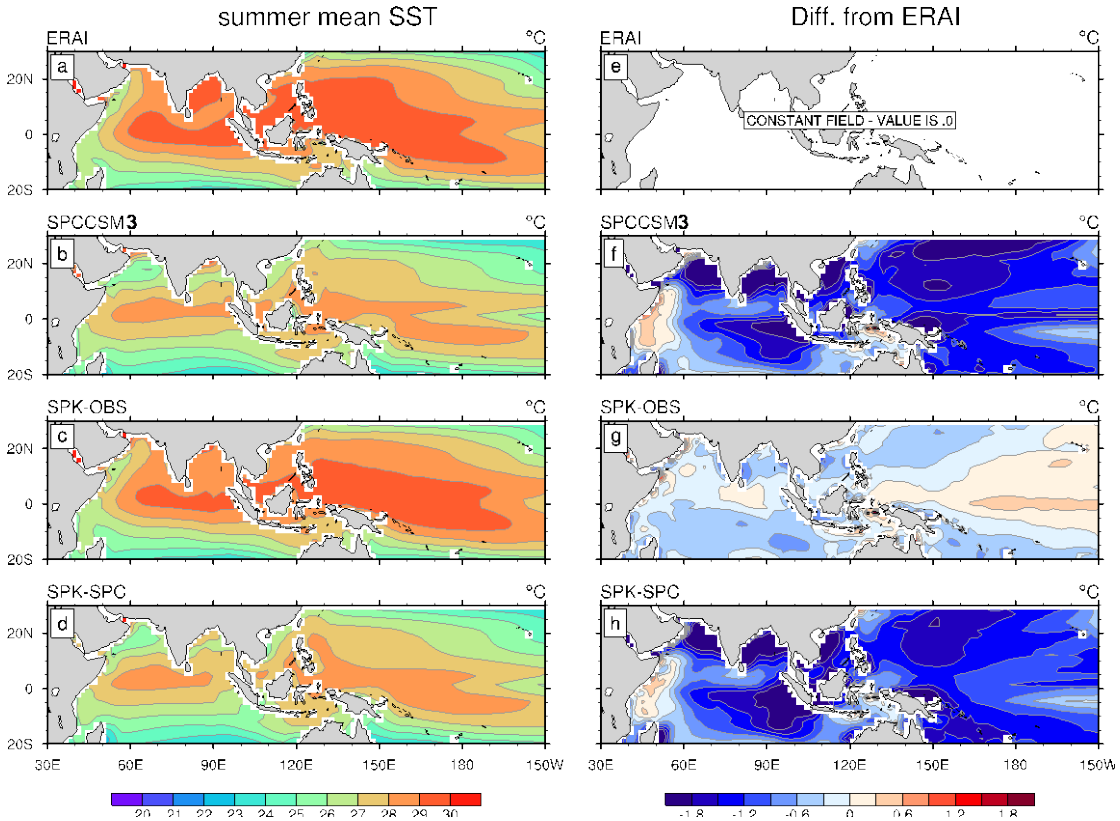

Figure 1: May–October mean SST for (a) ERAI, (b) SPCCSM3, (c) SPK-OBS, and (d) SPK-SPC. (f)–(h) are calculated differences between (b)–(d) and (a).

615

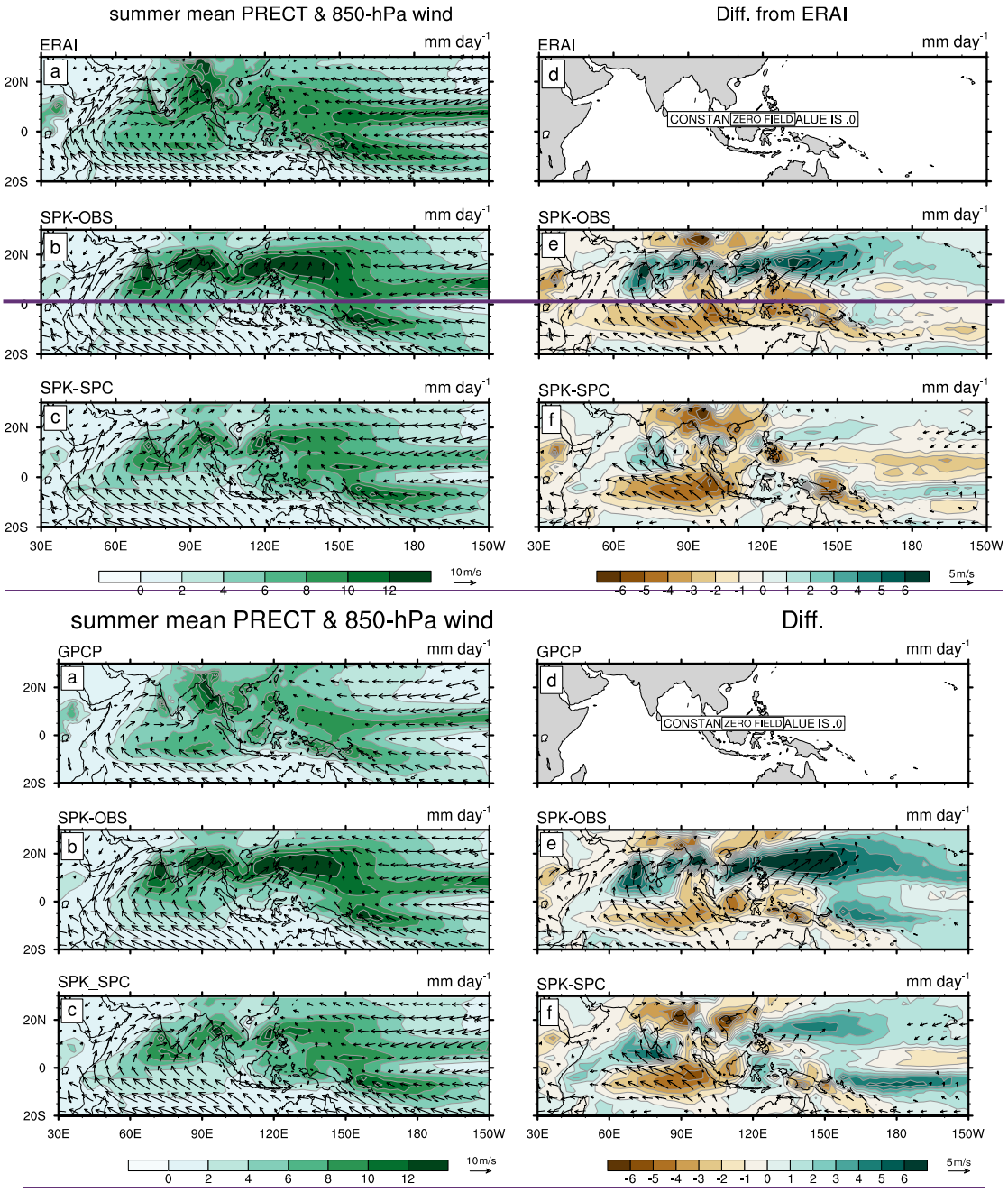

Figure 2: May–October mean precipitation (shading) and 850-hPa wind (vector; with amplitude > ~~1~~3.5 m s^{-1}) for (a) GPCP precipitation and ERAI 850-hPa wind, (b) SPK-OBS and (c) SPK-SPC. (e)–(f) are calculated differences between (b)–(c) and (a).

620

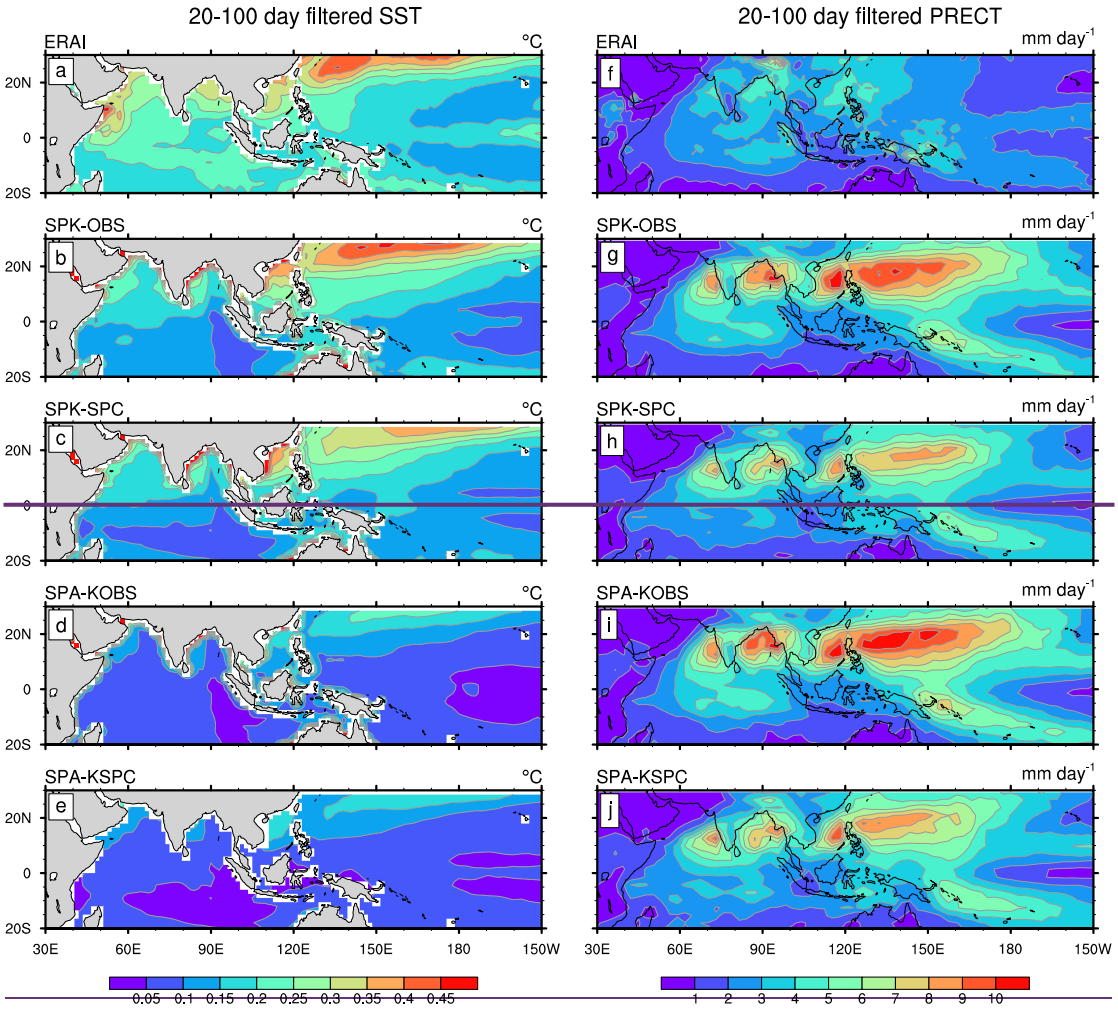
20-100 day filtered SST
20-100 day filtered PRECT
ERAI
°C
mm day-1
a
f
SPK-OBS
b
g
SPK-SPC
c
h
SPA-KOBS
d
i
SPA-KSPC
e
j
20N
0
20S
30E
60E
90E
120E
150E
180
150W
0.05 0.1 0.15 0.2 0.25 0.3 0.35 0.4 0.45
1 2 3 4 5 6 7 8 9 10

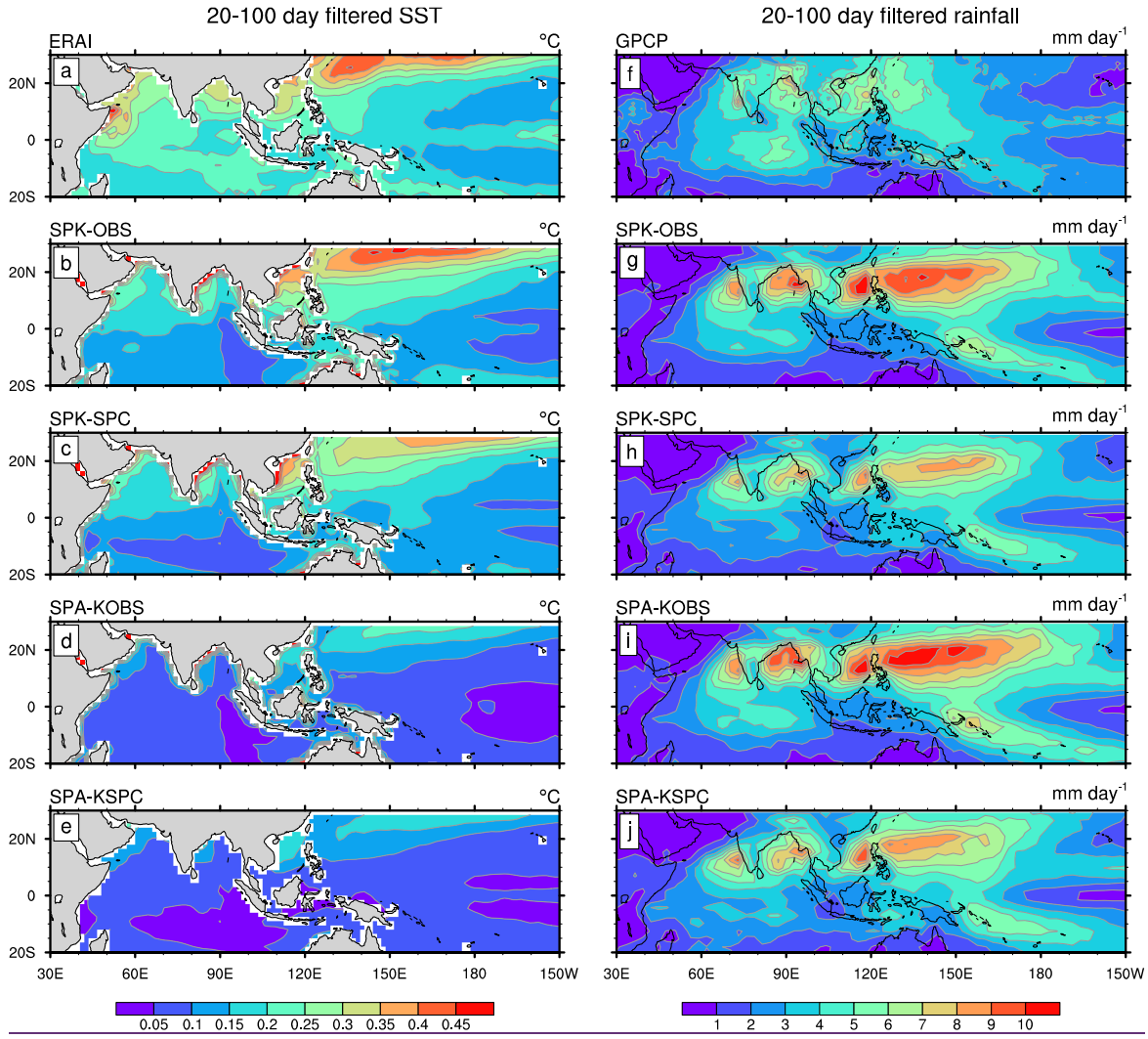

Figure 3: May–October standard deviations of 20–100-day-filtered (left column) SST and (right column) precipitation for (a, f) ERAI SST and GPCP precipitation, (b, g) SPK-OBS, (c, h) SPK-SPC, (d, i) SPA-KOBS, and (e, j) SPA-KSPC.

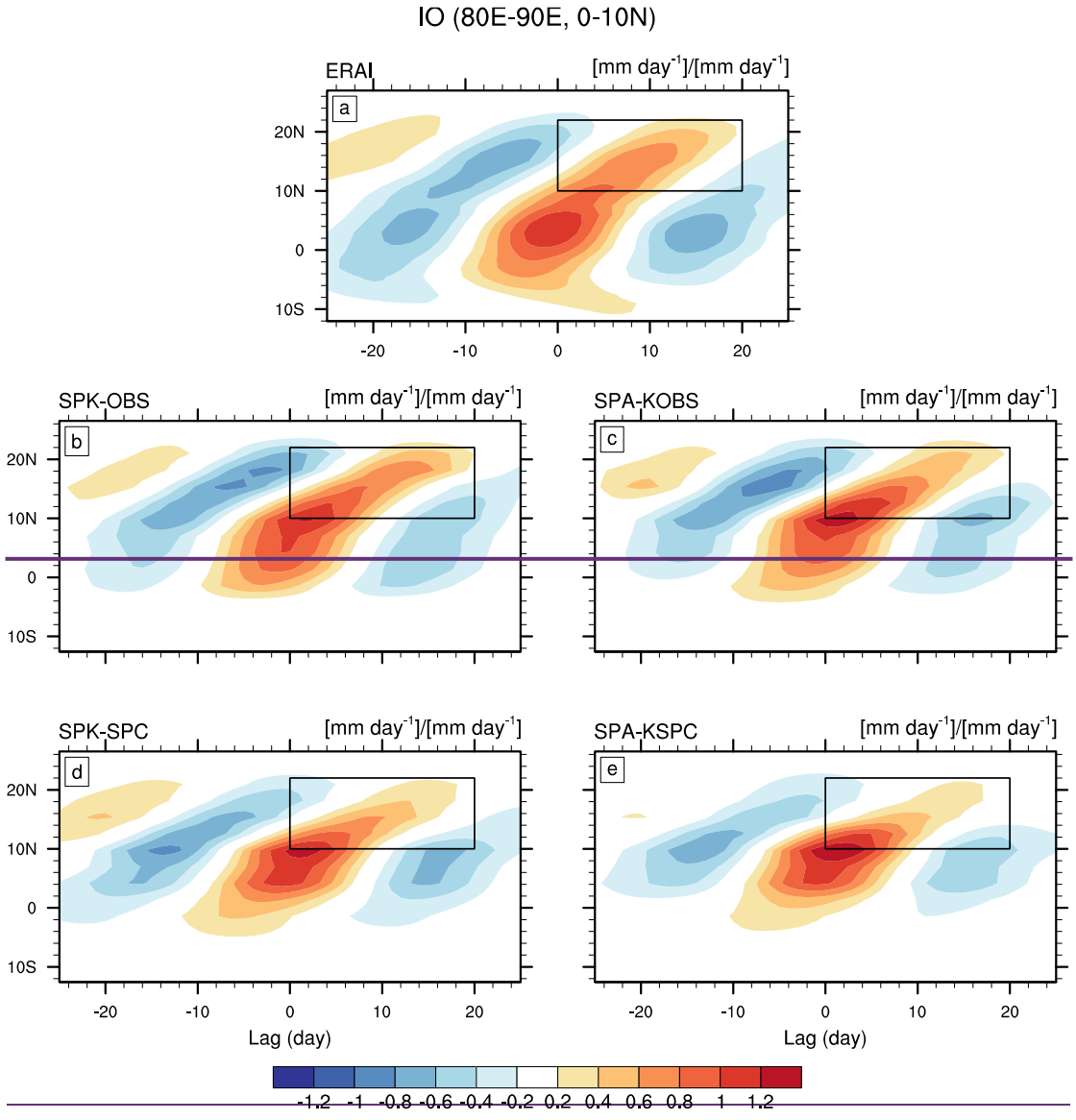
IO (80E-90E, 0-10N)
ERAI
[mm day-1]/[mm day-1]
a
20N
10N
0
10S
-20
-10
0
10
20
SPK-OBS
b
SPA-KOBS
c
SPK-SPC
d
SPA-KSPC
e
Lag (day)
-1.2 -1 -0.8 -0.6 -0.4 -0.2 0.2 0.4 0.6 0.8 1 1.2

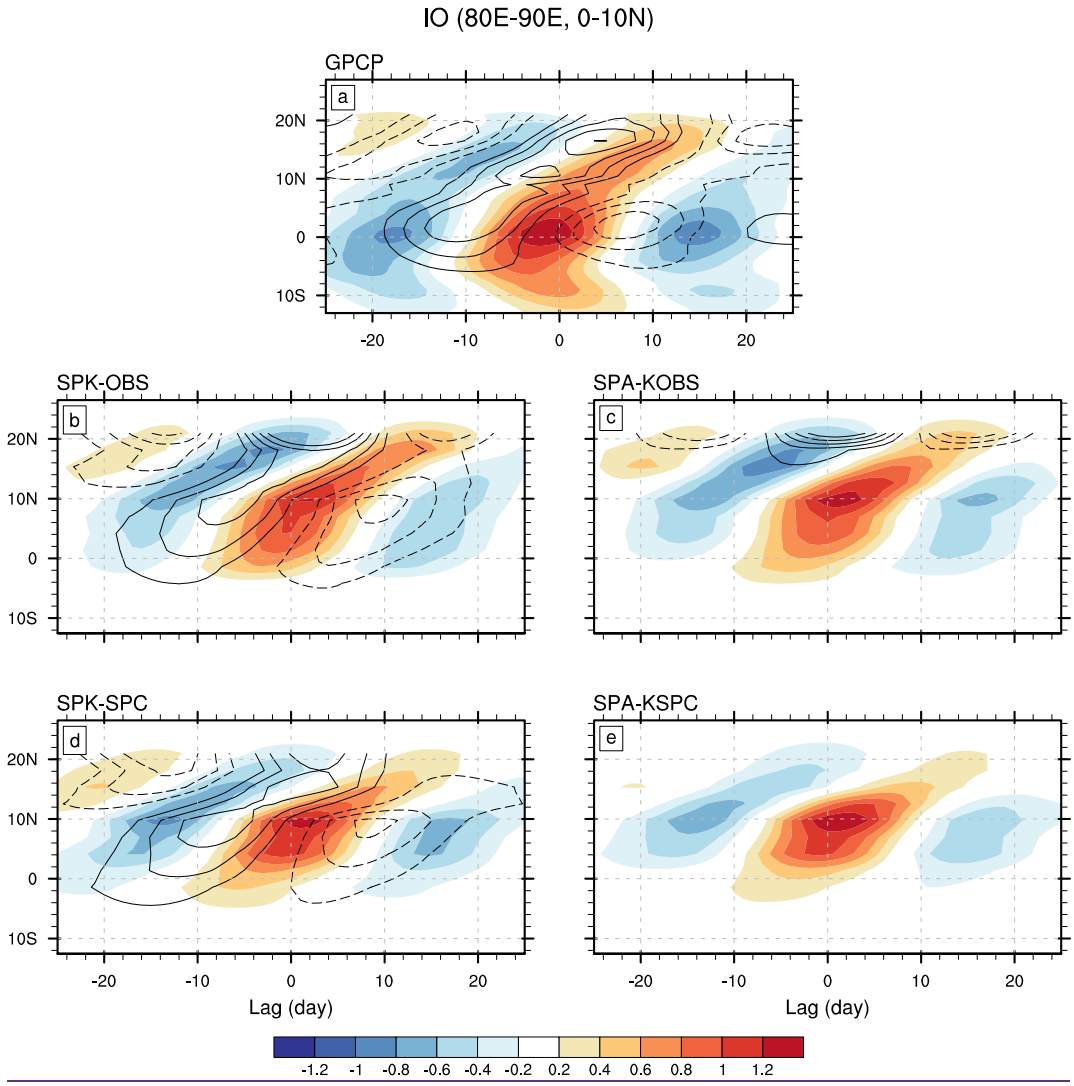

Figure 4: Lagged regression coefficients of 80°–90°E averaged intraseasonal precipitation (shading; [mm day^{-1}]/[mm day^{-1}]) and SST (contour; [°C]/[mm day^{-1}]) onto (80°–90°E, 0°–10°N) averaged intraseasonal precipitation for (a) GPCP precipitation and ERAI SST, (b) SPK-OBS, (c) SPA-KOBS, (d) SPK-SPC, and (e) SPA-KSPC. ~~Black box in each panel denotes (10ºN–22ºN, Lags~~Contour interval is 0~~–20)~~.001 [°C]/[mm day^{-1}]; the zero contour is omitted.

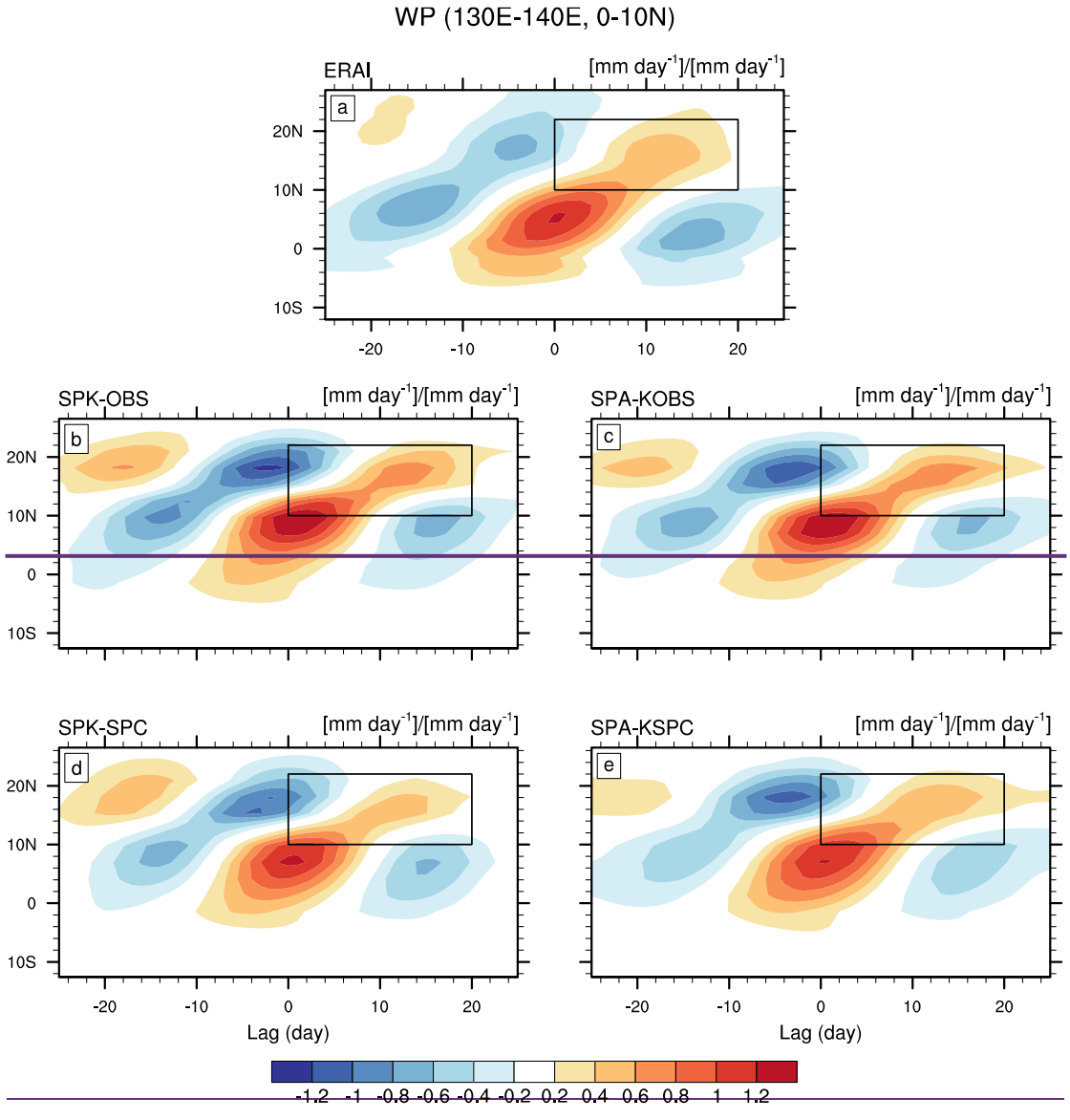
WP (130E-140E, 0-10N)
ERAI
[mm day-1]/[mm day-1]
a
20N
10N
0
10S
-20
-10
0
10
20
SPK-OBS
b
SPA-KOBS
c
SPK-SPC
d
SPA-KSPC
e
Lag (day)
-1.2 -1 -0.8 -0.6 -0.4 -0.2 0.2 0.4 0.6 0.8 1 1.2

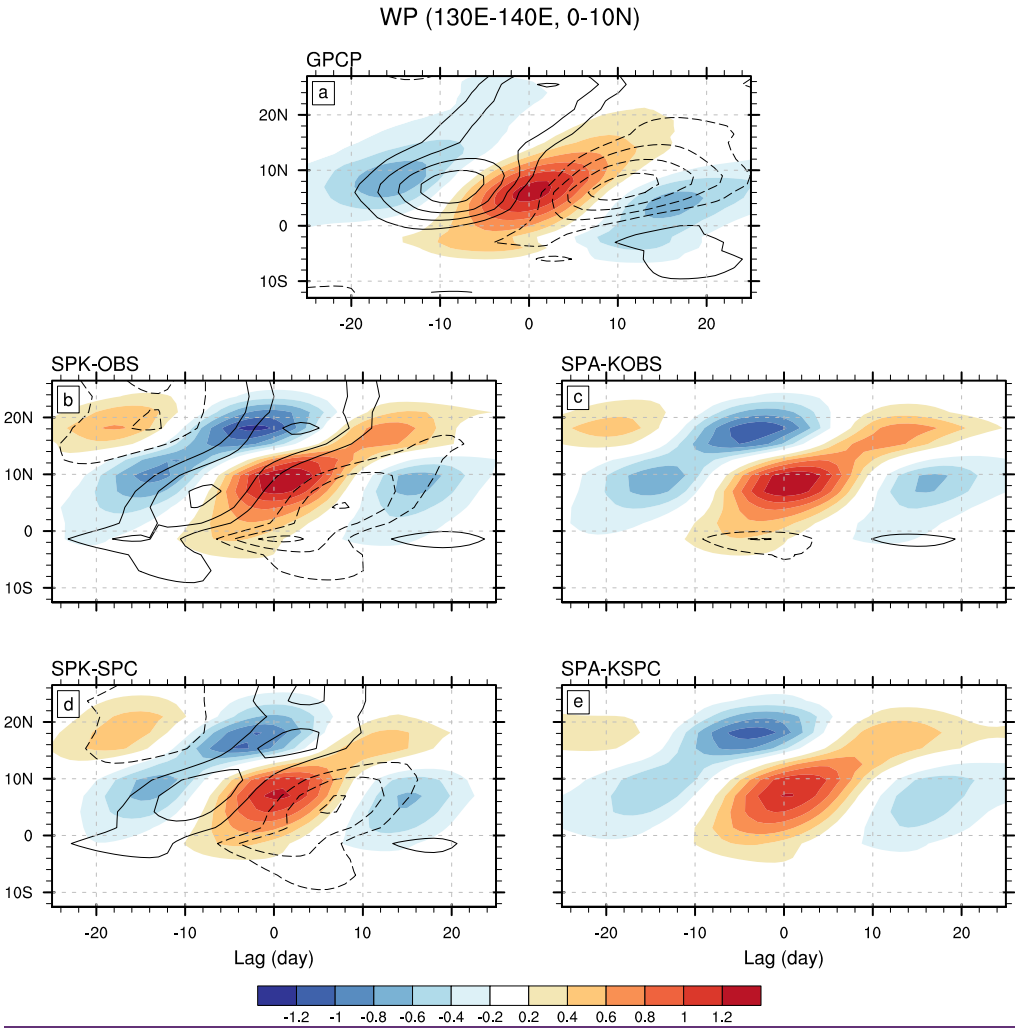

635

Figure 5: Same as Fig. 4, except for 130°–140°E averaged intraseasonal precipitation and SST regressed onto (130°–140°E, 0°–10°N) averaged intraseasonal precipitation.

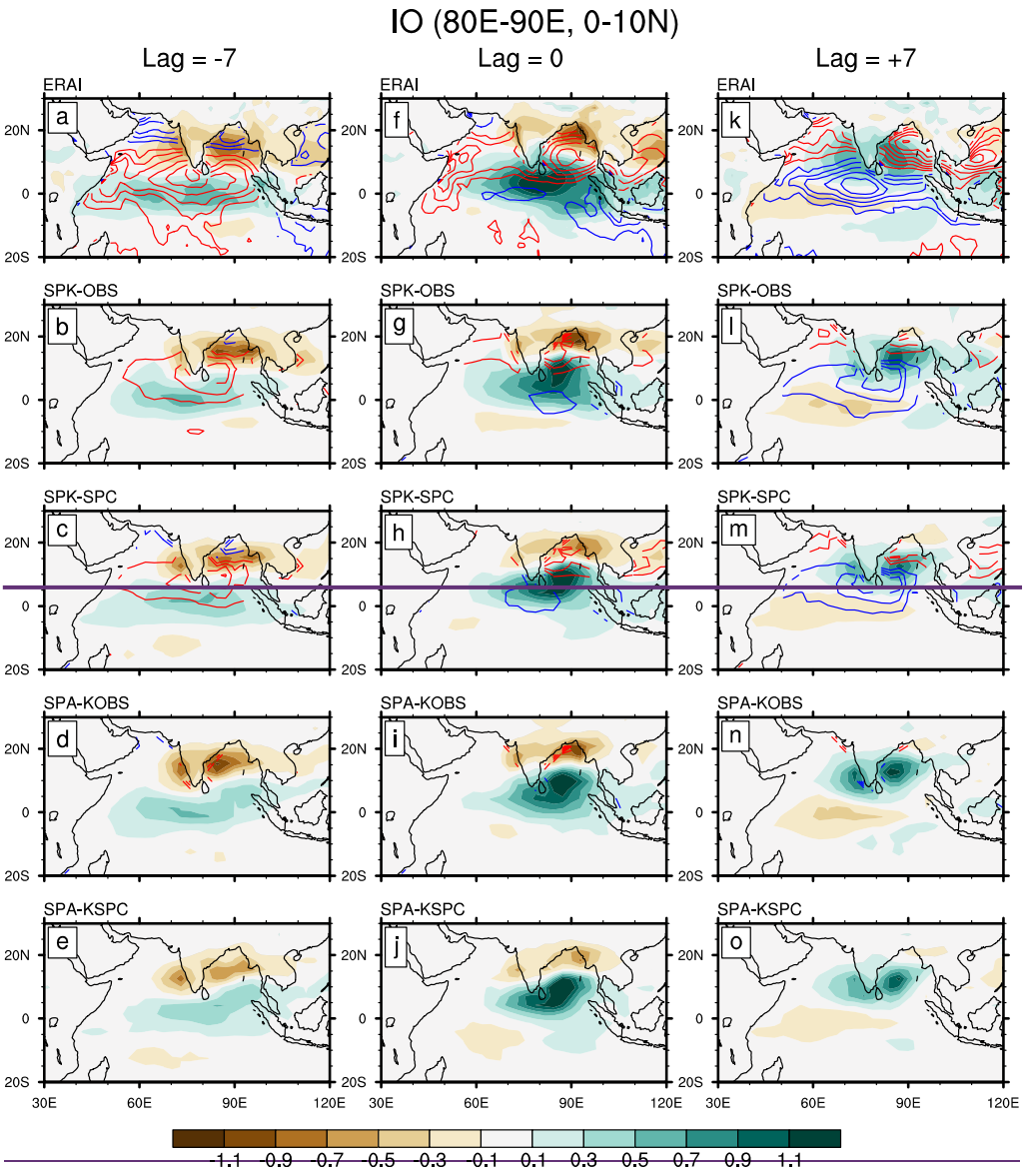
IO (80E-90E, 0-10N)
Lag = -7
Lag = 0
Lag = +7
ERAI
SPK-OBS
SPK-SPC
SPA-KOBS
SPA-KSPC
a
b
c
d
e
f
g
h
i
j
k
l
m
n
o
20N
0
20S
30E
60E
90E
120E
-1.1
-0.9
-0.7
-0.5
-0.3
-0.1
0.1
0.3
0.5
0.7
0.9
1.1

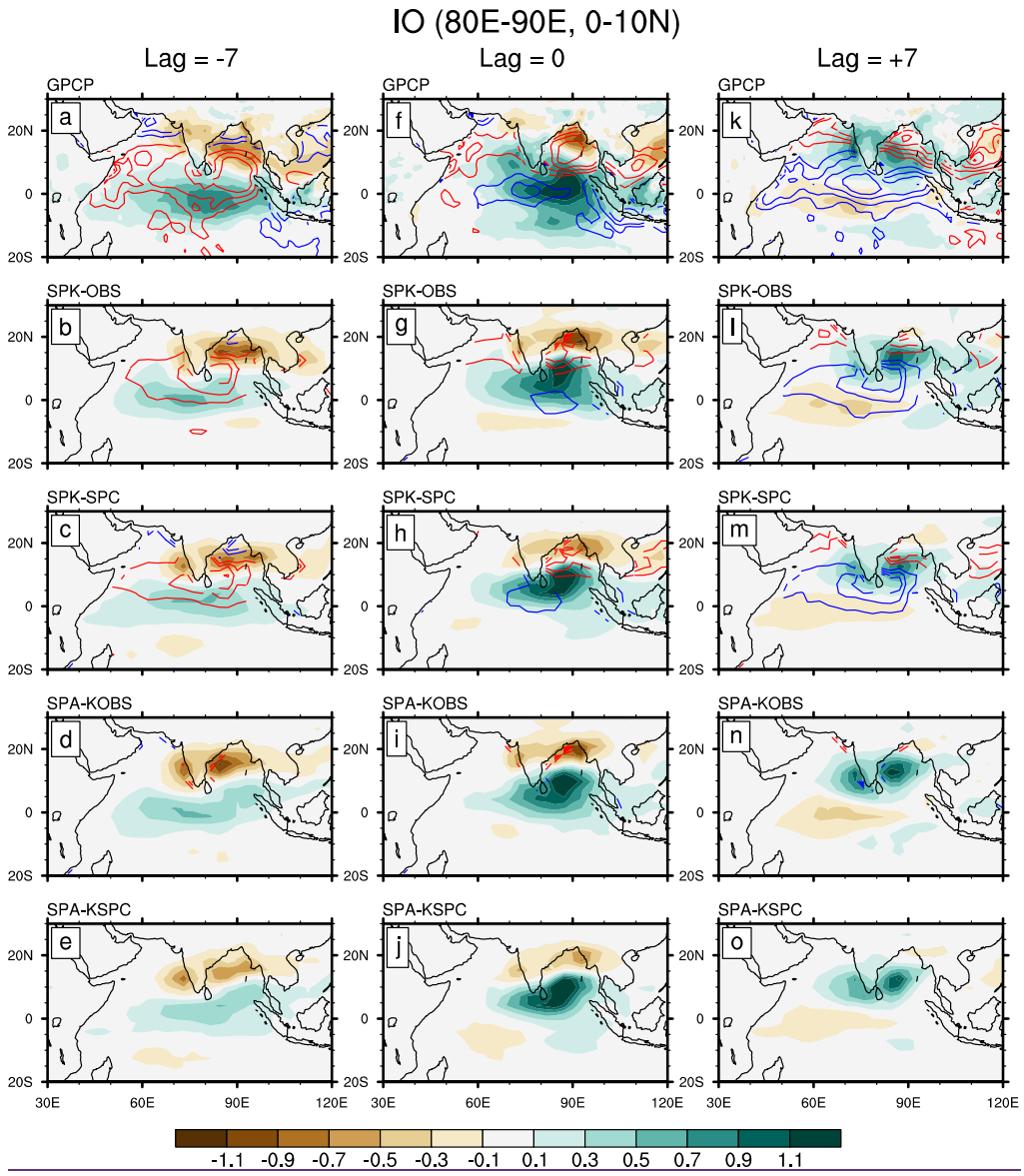

Figure 6: Regression coefficients of intraseasonal precipitation (shading; [mm day^{-1}]/[mm day^{-1}]) and SST (contour; [℃]/[mm day^{-1}]) onto (80°–90°E, 0°–10°N) averaged intraseasonal precipitation over the Indian Ocean at lags of (left column) -7, (middle column) 0 and (right column) +7 days, for (a, f, k) GPCP precipitation and ERAI SST, (b, g, l) SPK-OBS, (c, h, m) SPK-SPC, (d, i, n) SPA-KOBS, and (e, j, o) SPA-KSPC. The contour interval is 0.01 [℃]/[mm day^{-1}]; positive (negative) values are represented by red (blue) lines.

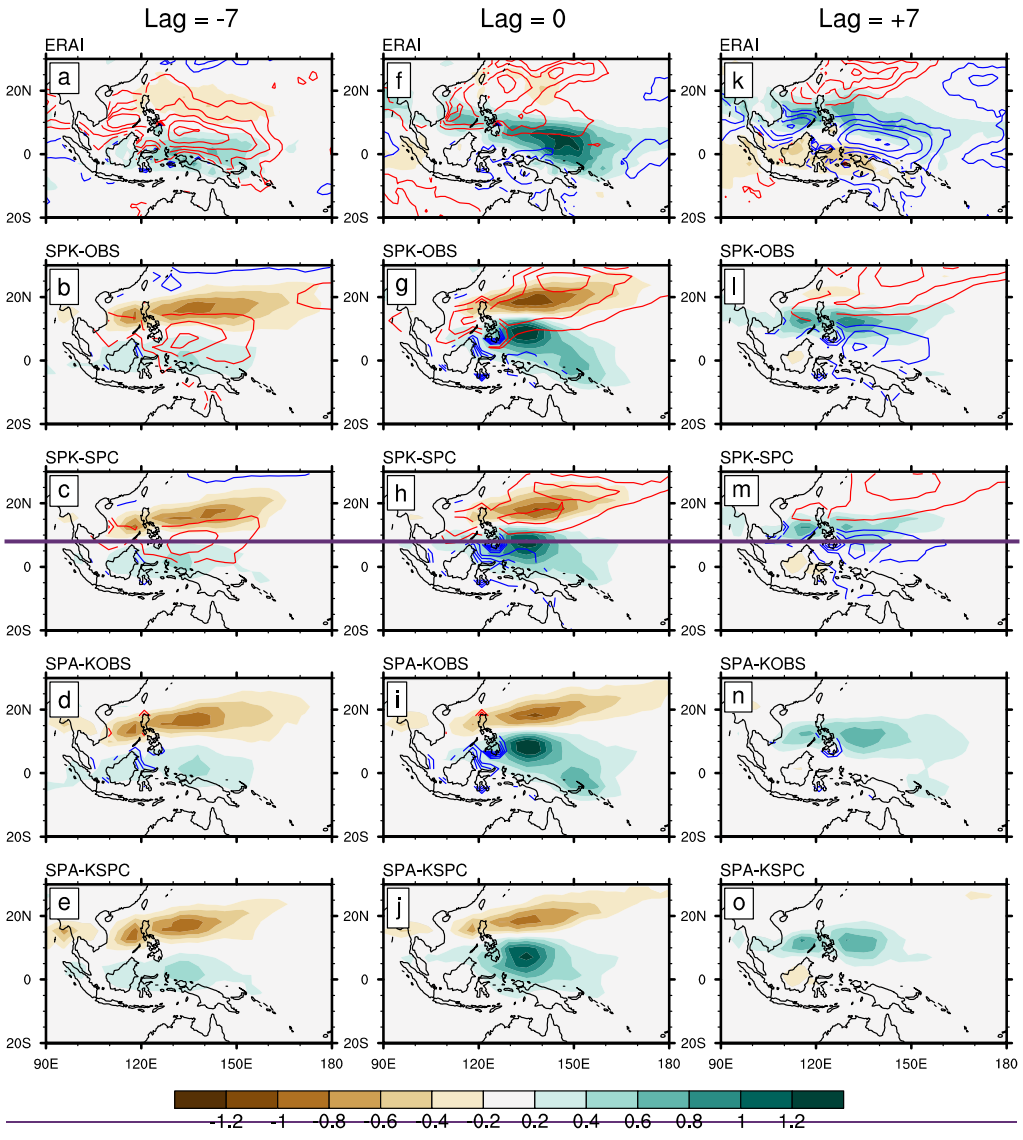
WP (130E-140E, 0-10N)
Lag = -7
Lag = 0
Lag = +7
ERAI
SPK-OBS
SPK-SPC
SPA-KOBS
SPA-KSPC
a
b
c
d
e
f
g
h
i
j
k
l
m
n
o
20N
0
20S
90E
120E
150E
180
-1.2
-1
-0.8
-0.6
-0.4
-0.2
0.2
0.4
0.6
0.8
1
1.2

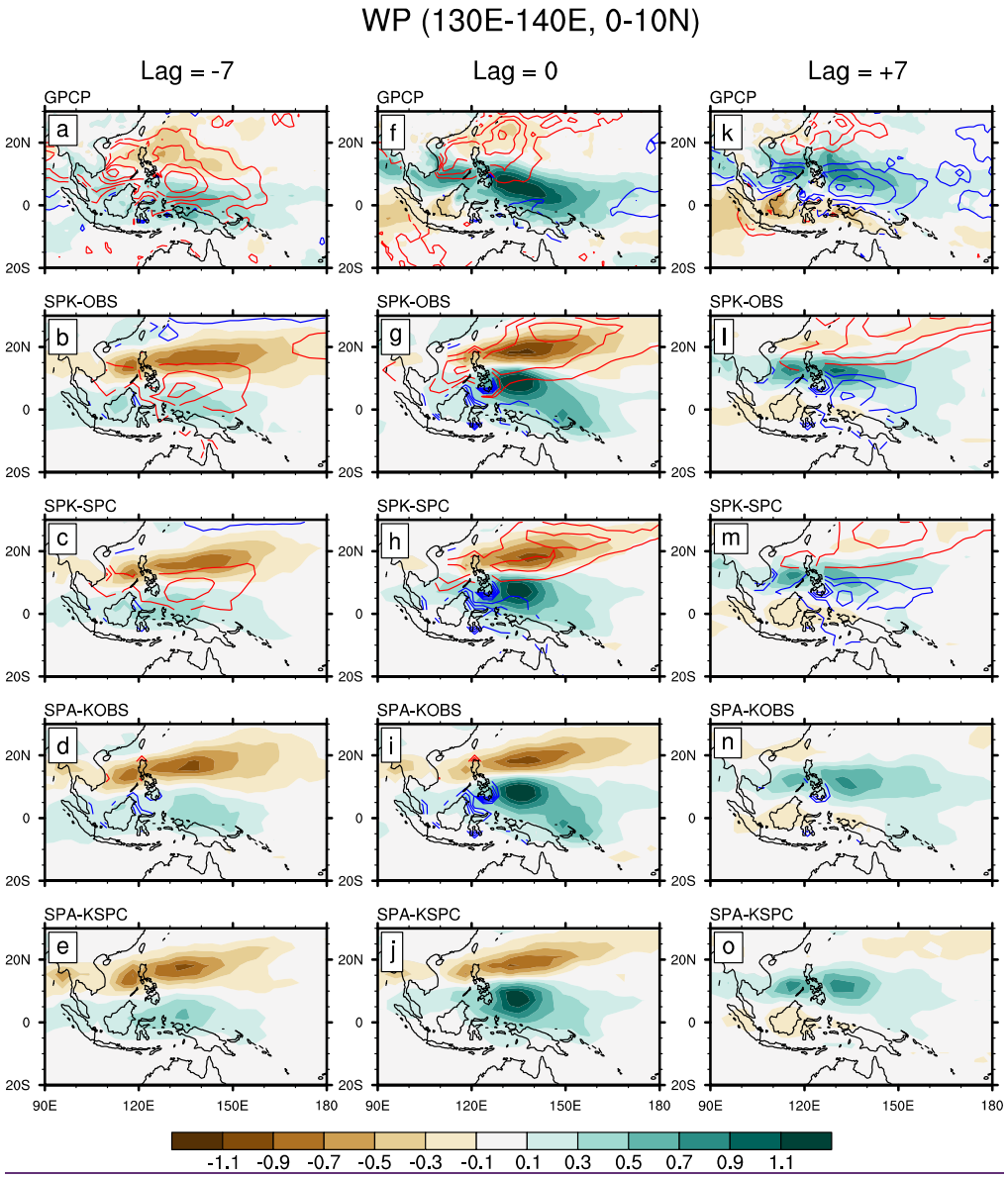

Figure 7: Same as Fig. 6, except for variables regressed onto (130~~°E~~–°–140°E, 0°–10°N) averaged intraseasonal precipitation over the western Pacific.

650

SST effect

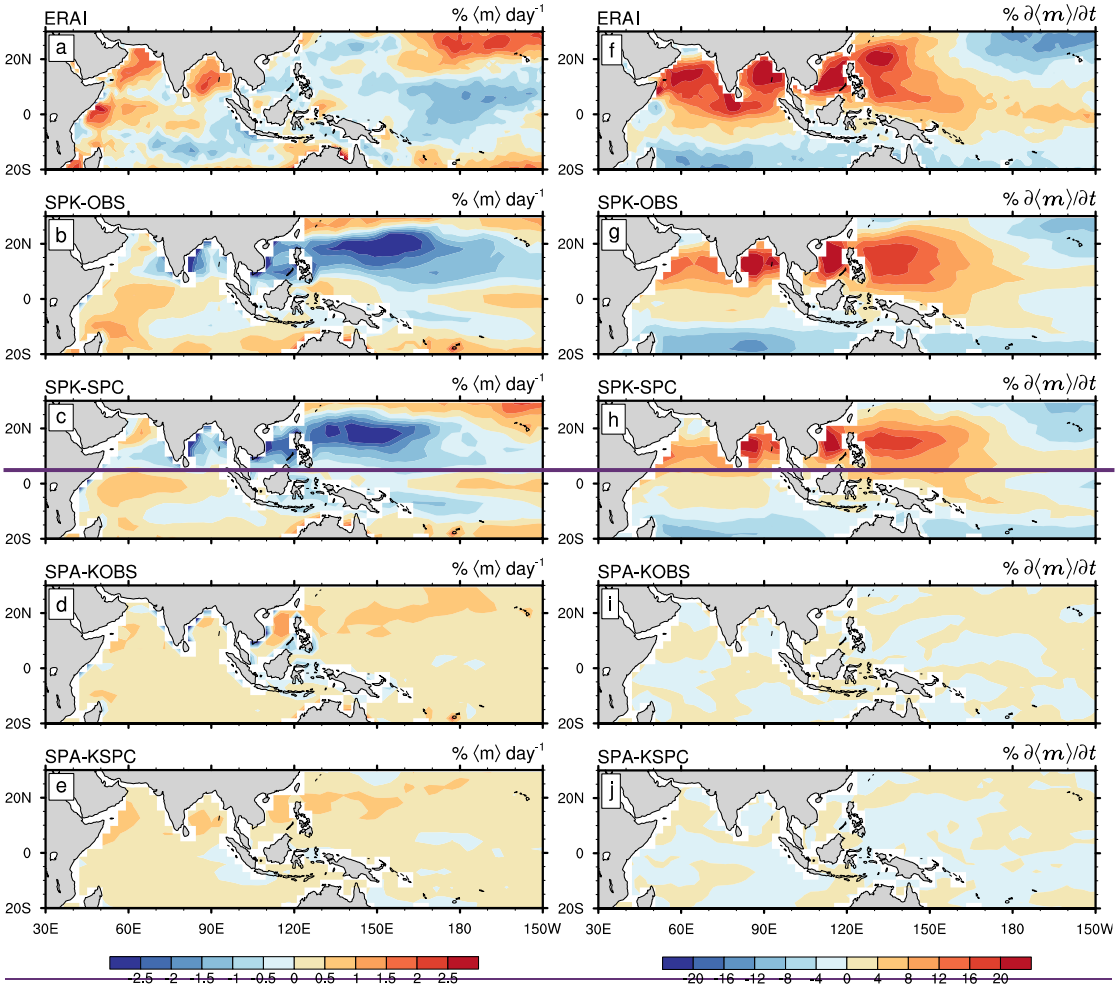
ERAI
% ⟨m⟩ day-1
a
20N
0
20S
SPK-OBS
b
SPK-SPC
c
SPA-KOBS
d
SPA-KSPC
e
30E
60E
90E
120E
150E
180
150W
-2.5 -2 -1.5 -1 -0.5 0 0.5 1 1.5 2 2.5
ERAI
% ∂⟨m⟩/∂t
f
SPK-OBS
g
SPK-SPC
h
SPA-KOBS
i
SPA-KSPC
j
-20 -16 -12 -8 -4 0 4 8 12 16 20

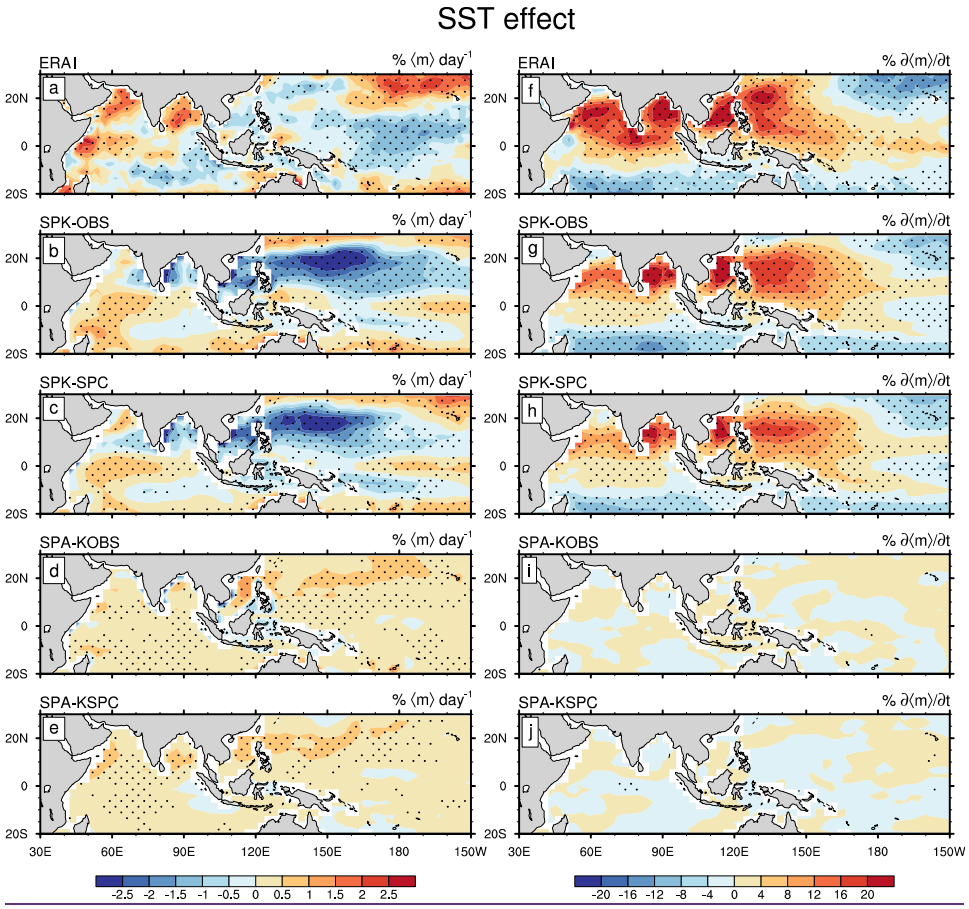

Figure 8: SST effect on (left column) $\langle \boldsymbol{m} \rangle$ and (right column) $\boldsymbol{\partial \langle m \rangle / \partial t}$ through the modification of surface turbulent fluxes for (a, f) ERAI, (b, g) SPK-OBS, (c, h) SPK-SPC, (d, i) SPA-KOBS, and (e, j) SPA-KSPC. Stippling indicates regression coefficient is significant at the 95% confidence level.

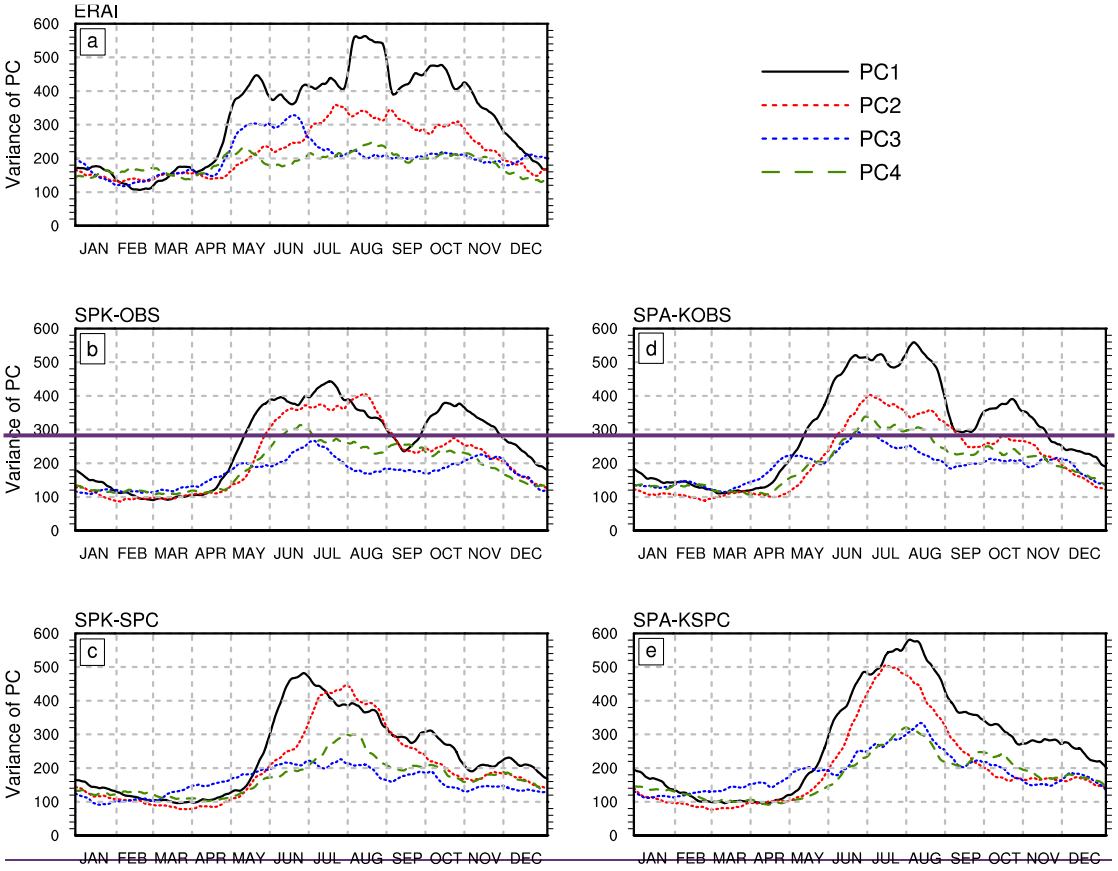
ERAI
a
Variance of PC
600
500
400
300
200
100
0
JAN FEB MAR APR MAY JUN JUL AUG SEP OCT NOV DEC
PC1
PC2
PC3
PC4
SPK-OBS
b
SPA-KOBS
d
SPK-SPC
c
SPA-KSPC
e

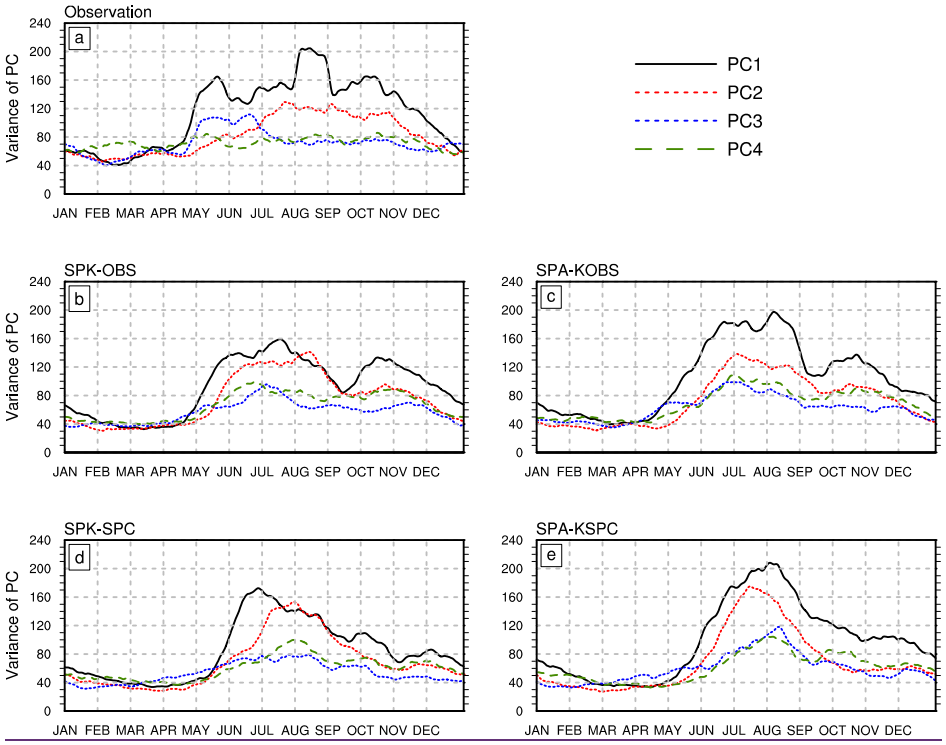

Figure 9: Seasonal cycle of variance of the four leading PCs for (a) NOAA OLR and ERAI u850, (b) SPK-OBS, (c) SPK-SPC, (d) SPA-KOBS, and (e) SPA-KSPC. A 30-day running mean is applied to the seasonal cycle of each ~~dataset~~variable.

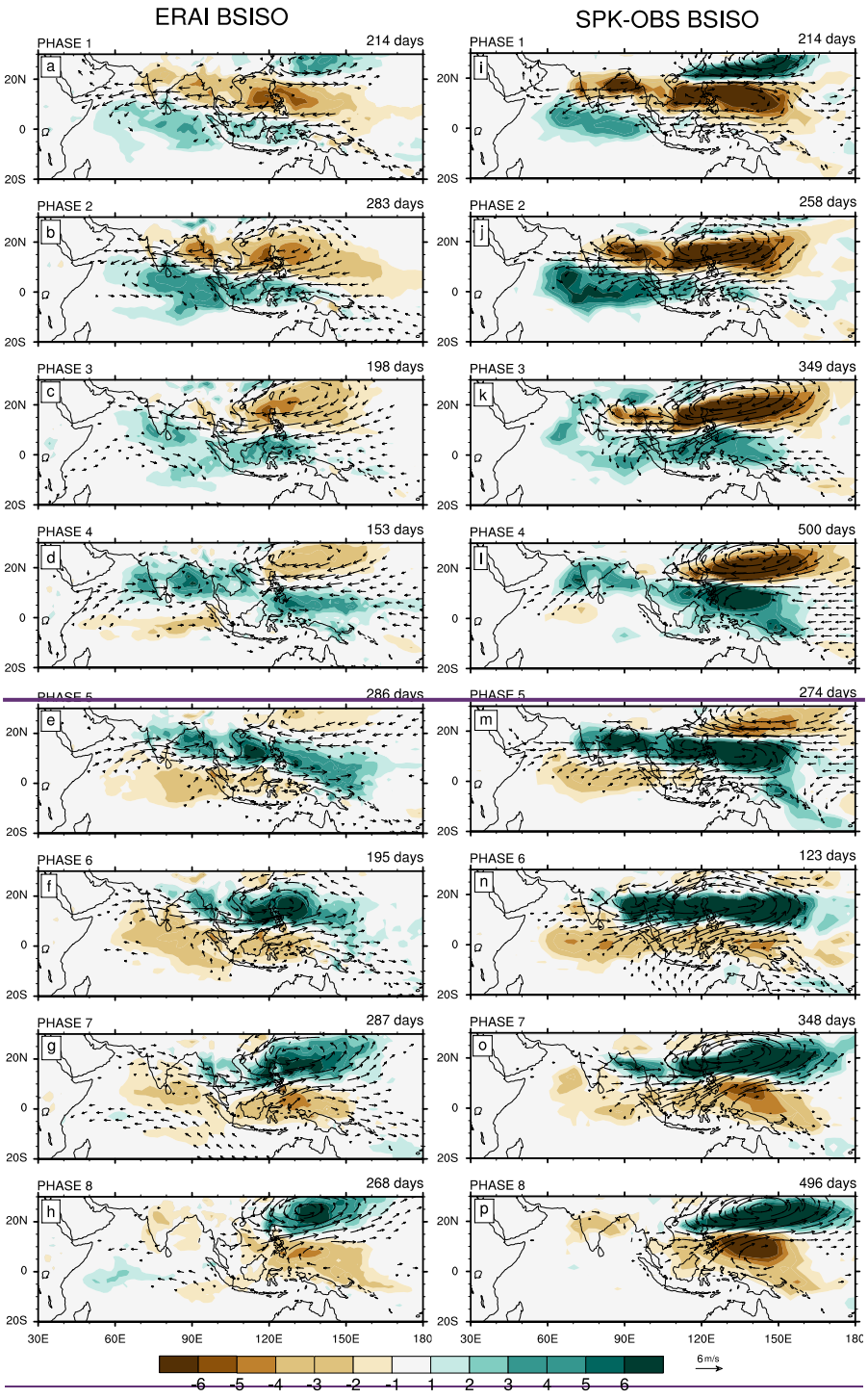
ERAI BSISO
SPK-OBS BSISO
PHASE 1
214 days
a
PHASE 1
214 days
i
PHASE 2
283 days
b
PHASE 2
258 days
j
PHASE 3
198 days
c
PHASE 3
349 days
k
PHASE 4
153 days
d
PHASE 4
500 days
l
PHASE 5
286 days
e
PHASE 5
274 days
m
PHASE 6
195 days
f
PHASE 6
123 days
n
PHASE 7
287 days
g
PHASE 7
348 days
o
PHASE 8
268 days
h
PHASE 8
496 days
p
20N
0
20S
30E
60E
90E
120E
150E
180
-6 -5 -4 -3 -2 -1 1 2 3 4 5 6
6 m/s

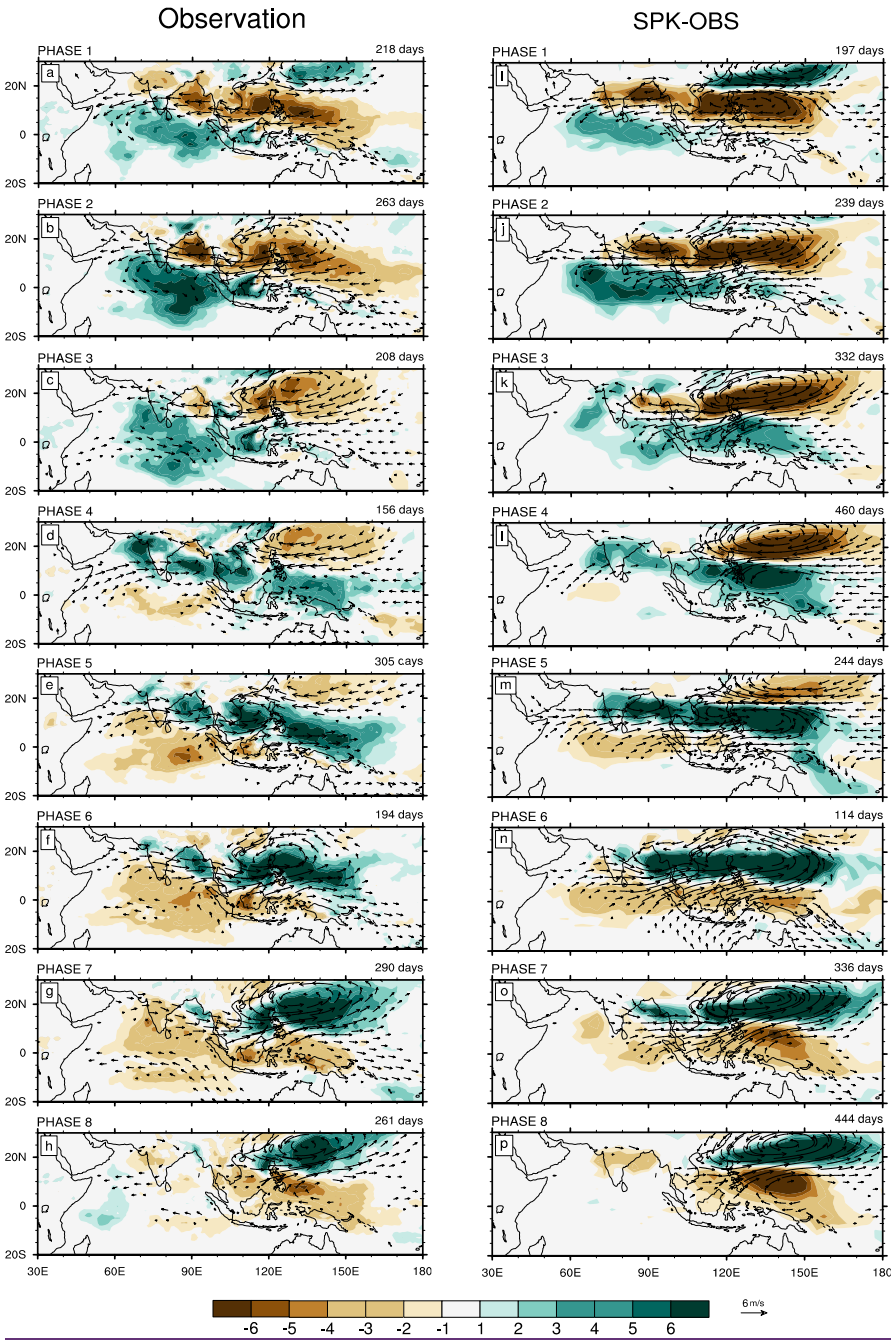

Figure 10: Composites of anomalous precipitation (shading; mm day^{-1}) and 850-hPa wind (vector; with amplitude > 1 m s^{-1}) in the BSISO life cycle from phase 1 to phase 8 for (a–h) GPCP precipitation and ERAI 850-hPa wind and (i–p) SPK-OBS. The number of days for phase composite is shown at the right corner above each panel. Only strong BSISO events (amplitude ≥ 1.5) are selected.

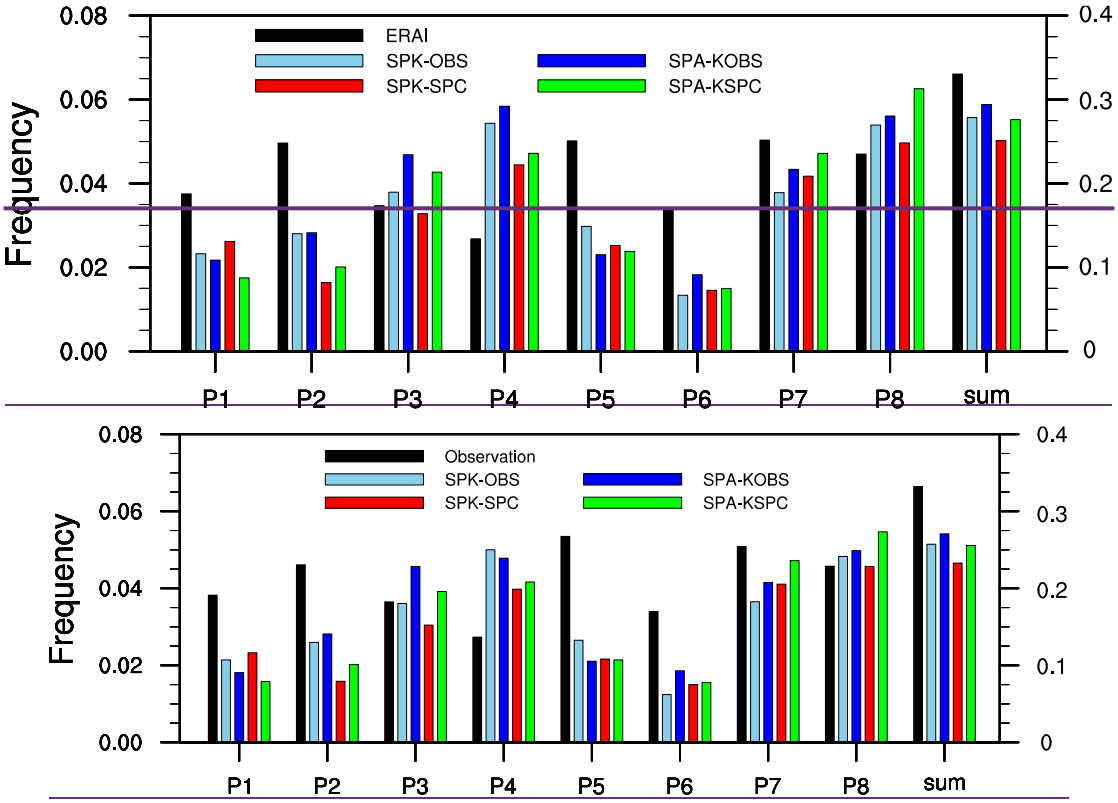

Figure 11: The frequency of strong BSISO activity (amplitude ≥ 1.5) in each phase (P1–P8; the left y-axis) and their sum (the right y-axis) for NOAA OLR and ERAI u850 (black), SPK-OBS (light blue), SPK-SPC (red), SPA-KOBS (dark blue), and SPA-KSPC (green).

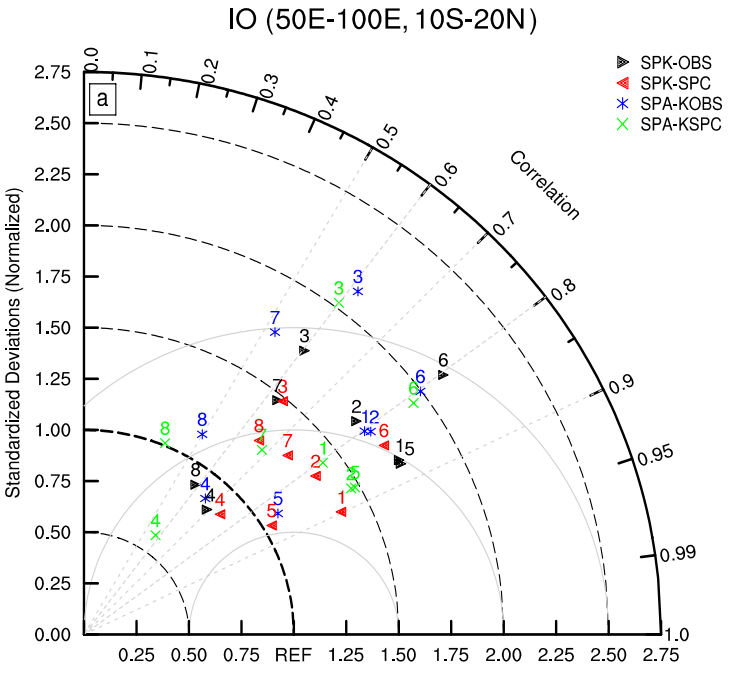
IO (50E-100E, 10S-20N)
a
SPK-OBS
SPK-SPC
SPA-KOBS
SPA-KSPC
Correlation
Standardized Deviations (Normalized)
REF

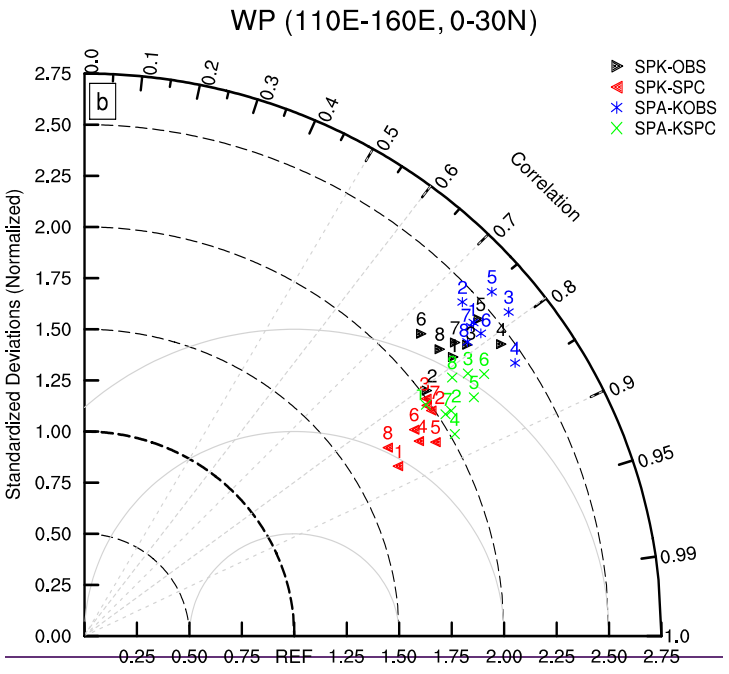
WP (110E-160E, 0-30N)
b
SPK-OBS
SPK-SPC
SPA-KOBS
SPA-KSPC
Correlation
Standardized Deviations (Normalized)
REF

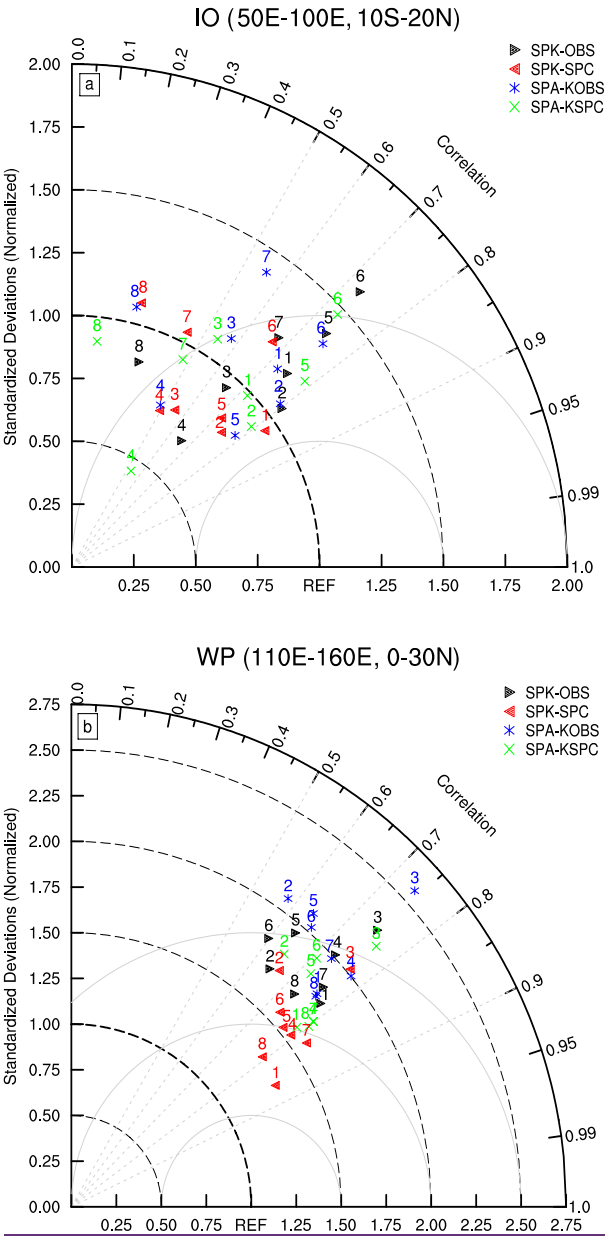

Figure 12: Taylor diagrams for anomalous precipitation in each BSISO phase averaged over (a) the Indian Ocean (IO; 50°–100°E, 10°S–20°N) and (b) western Pacific (WP; 110°–160°E, 0°–30°N). The number above each symbol refers to the BSISO phase.